POLITECNICO DI TORINO

College of Mechanical, Aerospace and Automotive Engineering

Master of Science in
MECHANICAL ENGINEERING

Master's Thesis

Design and Mechanical Performance Evaluation of Functionally Graded 316L Stainless Steel Lattice Structures Fabricated by Laser Powder Bed Fusion

Candidate:
Farbod Entezami

Supervisor:
Prof. Abdollah Saboori

Co-supervisor:
Dr. Amir Behjat

July 2026

Abstract

Laser Powder Bed Fusion (LPBF) enables the fabrication of metallic lattice structures with complex internal architectures that are difficult to produce using conventional manufacturing methods. This thesis investigates the compressive behavior of 316L stainless steel lattice structures based on Gyroid, Split-P, and stochastic Voronoi architectures. Cubic and cylindrical configurations were designed using nTop, manufactured by LPBF, separated from the build platform using Wire Electrical Discharge Machining, and evaluated through quasi-static compression testing. A selected group of specimens with the same relative volume was further analyzed using X-ray Computed Tomography and Abaqus finite element simulation. The results showed that the mechanical performance of the lattice structures was controlled not only by relative volume, but also by topology and internal configuration. Among the investigated samples, the Gyroid cylindrical structure GY-CYL-A showed the best overall performance, reaching the highest ultimate compressive strength and absorbed energy. The Split-P cylindrical structure SP-CYL-A presented the highest elastic modulus, making it the stiffest design. In contrast, the stochastic Voronoi structure showed lower and less stable performance due to its irregular load-transfer paths and localized deformation behavior. The Abaqus simulations reproduced the main experimental trends and helped interpret the stress distribution. However, differences between simulation and experiment were mainly related to the idealized numerical geometry and the presence of real LPBF manufacturing imperfections. Overall, this work confirms that TPMS-based cylindrical lattice structures provide promising mechanical efficiency for lightweight, load-bearing, and energy-absorbing applications.

Acknowledgements

I would like to express my sincere gratitude to my supervisor, Professor Abdollah Saboori, for his guidance, support, and valuable feedback throughout the development of this thesis. His knowledge and advice helped me shape the direction of this work and improve both the scientific quality and clarity of the research.

I would also like to thank my co-supervisor, Dr. Amir Behjat, for his helpful comments, technical support, and encouragement during the different stages of this project. His guidance was especially valuable in improving my understanding of the experimental and numerical aspects of the study.

I am also grateful to the researchers, technicians, and staff of the laboratory for their support during the fabrication, characterization, and testing activities. Their assistance made it possible to carry out the practical parts of this work in a reliable and organized way.

I would like to thank my family and friends, for their continuous encouragement, patience, and support. Their belief in me gave me the motivation to complete this thesis and overcome the challenges of this academic journey.

I would also like to express a special thanks to my friend Pouya Azarandaz for his continuous help, guidance, and support throughout this work. His advice, shared experience, and willingness to help during different stages of the thesis were highly valuable and sincerely appreciated.

Table of Contents

List of Figures

List of Tables

Chapter 1

Introduction

1.1 From Conventional Design to Architected Structures

The development of lightweight, mechanically efficient, and multifunctional structures is one of the central challenges in modern mechanical engineering. As it is shown in the figure 1, in several engineering sectors, including aerospace, automotive engineering, biomedical devices, energy systems, impact protection, and advanced manufacturing, components are required to provide reliable mechanical performance while minimizing mass, material consumption, and production complexity [1–6]. Weight reduction is particularly important because it can improve energy efficiency, reduce fuel consumption, decrease operating costs, and enhance the performance of moving or load-bearing systems [3,4,6]. At the same time, modern engineering components are increasingly expected to satisfy multiple functional requirements simultaneously, such as carrying mechanical loads, absorbing impact energy, enabling fluid flow, promoting heat transfer, or interacting with biological environments [5–7].

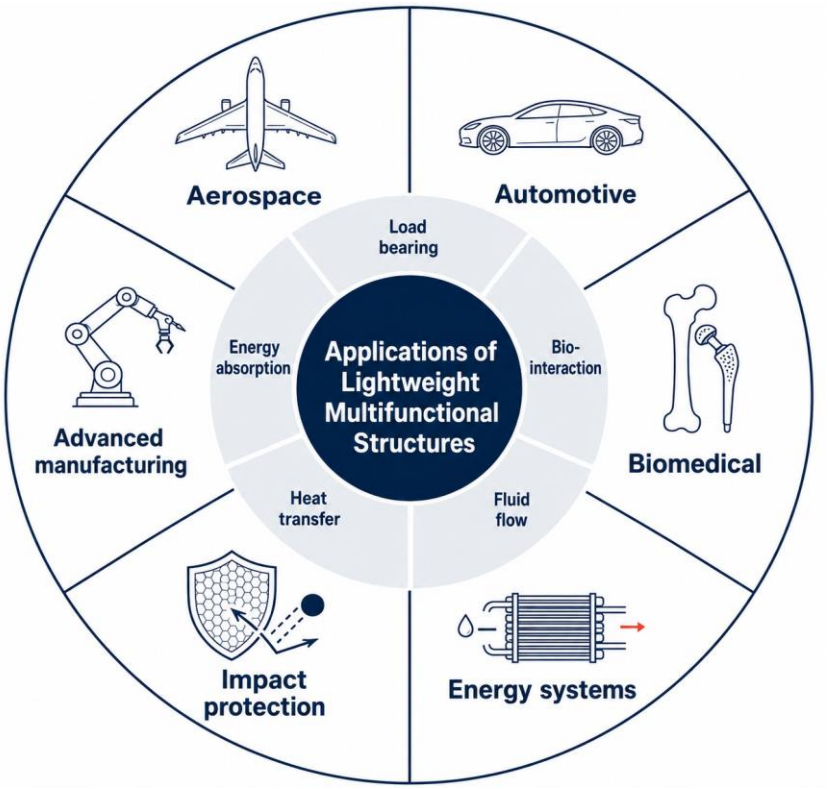

Figure 1. Application Areas and Functional Roles of Lightweight Multifunctional Structures [Created by the author].

Traditional engineering design has often relied on fully dense metallic components, where performance is mainly controlled by the intrinsic properties of the selected material and by the external geometry of the part. While this approach remains effective for many applications, it is not always the most efficient strategy when the objective is to maximize performance per unit mass [1,2]. In many structural components, material is not equally needed in every region. Some zones carry high loads, while others contribute less to the global mechanical response. This has motivated the development of optimized internal architectures, in which material can be distributed more efficiently inside a given design volume [1–4]. Instead of using a fully solid component, part of the internal volume can be replaced by controlled porosity or lattice networks to reduce weight while maintaining or tailoring stiffness, strength, and energy absorption [1–6].

This shift from fully dense components to internally architected structures represents an important change in the way mechanical performance is achieved. In this design approach, the internal geometry is no longer treated as an empty or inactive volume, but as a functional part of the component. By controlling the distribution of solid and void regions, the structure can be designed to guide load transfer, reduce unnecessary material, and introduce additional functional capabilities within the same external design envelope. Therefore, the performance of an engineering component becomes dependent not only on the material itself, but also on how that material is spatially arranged. This is particularly relevant for lightweight structures, where stiffness, strength, energy absorption, and functional requirements must be balanced

against mass reduction. However, the practical use of such architectures depends strongly on whether the required internal features can be manufactured with sufficient accuracy and repeatability.

Conventional manufacturing processes, such as casting, forging, forming, and machining, remain essential for producing a wide range of engineering components. However, these methods impose important restrictions on the geometrical complexity of a part [8–10]. Machining is limited by tool accessibility, especially when internal features, enclosed channels, porous networks, or free-form internal geometries are required [8,9]. Casting and forming often require molds, dies, draft angles, and simplified geometries to allow material flow, solidification, and part removal [8,9]. These limitations make it difficult to fabricate controlled porous structures, graded internal architectures, complex lattice networks, and topology-optimized components using conventional manufacturing methods [8–10]. As a result, many geometries that are mechanically attractive from a design perspective remain difficult or impossible to manufacture through traditional routes [8–10]. Figure 2 illustrates the transition from conventional dense design to optimized internal architecture.

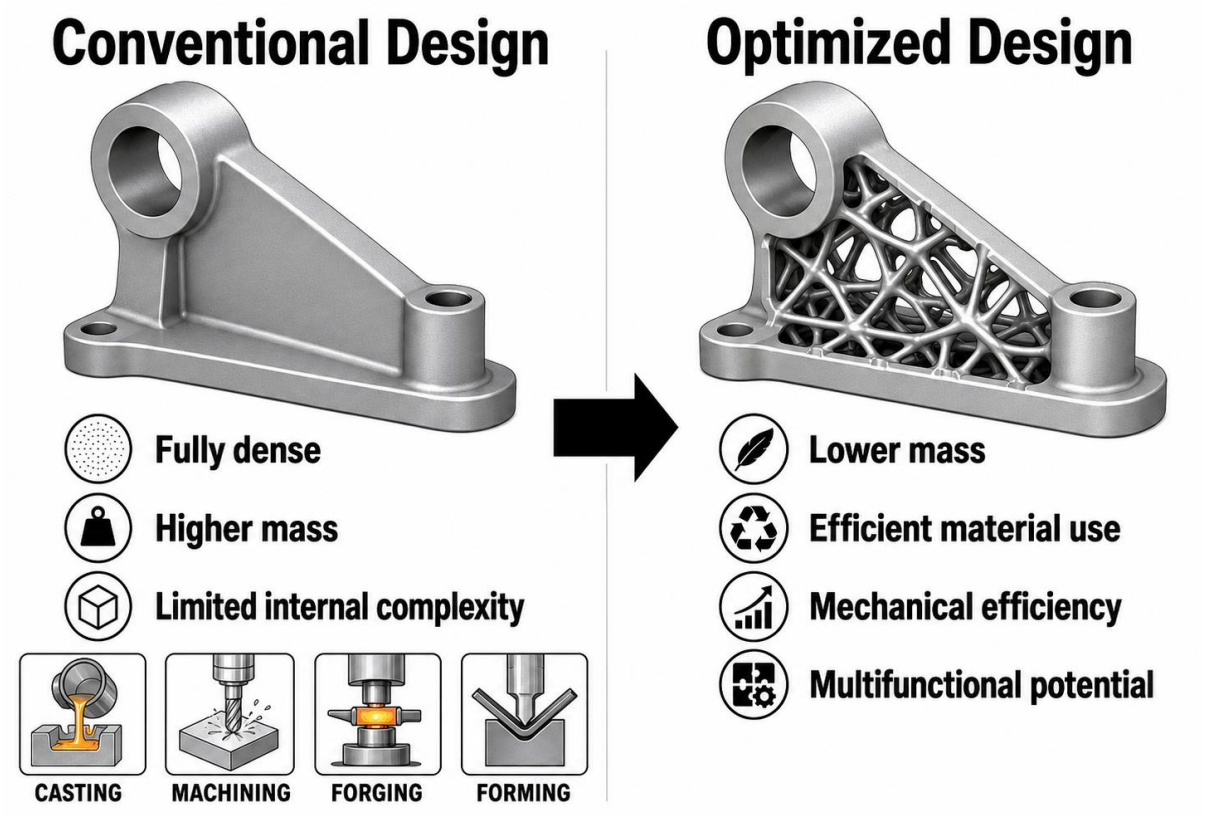

Figure 2. Transition from Fully Dense Design to Optimized Internal Architecture [Created by the author using AI-assisted graphic generation].

Additive Manufacturing (AM), commonly referred to as 3D printing, provides an alternative approach by producing components directly from digital model data through a

layer-by-layer process [8,9]. In contrast to subtractive manufacturing, where material is removed from a larger block, AM builds the final component by adding, melting, curing, or bonding material only where it is required [8,9]. This layer-wise manufacturing principle reduces many geometrical restrictions associated with conventional processes and enables the fabrication of complex external shapes and internal features [8–10]. As a result, AM has evolved from a rapid prototyping technique into a manufacturing route capable of producing functional engineering components [8–11].

The importance of AM is not limited to manufacturing itself; it also changes the design philosophy. In conventional production, the final geometry is often strongly influenced by manufacturing limitations such as tool access, mold removal, machining direction, and assembly constraints [8,10]. In AM, many of these restrictions are reduced, allowing the design process to be driven more directly by functional requirements such as stiffness, strength, energy absorption, permeability, thermal performance, and weight reduction [10–12]. This design flexibility has enabled the development of topology-optimized parts, cellular materials, lattice architectures, and functionally graded structures [10–16]. However, AM is not free from limitations. Surface roughness, residual stresses, build orientation, powder characteristics, support requirements, dimensional accuracy, and process-induced defects must still be considered during design, fabrication, and validation. Therefore, AM expands the design space, but reliable engineering application requires understanding the interaction between geometry, material, process parameters, manufacturing quality, and mechanical response [7,11,12,17].

This expanded design space is especially important for architected materials. Architected materials are structures whose macroscopic properties are governed not only by the intrinsic properties of the base material but also by their internal geometry. By controlling the arrangement of material within a given volume, it is possible to tune stiffness, strength, density, permeability, deformation mode, and energy absorption [1–4]. This concept allows engineers to create structures that behave differently from the parent material alone. For example, a fully dense material may be stiff and strong, while the same material arranged into a lattice architecture may become lightweight, deformable, and energy absorbing.

Lattice and porous structures represent one of the most important categories of architected materials. Their mechanical response can be controlled through topology, relative density, unit cell size, wall thickness, strut diameter, connectivity, and spatial material distribution. These structures are attractive because they can provide high specific stiffness and strength, controlled deformation, permeability, and efficient energy absorption [1–6]. In biomedical applications, porous structures may reduce stiffness mismatch between implant and bone, while interconnected pores can support bone ingrowth and biological fixation [5,18,19]. In thermal and fluid-related applications, large internal surface area and connected channels can improve heat transfer, fluid transport, or filtration [7,20,21]. In impact and energy absorption applications, controlled collapse under compression can allow the structure to dissipate mechanical energy over a large deformation range [6,21,22].

Porosity must be considered carefully in additively manufactured structures. Porosity may be intentional or unintentional. Intentional porosity is introduced by design and is used to control mass, stiffness, permeability, or energy absorption [1,5,7]. Unintentional porosity, in contrast, is a manufacturing defect caused by incomplete melting, gas entrapment, keyhole instability, or other process-related mechanisms. In additively manufactured lattice structures, these two forms of porosity may coexist. The lattice architecture contains designed pores, while the manufacturing process may introduce additional defects such as lack-of-fusion pores, gas pores, keyhole pores, unmelted powder, and rough surfaces [17,23,24]. Therefore, the mechanical behavior of additively manufactured lattices cannot be understood only from the nominal CAD model. It must also be interpreted considering as-built geometry, internal defects, surface condition, material behavior, and testing conditions [23–26]. In figure 3, a graphical summary is presented.

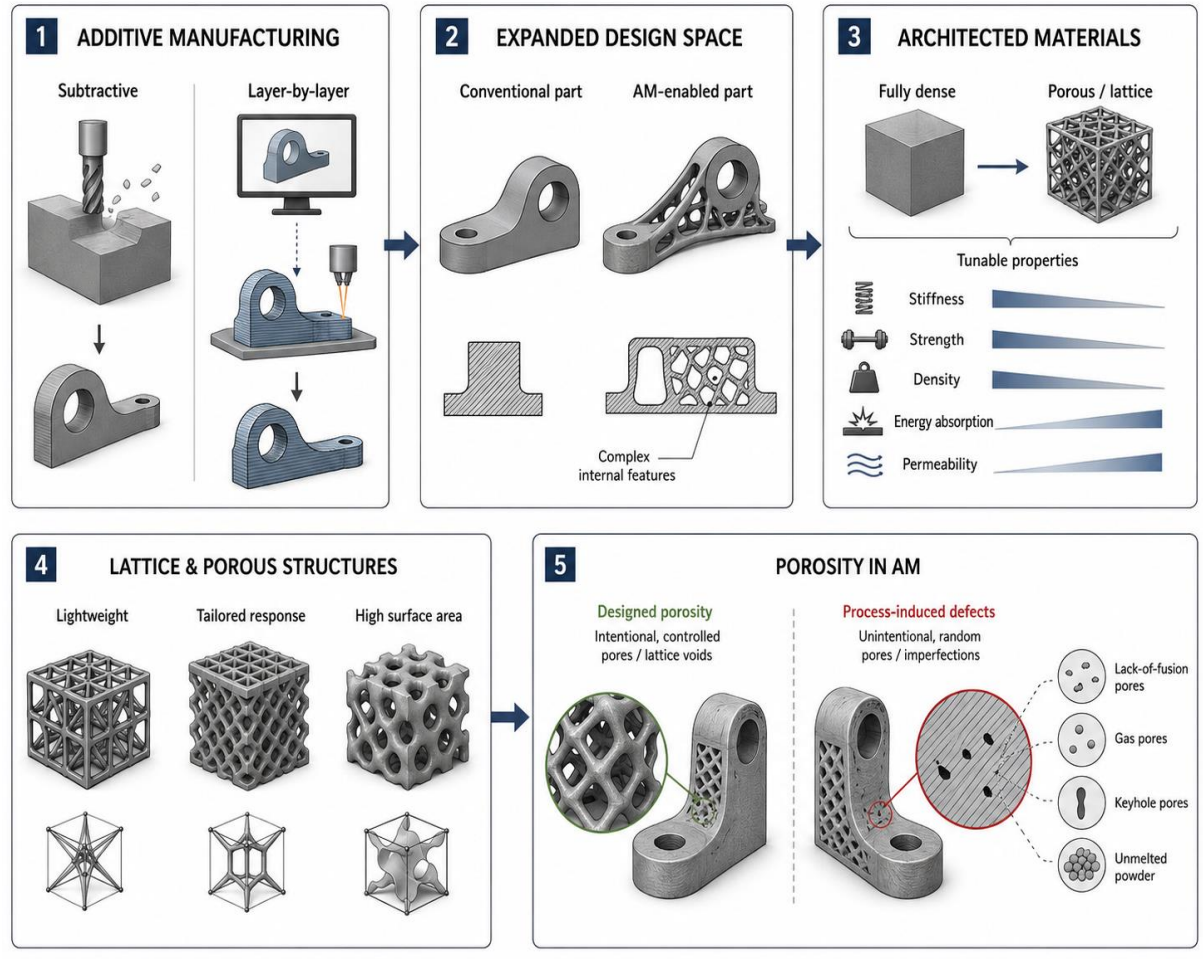

Figure 3. AM as an Enabler of Architected and Porous Structures [Created by the author using AI-assisted graphic generation].
(Schematic representation of the transition from subtractive to layer-by-layer manufacturing, the resulting expansion of design freedom, the development of architected lattice and porous structures, and the distinction between designed porosity and process-induced defects in additively manufactured components.)

1.2 Additive Manufacturing and Laser Powder Bed Fusion

As shown in Figure 4, AM is not a single manufacturing process but a family of technologies, that differ in feedstock form, bonding mechanism, energy source, material compatibility, resolution, productivity, and final part performance. According to the ISO/ASTM classification, AM processes are commonly grouped into seven main categories: material extrusion, vat photopolymerization, binder jetting, material jetting, sheet lamination, directed energy deposition, and powder bed fusion. A comparison of these process categories is presented in Figure 5. Material extrusion deposits heated filament, pellets, or paste through a nozzle, while vat photopolymerization selectively cures liquid photopolymer resins using light-based energy. Binder jetting joins powder particles by selectively depositing a liquid binder, whereas material jetting deposits droplets of build material in a controlled manner. Sheet lamination forms parts by bonding and cutting stacked sheets, and directed energy deposition uses focused thermal energy to melt powder or wire feedstock as it is deposited. Powder bed fusion, in contrast, selectively fuses regions of a powder layer using a laser or electron beam. This classification is important because each AM family offers different advantages and limitations in terms of achievable geometry, material selection, surface quality, mechanical properties, cost, and scalability [8,27,28].

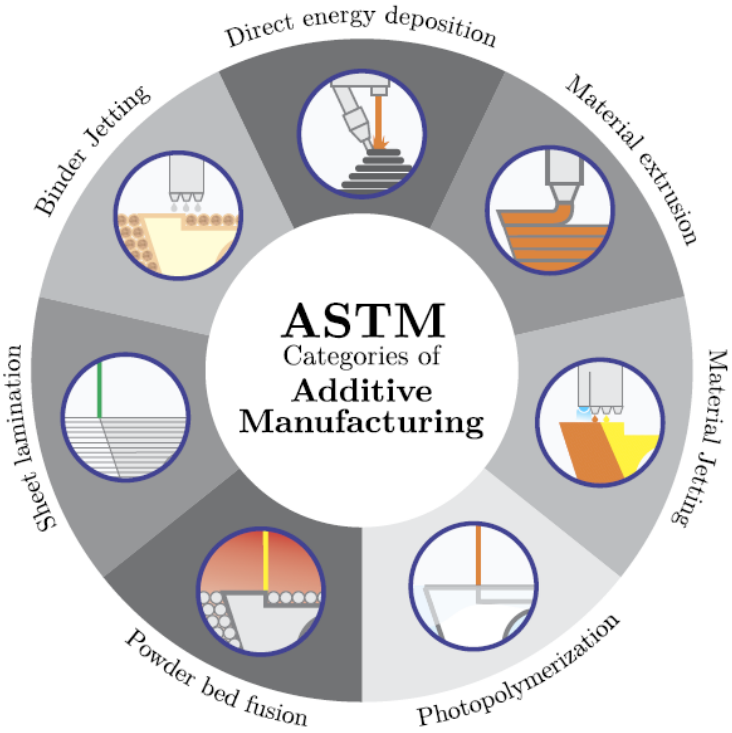

Figure 4. ASTM categories of AM [28].

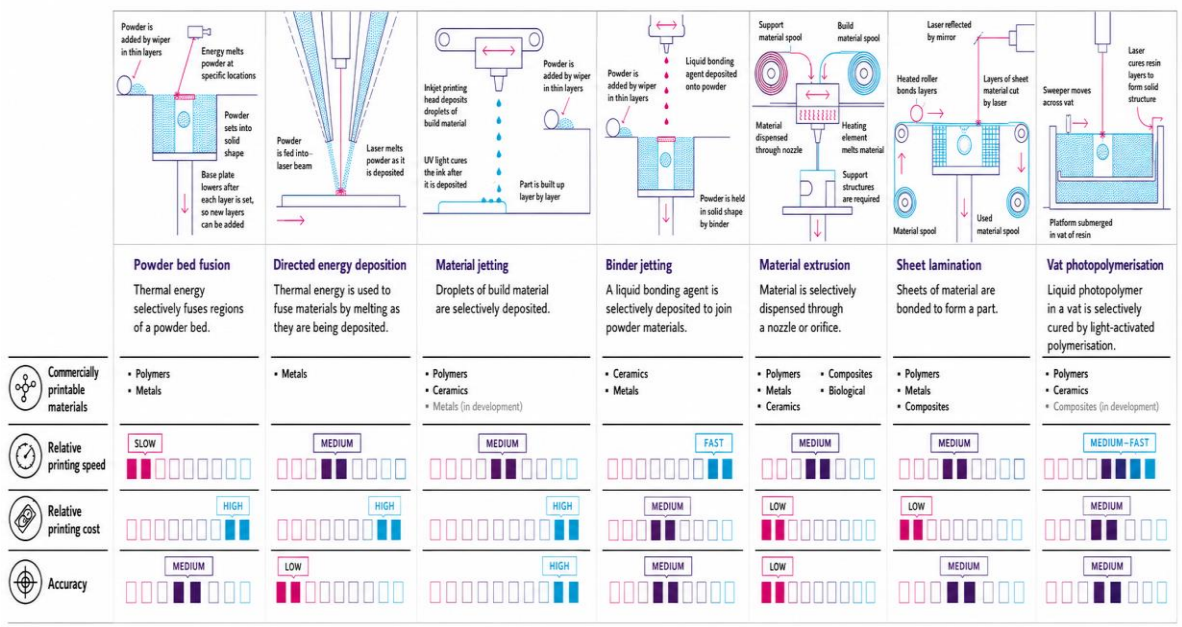

Figure 5. Overview and Comparison of AM Processes Based on Operating Principles, Compatible Materials, Printing Speed, Cost, and Accuracy [29].

Among these technologies, Powder Bed Fusion (PBF) is particularly important for metallic materials because it enables the production of complex metallic components directly from powder feedstock. In PBF, a thin layer of powder is spread over a build platform, and selected regions of the powder bed are fused according to the sliced geometry of the digital model. After each layer is processed, the build platform is lowered and a new powder layer is deposited, allowing the component to be built progressively in the vertical direction.

Metallic PBF processes mainly include Laser Powder Bed Fusion (LPBF) and Electron Beam Powder Bed Fusion [11,12,27]. In this thesis, the term LPBF is used to describe the laser-based powder bed fusion process for metals. In the literature, the same process is also frequently referred to as Selective Laser Melting (SLM), particularly when the metallic powder is fully melted during processing. In LPBF/SLM, a focused laser beam selectively melts metallic powder particles according to the cross-section of the part [11,12]. As the laser scans over the powder bed, a localized melt pool forms, solidifies rapidly, and bonds with the previously solidified material [11,23]. Repeating this process layer by layer produces the final metallic component. LPBF is widely used because it provides high geometrical resolution, good process control, and compatibility with many engineering alloys [11,12].

LPBF is especially suitable for producing lattice structures because it can fabricate complex internal geometries directly from digital models. Internal pores, curved surfaces, thin walls, spatially varying architectures, and interconnected channels can be produced without the need for molds or direct tool access [3,12]. This makes LPBF a key manufacturing technology for metallic lattices, biomedical implants, energy absorbers, lightweight structures, heat exchangers, and multifunctional components [3,5–7,18–22].

However, the successful fabrication of these structures depends strongly on process parameters, material behavior, feature size, build orientation, powder removal, and post-processing [3,11,12,17].

The LPBF process is schematically shown in Figure 6. During LPBF, complex thermal and physical phenomena occur, including powder-particle dynamics, melt-pool flow, solidification, vaporization, and residual-stress development, as summarized in Figure 7. During laser exposure, powder particles absorb energy, melt, form a melt pool, and solidify rapidly as the laser moves forward. Melt-pool behavior is influenced by heat conduction, surface tension, recoil pressure, vaporization, and fluid flow [11,23]. Repeated layer deposition produces complex thermal histories, residual stresses, melt-pool boundaries, and possible anisotropy [11,23,30]. These phenomena influence the final microstructure, porosity, residual stress state, surface roughness, density, and mechanical performance of the printed material [11,17,23].

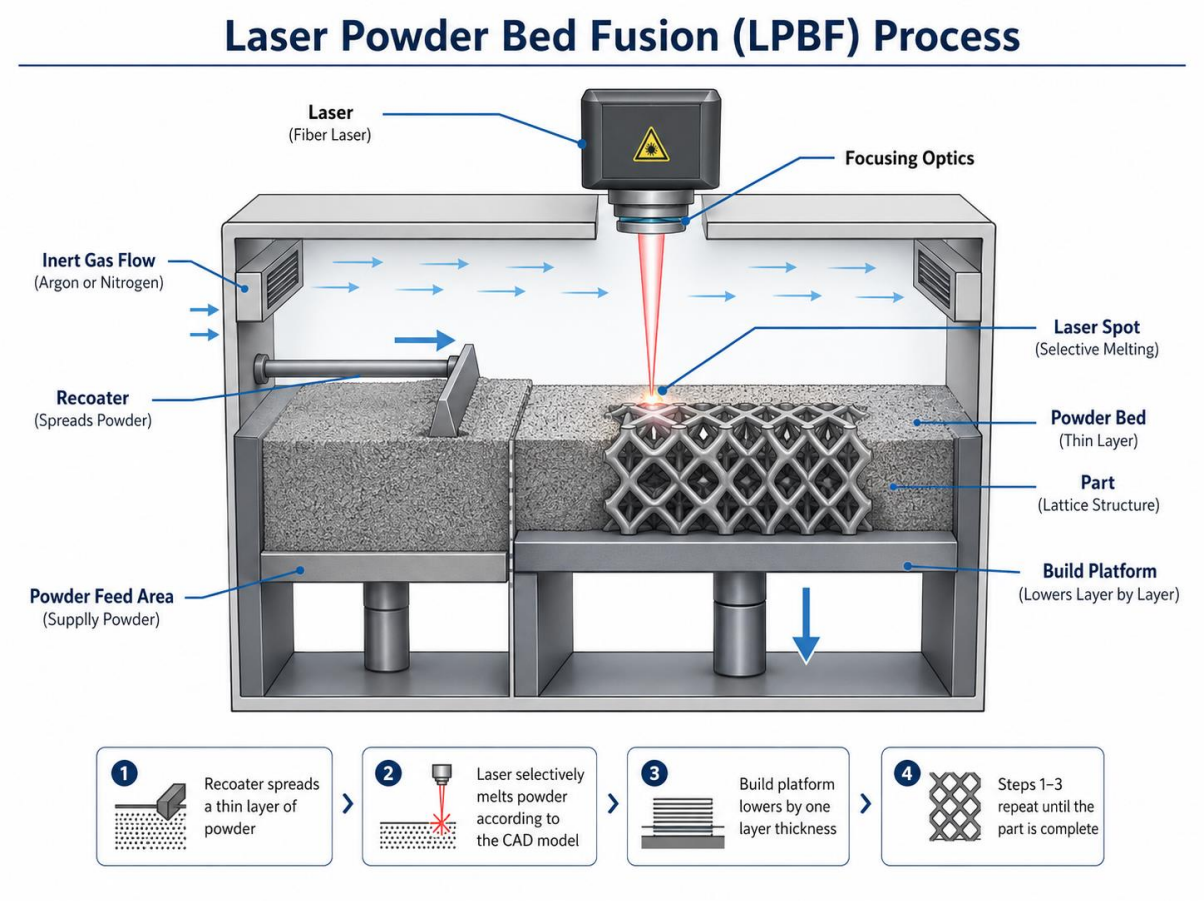

Figure 6. LPBF Process [Created by the author using AI-assisted graphic generation].

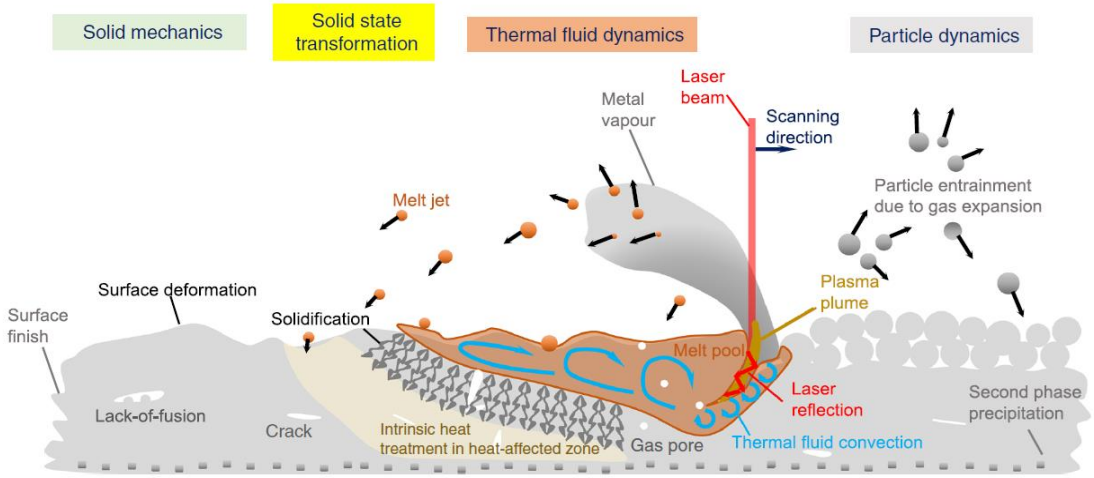

Figure 7. Schematic Illustration of Multiscale and Multiphysics Phenomena in Powder Bed Fusion AM [31].
(Different physical phenomena taking place during AM include powder-particle dynamics due to gas expansion, thermal fluid dynamics involving solid–liquid–vapor transitions during laser interaction, solid-state transformations such as precipitation during remelting and intrinsic heat treatment, and subsequent solid mechanics related to damage mechanisms such as cracking.)

The main LPBF process parameters, include laser power, scan speed, hatch spacing, layer thickness, scan strategy, powder morphology, particle size distribution, and build atmosphere [11,12,17]. Laser power controls the energy supplied by the beam, while scan speed determines the interaction time between the laser and the powder bed [17,24,32]. Hatch spacing determines the overlap between adjacent melt tracks, and layer thickness controls the powder volume that must be melted in each layer [17,24–26]. Scan strategy influences heat accumulation, residual stress formation, crystallographic texture, and anisotropy [11,17,33]. Powder morphology and particle size distribution influence powder spreading, packing density, and melt-pool stability [12,17].

A commonly used engineering parameter for comparing LPBF processing conditions is the volumetric energy density *VED* ($\frac{J}{mm^3}$), which is expressed as the following equation:

$$\mathrm{VED} = \frac{P}{v \cdot h \cdot t} \tag{1}$$

where P is the laser power ($\frac{J}{s}$), v is the scan speed ($\frac{mm}{s}$), h is the hatch spacing (mm), and t is the layer thickness (mm). This parameter provides a simplified estimate of the energy input delivered to a unit volume of powder during processing. The main LPBF processing parameters are schematically shown in Figure 8.

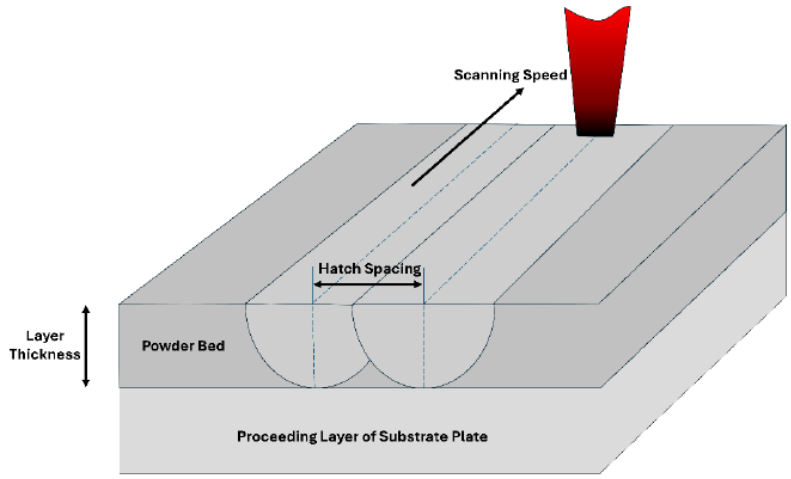

Figure 8. Schematic of LPBF Processing Parameters **[34].**

Although VED is useful for identifying general trends in density and defect formation, it does not fully describe the process. Different combinations of laser power, scan speed, hatch spacing, and layer thickness can produce the same nominal energy density while generating different melt-pool geometries, thermal histories, surface conditions, and defect types. Therefore, volumetric energy density should be considered an engineering indicator rather than a complete physical descriptor of LPBF [11,17,35]. The main process-parameter groups in LPBF are summarized in Figure 9.

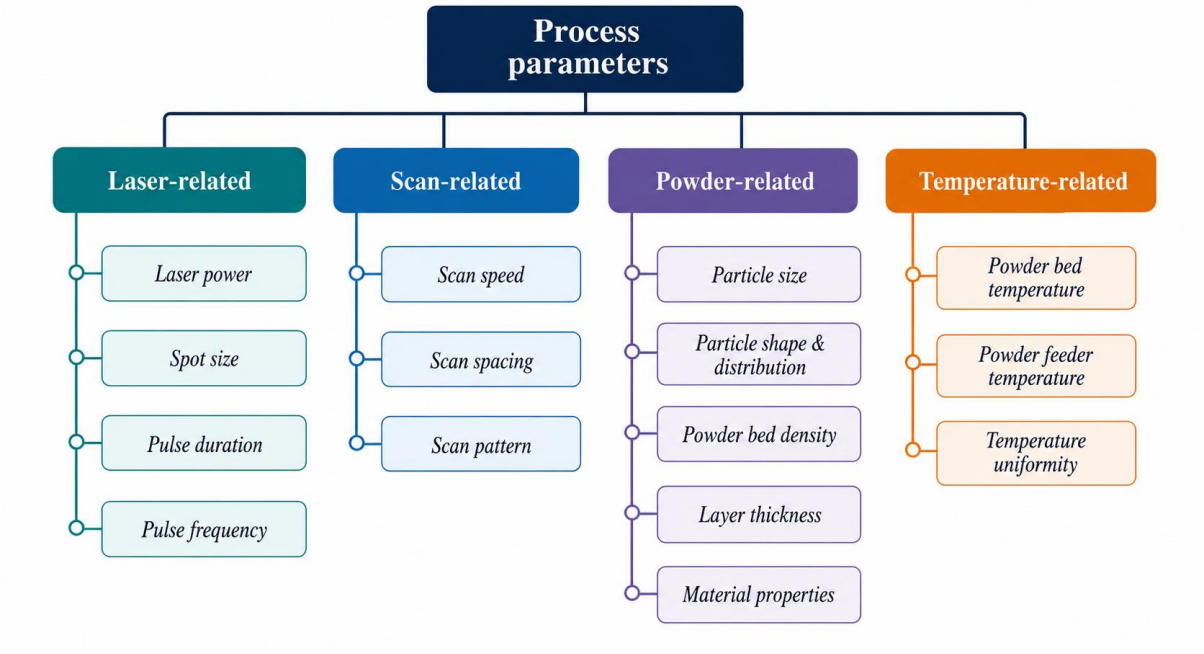

Figure 9. Main Process Parameters in the SLM/LPBF Process [Created by the author].

Defects in LPBF are often associated with an unsuitable process window. If the energy input is insufficient, the powder may not fully melt, leading to lack-of-fusion defects and poor bonding between adjacent scan tracks or layers. Such defects are often irregular and can significantly reduce mechanical reliability [17,23,24]. If the energy input is excessive, the melt pool may become unstable, producing vaporization, spatter, keyhole porosity, and surface degradation. Therefore, reliable LPBF manufacturing requires balancing sufficient melting against excessive energy input [17,24–26,32,35].

The issue of defect formation is particularly important for lattice structures. In dense components, a small pore may represent only a limited fraction of the load-bearing cross-section. In a lattice wall or strut, however, the same defect may occupy a significant portion of the local load-bearing area [3,23,36]. Surface roughness and partially melted powder particles can also be more influential in lattices because of their high surface-area-to-volume ratio. As a result, LPBF-fabricated lattice structures can be more sensitive to process-induced imperfections than dense bulk specimens [3,20,23,25,26].

For this reason, the study of LPBF lattice structures requires more than nominal design evaluation. It also requires characterization of as-built geometry, internal porosity, surface quality, and mechanical performance [3,25,26,37,38]. In the present thesis, this is addressed by combining LPBF fabrication with X-ray Computed Tomography (XCT) inspection, compression testing, and Abaqus-based numerical simulation.

1.3 Stainless Steel 316L as the Material System

Stainless steel 316L is one of the most widely studied alloys in LPBF due to its corrosion resistance, weldability, ductility, and broad industrial relevance. It is used in mechanical, chemical, marine, biomedical, aerospace, automotive, and energy-related applications where corrosion resistance and structural reliability are important. In AM, 316L is attractive because it can be processed into complex geometries while retaining useful mechanical properties [17,18,23,30,33].

The microstructure of LPBF-fabricated 316L differs from conventionally processed 316L because of the rapid melting and solidification cycles involved in the process. High cooling rates in LPBF can produce refined cellular and columnar microstructural features. Compared with laser cladding deposition, SLM produces smaller melt pools and higher cooling rates, resulting in finer microstructural features [19]. This microstructural refinement can contribute to the higher yield strength often reported for LPBF 316L compared with conventionally manufactured 316L [23,33].

However, the mechanical behavior of LPBF 316L is not controlled only by grain refinement. It is also affected by scan strategy, build orientation, residual stresses, melt-pool boundaries, crystallographic texture, porosity, and surface condition [17,18,23–26,30,32,33,35,36,39]. LPBF 316L may exhibit anisotropic mechanical behavior because the thermal history and layer-wise build direction can influence microstructure and defect orientation. Therefore, LPBF 316L should not automatically be treated as equivalent to

conventionally manufactured 316L, especially when interpreting experiments or defining material properties for finite element simulations [23,30,33].

The process window is also important for LPBF 316L. Stable melting occurs only within an appropriate energy-input range. Insufficient energy input can lead to lack-of-fusion defects and low density, while excessive energy input can promote vaporization and keyhole porosity. Density, microstructure, tensile strength, productivity, and surface quality of LPBF 316L can therefore be influenced by the selected process parameters [17,24–26,32,35]. This process sensitivity is particularly important when the material is used for lattice structures, where local defects can strongly influence global mechanical response [3,23,36].

Process-induced defects in LPBF 316L may include internal pores, lack-of-fusion regions, partially melted powder particles, surface roughness, and near-surface defects. These imperfections can act as stress concentration sites and reduce mechanical reliability [17,18]. Although many studies discuss these defects in relation to fatigue, they are also relevant for quasi-static compression of lattice structures because they may affect collapse initiation, local stiffness, and deformation stability [18,30,33]. In thin-walled lattice regions, even small defects may significantly modify the local load-bearing behavior [3,18,33].

The use of stainless steel 316L is particularly relevant for the present thesis because the selected lattice architectures are investigated as real metallic structures fabricated by LPBF. Compared with other commonly used AM metals, 316L combines ductility, corrosion resistance, and processability, making it suitable for evaluating compression behavior, energy absorption, and numerical validation of lattice structures. At the same time, its LPBF-specific microstructure and defect sensitivity require careful interpretation of experimental and numerical results [17,18,23,30,33].

The use of stainless steel 316L also affects numerical modeling. For global compression simulations, simplified elastic–plastic material models are often used to reduce complexity [40,41]. However, LPBF 316L can show anisotropy, strain hardening, and fracture behavior that depend on build orientation, stress state, and loading condition. Therefore, any simplified material model used in Abaqus must be interpreted as an approximation rather than a complete representation of the real LPBF material response [30,41]. This is especially important when comparing idealized finite element models with experimental compression tests.

The material data used in the Abaqus simulations are therefore taken from LPBF-fabricated stainless steel 316L with the same powder composition as the printed specimens, rather than from generic wrought 316L datasheets.

1.4 Lattice Structures and Architected Materials

Lattice structures are architected materials in which the global mechanical response depends on the internal arrangement of material. In a fully dense material, stiffness and strength are mainly controlled by material composition, microstructure, and processing history. In a lattice structure, however, the internal geometry plays a central role. By

modifying topology, relative density, cell size, wall thickness, strut diameter, connectivity, and grading strategy, it is possible to tailor the mechanical and functional behavior of the structure [1–6].

Relative density is a fundamental parameter in cellular and lattice materials. It is generally defined as the density of the porous structure divided by the density of the fully dense parent material. Increasing relative density generally increases stiffness and strength, but also increases mass. Therefore, lattice design requires balancing mechanical performance and weight reduction [1–4]. In lightweight applications, the most efficient structure is not necessarily the one with the highest absolute strength, but the one that provides the best performance relative to its mass [1–6].

The deformation mechanism of a lattice depends strongly on topology. Some lattice structures are stretching-dominated, meaning that their members carry mainly axial loads. These structures tend to show higher stiffness and strength [1,2]. Other structures are bending-dominated, meaning that deformation occurs mainly through bending of members. These structures may show lower stiffness but can provide stable collapse and energy absorption. This distinction helps explain why different lattice topologies with similar relative density can behave differently under compression [1,2,6].

Additively manufactured lattices may be designed as strut-based, sheet-based, or hybrid architectures. Representative strut-based unit-cell topologies are shown in Figure 10 [3,42]. Strut-based lattices consist of beams or trusses connected at nodes. They are relatively simple to design but may contain stress concentrations at joints [3,42]. Sheet-based lattices, including many Triply Periodic Minimal Surface (TPMS) structures. Representative TPMS unit-cell geometries are shown in Figure 11. These structures consist of continuous surfaces and may provide smoother stress distribution [7,22,37,40]. Stochastic lattices, such as Voronoi structures, introduce irregularity and can imitate natural porous architectures [43–45]. A representative stochastic Voronoi lattice is shown in Figure 12. Each family has different advantages and limitations depending on the intended application [3,7,42–45].

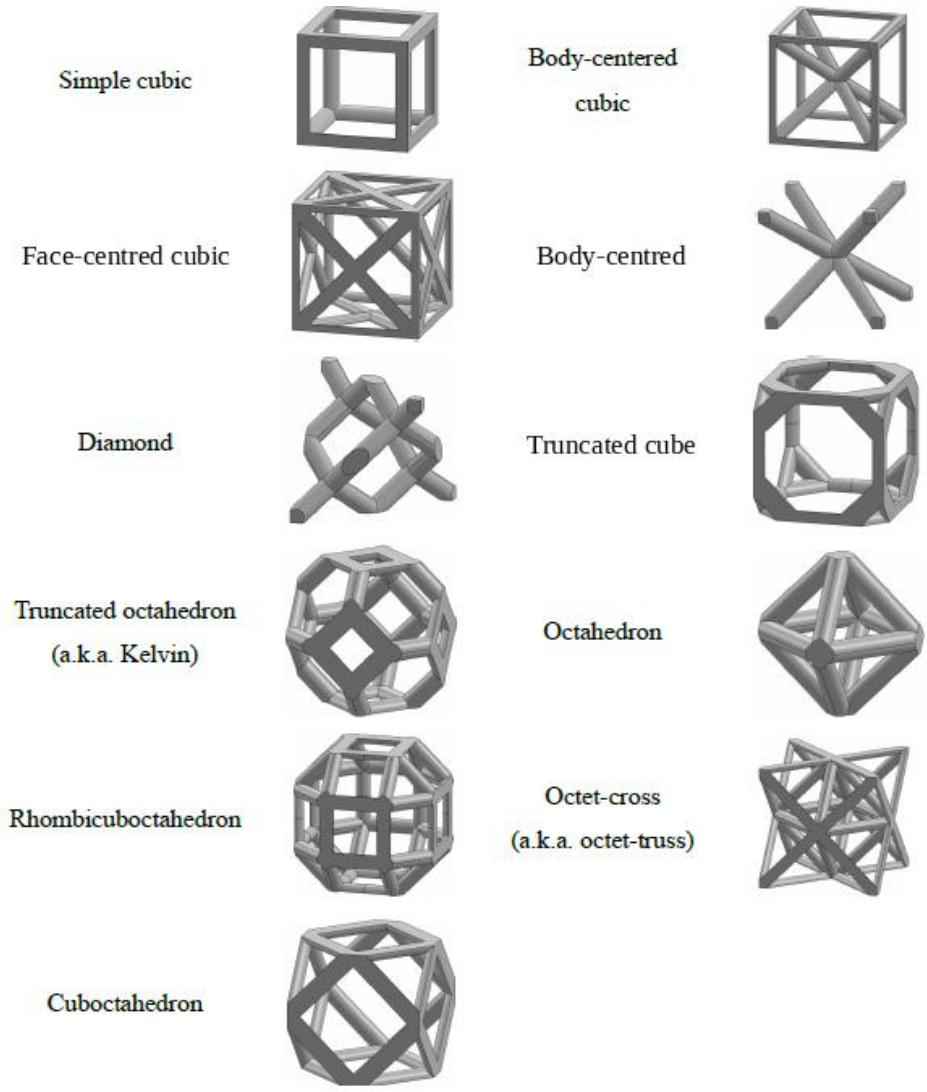

***Figure 10. Representative Strut-Based Lattice Unit-Cell Topologies* [46].**

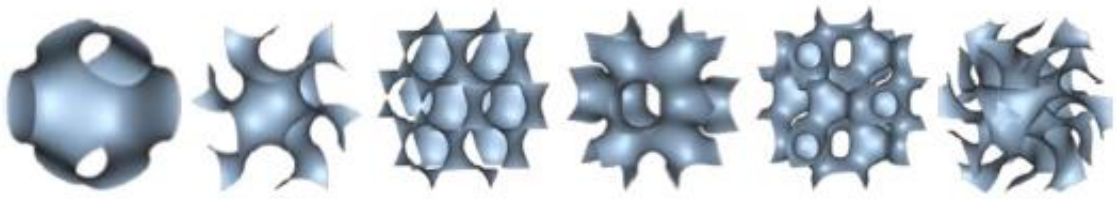

Figure 11. Representative TPMS Unit-Cell Geometries [7].

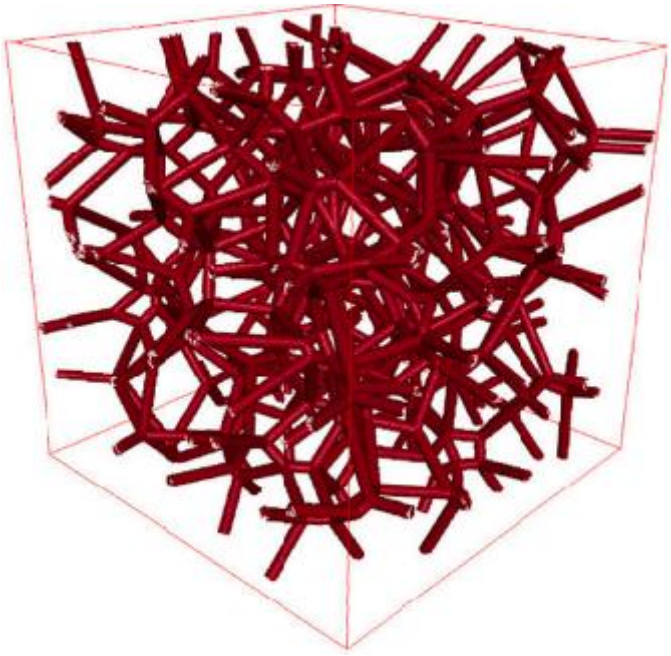

Figure 12. Representative Stochastic Voronoi Lattice Structure **[44].**

LPBF has significantly increased the practical relevance of metallic lattice structures. Complex geometries that were previously difficult to manufacture can now be produced directly from digital models [3,12]. However, successful fabrication of lattices remains challenging [3,37]. Thin walls and struts may be affected by roughness, overmelting, under-melting, powder adhesion, and dimensional deviations [3,17,37]. These manufacturing features influence effective geometry and mechanical response. Therefore, the final performance of LPBF lattices depends on both designed architecture and manufacturing quality [3,23,37,38].

The present thesis treats lattice structures as real manufactured components rather than ideal mathematical objects. This distinction is important because the selected geometries are not only simulated, but also fabricated, inspected, and mechanically tested. XCT and compression testing allow the actual behavior of the printed structures to be compared with numerical predictions, providing insight into the combined influence of topology, material, manufacturing quality, and modeling assumptions.

1.5 Triply Periodic Minimal Surface (TPMS) Structures

TPMS structures are a class of porous architectures defined by continuous surfaces that repeat periodically in three independent spatial directions. The mathematical mid-surface of a TPMS has zero mean curvature, meaning that the local surface curvatures are balanced. This gives TPMS structures smooth and continuous geometries, distinguishing them from conventional strut-based lattices that often contain sharp nodes and beam intersections. The absence of sharp junctions can reduce severe local stress concentrations and improve stress distribution [7,22,37].

TPMS structures are usually generated using implicit mathematical equations, as shown in Figure 13. This allows the designer to control unit cell size, wall thickness, level-set value, relative volume, pore size, surface area, and permeability. This mathematical controllability is one of the main advantages of TPMS structures because it allows systematic design variation and comparison between different topologies [7,37]. TPMS geometries can also be used to create uniform or graded porous structures by varying wall thickness, unit cell size, amplitude, or level-set parameters [7,13–16,38].

Common TPMS topologies include Gyroid, Primitive, Diamond, I-Wrapped Package, Neovius, Fischer–Koch, and F-Rhombic Dodecahedron structures [7,37]. Although they belong to the same general family, these geometries can show very different mechanical responses because material distribution and load paths differ between topologies [37,47,48]. Therefore, it is not sufficient to refer to TPMS structures as a single category when discussing mechanical performance. The specific topology must be considered [37,47].

Figure 14 summarizes AM technologies and multifunctional applications associated with TPMS structures. Their smooth surfaces reduce abrupt geometrical discontinuities [7,22,37]. Their interconnected pore networks can support fluid flow, biological integration, and transport phenomena [7,49]. Their high surface-area-to-volume ratio can be useful for heat transfer and filtration. In mechanical applications, their continuous surfaces can promote progressive deformation and energy absorption under compression. These features make TPMS structures relevant for biomedical scaffolds, lightweight components, energy absorbers, heat exchangers, and multifunctional structures [7,20–22,37,47,49].

Sheet-based TPMS structures are particularly important because they are composed of continuous shells rather than isolated beams or struts. This can lead to smoother stress transfer and potentially higher stiffness, plateau stress, and energy absorption compared with some conventional lattice architectures. However, their performance depends strongly on topology, relative density, shell thickness, material, build orientation, and manufacturing quality. Therefore, experimental characterization and numerical modeling are both needed to understand their behavior under compression [22,37,40,50].

Unit name	Mathematical expressions	3D models
P	$f(x,y,z) = \cos(\omega_x x) + \cos(\omega_y y) + \cos(\omega_z z) = C$	
G	$f(x,y,z) = \sin(\omega_x x)\cos(\omega_y y) + \sin(\omega_z z)\cos(\omega_x x) + \sin(\omega_y y)\cos(\omega_z z) = C$	
D	$f(x,y,z) = \cos(\omega_x x)\cos(\omega_y y)\cos(\omega_z z) - \sin(\omega_x x)\sin(\omega_y y)\sin(\omega_z z) = C$	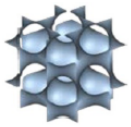
I-WP	$f(x,y,z) = 2[\cos(\omega_x x)\cos(\omega_y y) + \cos(\omega_y y)\cos(\omega_z z) + \cos(\omega_z z)\cos(\omega_x x)] - [\cos(2\omega_x x) + \cos(2\omega_y y) + \cos(2\omega_z z)] = C$	
F-RD	$f(x,y,z) = 4\cos(\omega_x x)\cos(\omega_y y)\cos(\omega_z z) - [\cos(2\omega_x x)\cos(2\omega_y y) + \cos(2\omega_x x)\cos(2\omega_z z) + \cos(2\omega_y y)\cos(2\omega_z z)] = C$	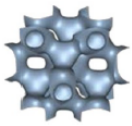
I_2-Y**	$f(x,y,z) = -2[\sin(2\omega_x x)\cos(\omega_y y)\sin(\omega_z z) + \sin(\omega_x x)\sin(2\omega_y y)\cos(\omega_z z) + \cos(\omega_x x)\sin(\omega_y y)\sin(2\omega_z z)] + \cos(2\omega_x x)\cos(2\omega_y y) + \cos(2\omega_y y)\cos(2\omega_z z) + \cos(2\omega_x x)\cos(2\omega_z z) = C$	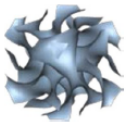

Figure 13. Mathematical Definitions and Representative 3D Models of Common TPMS Unit Cells [7].

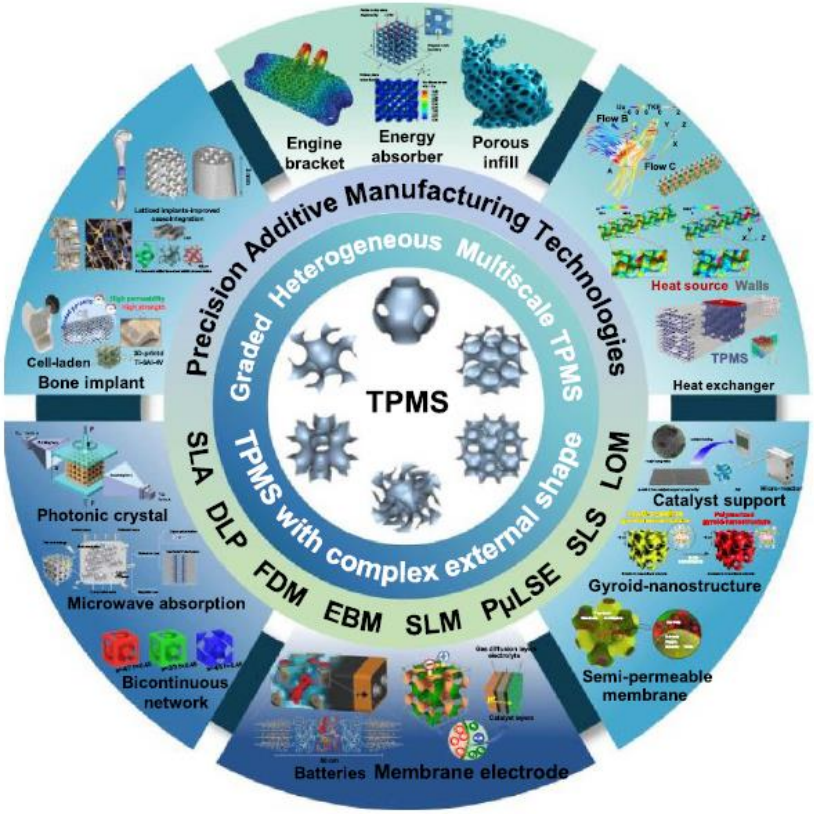

Figure 14. AM Technologies, and Multifunctional Applications of TPMS structures [7].

The Gyroid is one of the most widely studied TPMS structures. It is smooth, periodic, interconnected, and has been investigated using both experimental testing and finite element modeling. Gyroid structures can provide competitive stiffness, compressive strength, and energy absorption compared with other TPMS structures [7,47,51]. Gyroid lattices fabricated from 316L stainless steel have also shown promising behavior in quasi-static compression, dynamic compression, biomedical scaffold design, and energy absorption studies. However, Gyroid performance depends on relative density, wall thickness, material, manufacturing accuracy, and loading condition [37,49,50,52–54].

Split-P is another surface-based lattice architecture related to the TPMS family. Compared with more widely studied TPMS topologies such as Gyroid and Diamond, Split-P has received less attention in the literature. Nevertheless, it is relevant because it provides interconnected porosity and controllable wall geometry [55]. Its inclusion in this thesis allows comparison with Gyroid structures under the same material and manufacturing route.

The comparison between different surface-based lattices is important because topology influences load-path distribution, stiffness, collapse behavior, and energy absorption. Even when two structures have the same designed relative volume, their internal geometry may distribute stress differently [37,47]. Therefore, mechanical behavior should be evaluated experimentally and numerically rather than inferred only from nominal relative density.

1.6 Stochastic Voronoi Lattices and Bioinspired Porous Architectures

Stochastic Voronoi lattices represent a different architectural concept from TPMS structures. While TPMS structures are periodic and mathematically smooth, Voronoi lattices are based on irregular cellular partitions. This gives them a more random or foam-like internal geometry, which can imitate natural porous systems such as trabecular bone. Because of their irregularity, Voronoi structures can be useful where a more biomimetic or non-periodic architecture is desired [43–45].

Voronoi-based porous structures have been studied for implant design, stress transfer, and compressive behavior. Their irregular cellular networks can provide design flexibility because local cell size, randomness, and relative density can be adjusted. However, irregularity may also produce complex local stress distributions and less predictable collapse behavior compared with periodic TPMS structures. Therefore, the mechanical response of Voronoi structures must be evaluated carefully, especially when compared with smoother surface-based lattices [43–45].

The inclusion of a stochastic Voronoi lattice in the present thesis is important because it provides a contrast to the Gyroid and Split-P architectures. Gyroid and Split-P represent surface-based periodic or TPMS-derived structures, while the stochastic Voronoi specimen represents an irregular cellular architecture, as illustrated in Figure 15. Comparing these architectures under the same material, manufacturing route, and relative-volume level allows a more meaningful discussion of how architecture influences mechanical response.

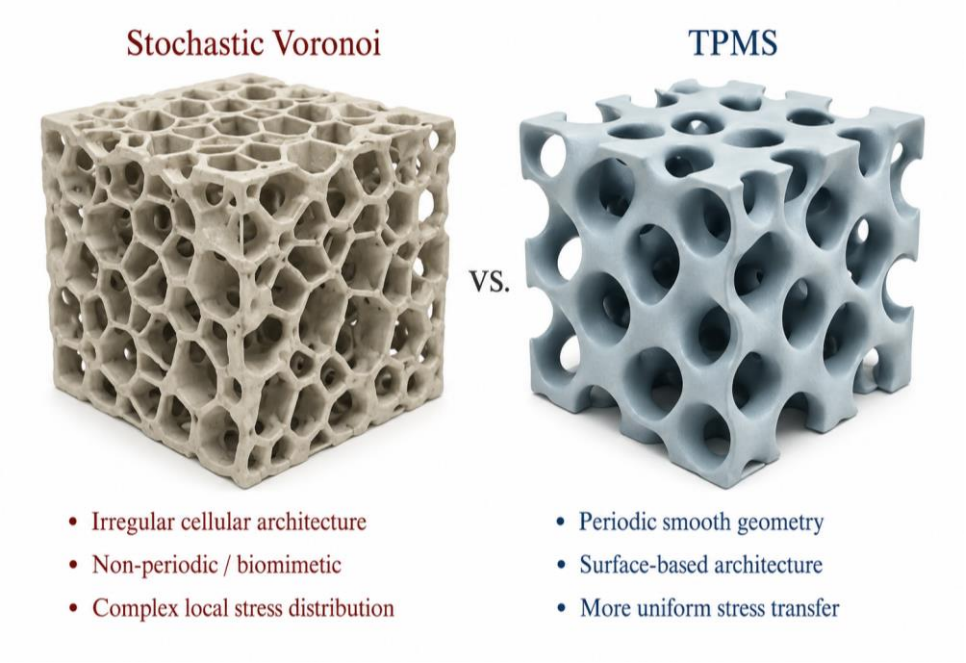

Figure 15. Comparison of Voronoi-Based and TPMS Architectures for Porous Structures [Created by the author using AI-assisted graphic generation].

1.7 Uniform, Graded, and Relative-Volume-Based Lattice Design

Lattice structures can be designed as uniform or graded architectures. In uniform lattices, parameters such as relative density, wall thickness, cell size, or strut diameter remain approximately constant throughout the specimen. Uniform designs are useful for studying the intrinsic mechanical behavior of a topology because the geometry is consistent throughout the volume [37,47]. In graded lattices, one or more geometrical parameters vary spatially, as shown in Figure 16, allowing local stiffness, strength, or porosity to change within the structure.

Functionally graded lattices can be designed by varying wall thickness, strut diameter, cell size, cell type, amplitude, or local relative density. This can create smoother mechanical transitions, reduce stiffness mismatch, delay localized collapse, or improve energy absorption [13–16,38]. In biomedical applications, graded porosity may reduce stress shielding and improve biological compatibility [5,18,19]. In energy absorption applications, grading can promote progressive collapse and extend the useful deformation range [6,13–16,38].

However, grading does not automatically improve performance. If the graded architecture contains very thin regions, the structure may become more difficult to manufacture accurately. Defects may become more influential in low-density regions, and deformation may localize where stiffness is lowest. Therefore, graded lattice designs must be evaluated experimentally and not only through nominal CAD models [3,13,37,38]. Manufacturing quality and real geometry must be considered together with the intended grading strategy [37,56].

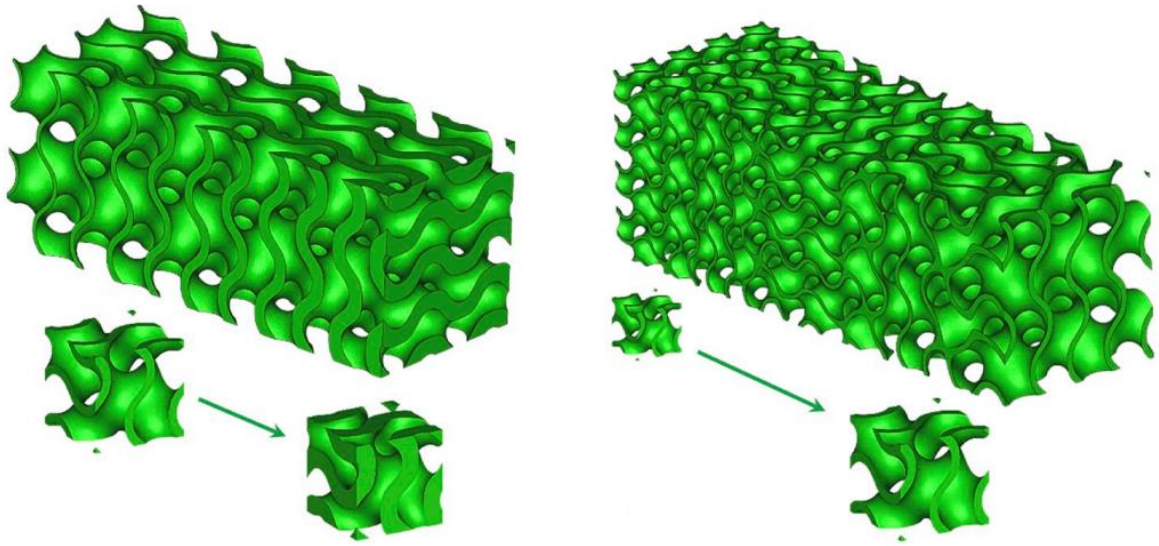

(a) (b)

Figure 16. Functionally Graded Gyroid Lattices. a) Relative Density Grading and b) Cell Size Grading [14].

In the present thesis, selected Gyroid, Split-P, and stochastic Voronoi architectures are investigated to compare different lattice concepts under the same material system and manufacturing route. The selected group allows the influence of lattice topology and spatial material distribution to be considered while maintaining a controlled relative-volume condition. This approach avoids mixing too many variables at the same time and provides a focused basis for interpreting the effect of material behavior, internal quality, and numerical modeling assumptions on the compressive response.

1.8 Digital Design Workflow for Lattice Specimens

The mechanical behavior of lattice structures is strongly governed by the way material is distributed inside the design volume. For this reason, lattice design cannot be treated only as a visual or geometrical task. Parameters such as topology, unit-cell size, cell mapping, wall or strut thickness, relative volume, and spatial thickness variation directly influence stiffness, collapse behavior, energy absorption, and manufacturability [1–7,37,47,48].

In the present work, the lattice compression specimens were designed using nTop. This software was selected because implicit and field-driven modeling are suitable for complex lattice geometries, especially when the geometry contains periodic TPMS surfaces, stochastic cellular networks, variable wall or strut thickness, and controlled relative-volume classes [57]. Compared with conventional CAD workflows, implicit modeling allows complex porous architectures to be generated and modified more efficiently, which is particularly important for structures that contain repeated cells, smooth internal surfaces, or irregular cellular regions [7,37].

The design workflow was based on the definition of the external compression-specimen volume, followed by the generation of the internal lattice architecture. Gyroid and Split-P structures were designed as surface-based lattice configurations, while the stochastic Voronoi architecture was generated as an irregular cellular network. For the periodic structures, the internal architecture was controlled by topology, cell mapping strategy, unit-cell dimensions, and wall thickness. For the stochastic architecture, the distribution of seed points and the resulting cellular network controlled the internal geometry [43–45].

Relative volume was used as a key design parameter to organize the compression specimens. By adjusting the wall thickness, different relative-volume classes were obtained while maintaining the intended external specimen dimensions. This allowed the influence of architecture and material distribution on compression behavior to be investigated [13–16,37,38]. The full specimen set was designed for experimental compression testing, while a group with same relative-volume was selected for detailed XCT inspection and Abaqus-based numerical validation.

After the design stage, the lattice models were exported as STL files for LPBF manufacturing and later used as the basis for numerical model preparation. In this way, the digital design workflow connected the main stages of the thesis: geometry generation, additive manufacturing, WEDM separation, XCT characterization, compression testing, and finite element simulation.

1.9 Post-Processing and Separation from the Build Platform

After LPBF fabrication, metallic parts are usually attached to the build platform and must be separated before characterization or testing. For dense components, several cutting methods may be possible. For lattice structures, however, the separation step must be performed carefully because thin walls, delicate surfaces, and internal porous geometry can be damaged by excessive mechanical forces. Damage introduced during removal could influence XCT inspection, compression testing, and interpretation of mechanical behavior.

Wire Electrical Discharge Machining (WEDM) is suitable for cutting conductive metallic components because material removal occurs through controlled electrical discharges rather than conventional cutting forces. In WEDM, a continuously fed wire electrode follows a programmed path, while dielectric fluid removes debris and stabilizes the cutting region. Since the tool does not apply conventional mechanical cutting forces in the same way as milling or sawing, WEDM is useful for delicate parts, thin-walled components, and hard-to-machine materials.

For LPBF lattice structures, WEDM is particularly useful because it can separate specimens from the build platform while reducing the risk of damaging the lattice architecture [58]. The separation process is shown in Figure 17. This is important because the mechanical response measured during compression should reflect the behavior of the printed structure, not damage caused by post-processing. In the present thesis, WEDM is used before XCT inspection and compression testing of the lattice specimens.

Figure 17. Lattice Separation from Build Platform using WEDM [Image taken during specimen preparation].

1.10 X-ray Computed Tomography (XCT) Evaluation

The difference between nominal geometry and as-built geometry is a critical issue in LPBF lattice structures. The nominal STL or CAD file represents the intended geometry, but the printed part may contain deviations caused by powder spreading, laser melting, thermal distortion, surface roughness, powder adhesion, and limited process resolution. These deviations can affect wall thickness, pore size, local curvature, connectivity, and effective relative volume [3,17,37]. Therefore, the actual printed geometry must be evaluated before drawing conclusions about mechanical behavior [37,56].

Unintended porosity in LPBF may originate from different mechanisms. Lack-of-fusion porosity is commonly associated with insufficient energy input, poor overlap between scan tracks, or incomplete bonding between layers. Keyhole porosity is generally associated with excessive energy input, vaporization, and unstable melt-pool behavior. Gas porosity may occur due to trapped gas in the powder or melt pool. Partially melted or unmelted powder particles may also remain attached to surfaces or trapped inside complex lattice geometries [17,23,35,37].

In lattice structures, such defects can have a significant influence on mechanical response. Because the load-bearing walls or struts are small, a local pore or lack-of-fusion region can represent a meaningful reduction in local cross-section. Surface roughness can also act as a local stress concentrator and may affect collapse initiation [3,23,36]. This is particularly important for surface-based lattices, where the walls are curved and many critical regions are located inside the structure [37,56].

XCT is one of the most useful methods for evaluating LPBF lattice structures because it provides non-destructive three-dimensional information about internal and external geometry. XCT can detect internal pores, defect distribution, pore size, maximum pore diameter, and geometry deviations without cutting the specimen [41,56]. This is particularly valuable for TPMS and stochastic lattice structures because many surfaces are internal and cannot be inspected by simple optical methods.

XCT can also be used to compare nominal and as-built geometries. This comparison is important because the real printed structure may have different wall thickness, surface roughness, or local defects compared with the design model. These deviations may explain differences between predicted and measured stiffness, strength, or energy absorption [3,37,56]. Therefore, XCT is not only a quality-control tool but also a link between manufacturing and mechanical performance [41,56].

In some studies, XCT data can also be used to build more realistic finite element models. Such models include as-built geometry and can improve the relationship between simulation and experiment. However, XCT-based modeling requires image segmentation, surface reconstruction, and complex meshing, which increases computational cost. Therefore, ideal CAD or STL-based models are still widely used, while XCT is used to interpret deviations between simulations and experiments [54,56].

In the present thesis, XCT is used to inspect the selected stainless steel 316L lattice specimens. The XCT analysis provides information about internal porosity, defect distribution, and geometrical fidelity, which supports the interpretation of compression-test results and finite element comparisons.

1.11 Compression Behavior and Mechanical Characterization

Compression testing is one of the most common methods used to evaluate cellular and lattice structures. Many potential applications of lattice structures involve compression or crushing loads, including energy absorbers, biomedical implants, lightweight supports, protective structures, and sandwich cores. Under compression, lattice structures generally show an initial elastic region, followed by collapse or plateau-like deformation, and finally densification at larger strains [1,3,6,37,47,59].

The initial elastic region provides information about the effective stiffness of the lattice. Because part of the specimen volume is occupied by pores, the effective modulus of a lattice structure is lower than that of the fully dense parent material. This modulus depends on relative density, topology, wall thickness, material behavior, and manufacturing quality. In LPBF lattices, roughness, dimensional deviations, and internal defects may further reduce stiffness compared with ideal geometry [1,3,23,37].

After the initial elastic region, the structure enters a collapse or plateau-like region. In this stage, deformation can occur through bending, buckling, plastic yielding, fracture, layer-wise collapse, or progressive folding depending on topology and material behavior. A stable plateau is desirable for energy absorption because it allows the structure to absorb energy

over a large deformation range without a sudden increase in stress. However, some lattice structures may show unstable collapse, sudden stress drops, or localized deformation depending on architecture and defects [1,37,47].

At larger strain levels, densification occurs when internal pores close and solid regions begin to contact each other. During densification, stress increases rapidly because the structure behaves increasingly like a compacted solid. Densification strain is important because it defines the useful deformation range for energy absorption [1,37]. Structures that densify too early may absorb less energy efficiently, while structures that maintain stable deformation before densification may show better energy-absorbing performance [37,47]. These three phases, together with a schematic compression-test configuration, are shown in Figure 18.

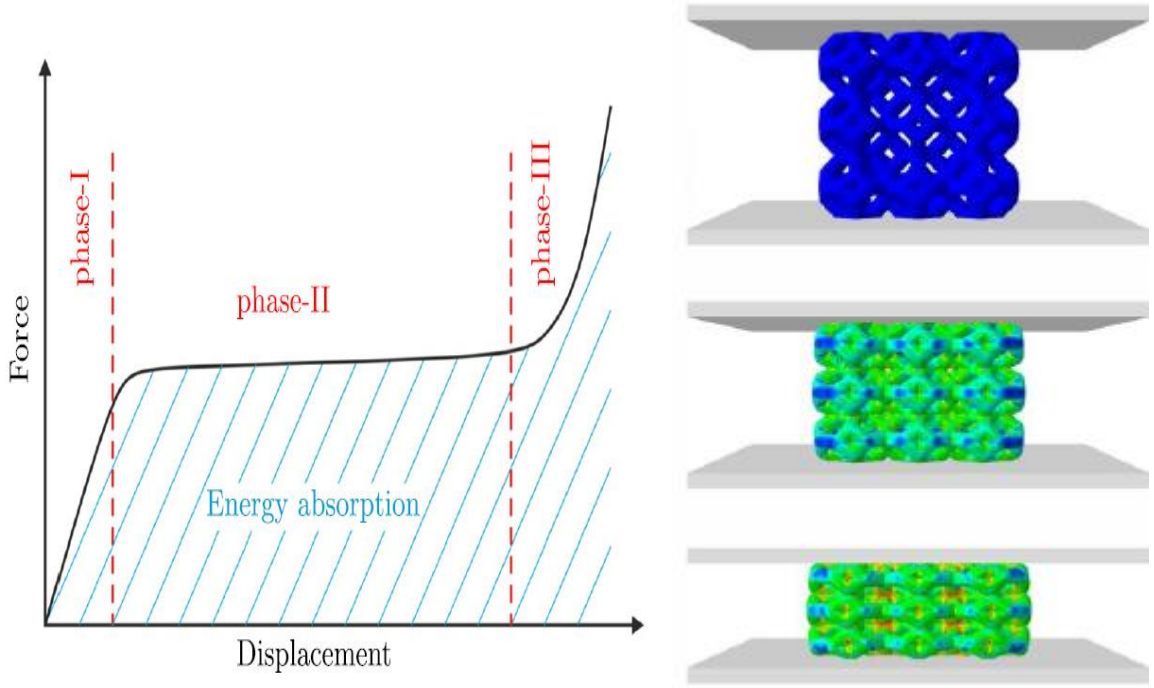

Figure 18. Typical Force-Displacement Diagram and Schematic of Compression Test for Cellular Structures [60].

Several mechanical indicators can be extracted from compression tests, including effective elastic modulus, maximum compressive stress, plateau stress, absorbed energy, specific energy absorption, and densification strain. Absorbed energy is calculated as the area under the stress–strain curve up to a selected strain level. Specific energy absorption normalizes absorbed energy by mass or density, allowing comparison between structures with different masses or relative densities. This is important in lightweight design because the best structure

is not always the strongest one, but the one with the best performance relative to its weight [1,37,47,59].

The compressive behavior of 316L lattice structures has been investigated in several contexts, including BCC lattices, diamond lattices, Gyroid structures, TPMS sheets, and functionally graded architectures. These studies show that relative density, topology, unit cell size, build orientation, and modeling assumptions can significantly influence stiffness, yield strength, deformation pattern, and energy absorption [20,21,40,49,50,52–54]. In the present thesis, quasi-static compression testing is used to evaluate the Gyroid, Split-P, and stochastic Voronoi lattice specimens fabricated from stainless steel 316L.

1.12 Finite Element Simulation and Numerical Validation

Finite Element Analysis (FEA) is widely used to predict and interpret the mechanical behavior of lattice and TPMS structures. Numerical simulation provides information that cannot be fully obtained from experimental curves alone, including stress distribution, plastic strain localization, deformation sequence, contact behavior, and collapse mechanisms. For complex lattice geometries, FEA is particularly useful because internal stress states and deformation patterns are difficult to observe directly during testing [37,51,54,56,61].

In compression simulations, the lattice specimen is commonly modeled between two rigid or analytical plates. The lower plate is fixed, while the upper plate is displaced downward to reproduce the experimental compression test. This configuration is illustrated in Figure 19 [51,54,56,61]. Reaction force can be extracted from the moving plate and compared with experimental force–displacement data [54,56]. Stress and strain fields can be used to identify critical regions and explain deformation mechanisms [37,54].

The accuracy of FEA depends on several modeling choices. The first major choice is the geometry used in the model. Ideal CAD or STL-based models are easier to mesh and simulate, but they do not include surface roughness, internal pores, or dimensional deviations. XCT-based models can represent the real printed structure more accurately, but they require segmentation, reconstruction, and more complex meshing. Therefore, the choice between ideal and as-built geometry depends on the purpose and complexity of the analysis [37,51,54,56,61].

Mesh strategy is also important for TPMS and lattice structures. Thin-walled surface-based lattices may be modeled using shell elements, while thicker or more complex geometries may require solid or voxel-based elements [37]. Mesh size influences both accuracy and computational cost. A mesh that is too coarse may not capture local curvature or stress concentration, while a very fine mesh may become computationally expensive. Therefore, mesh generation is a key step in the numerical workflow [37,48,51,61].

In the present thesis, a mesh convergence study is performed before the final Abaqus simulations. Several mesh sizes are compared, and the final mesh is selected by balancing the stability of the predicted force–displacement response with computational cost.

Material modeling is another important aspect. Stainless steel 316L produced by LPBF may show anisotropic plasticity, strain hardening, and fracture behavior depending on build orientation and stress state [33,40,54]. However, simplified isotropic elastic–plastic material models are often used in global lattice simulations to make the analysis computationally manageable. Such simplifications may reproduce global force–displacement trends but may not capture local fracture or anisotropic material response [40,54]. Therefore, assumptions of the material model must be clearly discussed.

Contact and boundary conditions can also strongly affect numerical predictions. Friction between compression plates and specimen can influence lateral deformation and collapse behavior. Boundary conditions may influence reaction force, deformation pattern, and stress distribution. Full-specimen models are generally more representative than single-cell models, but they require higher computational resources. Therefore, numerical models should be validated against experimental data rather than treated as automatically reliable [37,54].

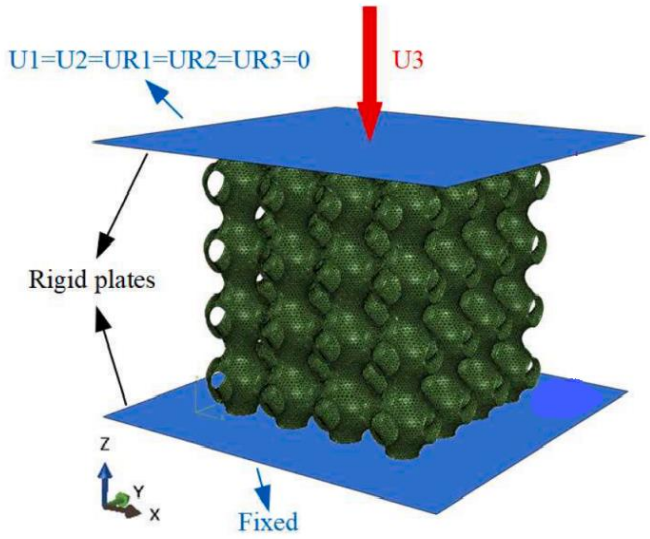

Figure 19. Finite Element Simulation of Lattice Structure **[37].**

In the present thesis, finite element models are developed to simulate the compression behavior of the selected lattice specimens and a bulk reference geometry. The objective of the numerical analysis is not only to reproduce the experimental force–displacement response, but also to identify possible causes of agreement or deviation between numerical predictions and experimental behavior, including idealized geometry, internal defects, simplified material behavior, contact assumptions, and mesh quality.

1.13 Research Gap and Positioning of the Present Work

The literature shows that LPBF is a powerful process for producing complex metallic structures, including lattice and TPMS architectures [3,11,12,37]. Stainless steel 316L is a

relevant LPBF material because of its corrosion resistance, ductility, processability, and mechanical properties [17,23,33,40]. TPMS structures are promising because of their smooth surfaces, interconnected porosity, and compression behavior [7,37,47]. Stochastic Voronoi lattices provide a useful contrast because they represent a more irregular and bioinspired porous architecture [43–45].

Despite the extensive literature on LPBF, 316L stainless steel, TPMS lattices, Voronoi structures, XCT characterization, compression testing, and finite element modeling, several aspects remain important for the present work. First, the same lattice architecture may behave differently when the base material changes because material density, stiffness, yield behavior, ductility, strain hardening, and defect sensitivity influence the global response of lattice structures [17,23,33,40]. Therefore, the mechanical behavior of a lattice architecture cannot be fully generalized without considering the material system.

Second, real LPBF-fabricated lattice structures can contain surface roughness, porosity, dimensional deviations, and local manufacturing defects. These features may strongly influence stiffness, collapse behavior, and energy absorption [3,17,23,37]. Therefore, the actual printed geometry and internal quality must be evaluated experimentally rather than relying only on nominal STL geometry [37,56].

Third, numerical models often use ideal geometries and simplified material behavior. These assumptions may lead to differences between simulation and experiment, especially for complex lattice structures manufactured by LPBF. Therefore, FEM results should be interpreted through experimental validation and through awareness of model limitations [37,54].

The present thesis addresses these issues by designing Gyroid, Split-P, and stochastic Voronoi compression specimens in nTop and fabricating them from stainless steel 316L using LPBF. The full set of compression specimens is evaluated through quasi-static compression testing, while a group with the same relative-volume is further characterized by XCT and simulated using Abaqus. A bulk specimen is included as a numerical dense reference. The thesis is therefore positioned as a design–manufacturing–testing–simulation study of LPBF-fabricated 316L lattice structures, with emphasis on the relationship between architecture, relative volume, internal quality, compressive response, and numerical predictability.

1.14 Aim and Objectives

The main aim of this thesis is to design, fabricate, experimentally characterize, and numerically validate LPBF-fabricated stainless steel 316L lattice structures based on Gyroid, Split-P, and stochastic Voronoi architectures. The full set of compression specimens is evaluated experimentally, while XCT inspection and Abaqus validation are focused on a group of same relative-volume lattice specimens.

The specific objectives are:

1. To design the lattice specimens in nTop by controlling topology, cell mapping, wall thickness, and relative-volume class.
2. To fabricate all lattice specimens two times, from stainless steel 316L using LPBF.
3. To separate the printed specimens from the build platform using WEDM.
4. To evaluate internal porosity, defect distribution, and geometrical fidelity of a specific group of same relative-volume specimens using XCT.
5. To perform quasi-static compression testing two times on the full specimen set, to make sure that the results are reliable enough.
6. To develop Abaqus finite element models for a group of same relative-volume lattice specimens.
7. To validate the numerical response by comparing Abaqus predictions with experimental compression-test results.
8. To discuss the influence of lattice topology, relative volume, manufacturing quality, material behavior, and modeling assumptions on the compressive response of LPBF-fabricated 316L lattice structures.

1.15 Thesis Structure

This thesis is organized into five main chapters. Chapter 1 introduces the transition from conventional design to architected design, including AM, LPBF, stainless steel 316L, lattice structures, TPMS and stochastic Voronoi architectures, uniform and relative-volume-based lattice design, digital design workflow, WEDM separation, XCT characterization, compression testing, finite element validation, research gap, and objectives. Chapter 2 presents the state of the art related to LPBF processing, 316L stainless steel, additively manufactured lattice structures, TPMS and stochastic Voronoi architectures, graded lattices, digital lattice design and nTop-based modeling, XCT-based quality evaluation, compression behavior, and numerical modeling. Chapter 3 describes the materials and methods, including nTop-based design of the lattice specimens, stainless steel 316L powder and material properties, LPBF fabrication, WEDM separation, experimental repeatability, XCT inspection, quasi-static compression testing of the full sample set, data processing, and Abaqus simulation setup. Chapter 4 presents and discusses the experimental and numerical results, including compression behavior of the full sample set, XCT-based quality evaluation, Abaqus predictions, and experimental–numerical validation. Chapter 5 summarizes the main conclusions of the work and proposes possible directions for future research.

Chapter 2

State of the Art

Chapter 1 introduced the general context of architected materials, LPBF, stainless steel 316L, TPMS and stochastic Voronoi lattices, XCT inspection, compression testing, and finite element validation. To avoid repeating the introductory explanations, this chapter focuses on the published research that is most directly connected to the present thesis. The review is organized around the variables that control the behavior of LPBF-fabricated lattice structures: process-parameter sensitivity, 316L material response, defect formation, lattice topology, TPMS and Voronoi architectures, grading strategies, XCT-based quality evaluation, compression testing, and numerical modelling. The aim is to position the present experimental-numerical study within the existing literature, rather than to provide a broad historical overview of AM.

The present thesis investigates nTop-designed Gyroid, Split-P, and stochastic Voronoi lattice structures fabricated from stainless steel 316L using LPBF. The full compression sample set is experimentally tested, while XCT inspection and Abaqus-based validation are focused on a same relative-volume group. Therefore, the state of the art is not limited to one single topic. It must connect four research streams that are often discussed separately: metallic LPBF processing, mechanical behavior of lattice structures, quality evaluation of as-built geometries, and finite element simulation of cellular materials. This chapter reviews these streams with emphasis on how they affect the interpretation of quasi-static compression results and the comparison between experimental and numerical responses.

2.1 LPBF Process-Structure-Property Relationships in Metallic Materials

LPBF is widely used for the fabrication of complex metallic components because it allows the direct production of geometries that are difficult or impossible to obtain by conventional manufacturing. However, the process is governed by strong interactions between laser energy input, powder-bed behavior, melt-pool dynamics, solidification, residual stress, surface quality, and defect formation [11,12,17,23,24,62–67]. For dense parts, the main target is usually to maximize density and mechanical reliability. For lattice structures, the same issues become even more critical because load-bearing walls or struts are small and defects may occupy a significant fraction of the local cross-section [3,23,30,37].

Early work on laser sintering and laser melting emphasized that the final bonding mechanism depends on the way thermal energy interacts with the powder feedstock and the surrounding material [62]. In LPBF of metals, full melting is generally required to produce metallurgical bonding between layers, but the process window is narrow. If energy input is insufficient, lack-of-fusion defects and weak interlayer bonding may occur. If energy input is excessive, vaporization, spatter, deep keyholes, and unstable melt pools may develop [17,23,24,32,63–67]. Therefore, process optimization cannot be reduced to choosing the highest energy input. A stable balance between complete melting and melt-pool stability is required.

Powder-scale simulations and in-situ observations have provided important insight into the physical origin of LPBF defects. Khairallah et al. showed that recoil pressure, Marangoni convection, melt-pool instability, spatter, and denudation zones can all contribute to pore formation and surface irregularity in LPBF of 316L stainless steel [63]. King et al. experimentally observed keyhole-mode laser melting in LPBF and showed that deep vapor depressions can form voids in the wake of the laser beam [64]. Matthews et al. further showed that metal powder can be denuded from regions near the scan track, which changes local powder availability and can influence the next layer [65]. Cunningham et al. used high-speed X-ray imaging to identify keyhole threshold and morphology during laser melting, confirming that pore formation can be linked to the stability of the vapor depression [66]. These studies explain why nominally simple parameter changes can strongly alter part quality.

The use of volumetric energy density is common in LPBF literature because it combines laser power, scan speed, hatch spacing, and layer thickness into one engineering indicator. However, several studies have shown that VED alone is not a complete descriptor of the process [17,23,24,67]. Oliveira et al. reviewed the role of processing parameters in LPBF and emphasized that equal energy density values may generate different thermal histories, melt-pool geometries, residual stresses, porosity levels, surface conditions, and microstructures [67]. This is important for the present thesis because lattice specimens should not be interpreted only by their nominal relative volume or CAD geometry; their response also depends on how the LPBF process actually produced the thin walls, curved surfaces, and internal features.

2.2 LPBF of Stainless Steel 316L

Stainless steel 316L is one of the most studied alloys in LPBF because it combines corrosion resistance, ductility, weldability, and industrial relevance [17–19,23,24,30,33,36,39,68–71]. In conventionally manufactured form, 316L is already a useful engineering alloy. Under LPBF conditions, however, the material experiences repeated rapid melting and solidification cycles, which can produce refined cellular or columnar microstructures, melt-pool boundaries, residual stresses, and anisotropy. Therefore, LPBF 316L cannot be treated as a direct equivalent of wrought 316L.

Cherry et al. investigated the effect of SLM process parameters on the microstructural and physical properties of 316L stainless steel and showed that laser energy density influences porosity, density, surface finish, microstructure, and hardness [68]. Liverani et al. similarly demonstrated that SLM process parameters affect the microstructure and mechanical properties of 316L austenitic stainless steel [69]. These works support the idea that the material response of LPBF 316L is process-dependent. The same nominal alloy can show different behavior if the process window, scanning strategy, or local thermal history changes.

Several studies have reported that LPBF or laser-melted 316L can present higher yield strength than conventionally processed 316L. Ma et al. compared SLM and laser cladding deposition of 316L and reported that the smaller melt pools and higher cooling rates in SLM produce finer microstructural features [19]. Saeidi et al. described laser-melted 316L as a hardened austenitic steel with a columnar sub-grain structure, linking the refined solidification structure to increased strength [70]. Suryawanshi et al. also showed that selective laser melted 316L can have significantly higher yield strength than conventionally manufactured 316L, although ductility and anisotropy must also be considered [33].

The improved strength of LPBF 316L does not eliminate concerns related to defects and material variability. Riemer et al. investigated fatigue crack growth in SLM 316L and highlighted the importance of microstructure and defect population in crack initiation and propagation [71]. Crisafulli et al. discussed microstructure, porosity, surface characteristics, and fatigue behavior of LPBF 316L, showing that process-induced imperfections remain relevant even when the alloy has useful static mechanical properties [18]. Liu et al. further showed that LPBF 316L may require anisotropic plasticity and fracture descriptions when stress state and loading rate are important [39]. For this thesis, such observations justify the use of experimental compression data to validate numerical simulations rather than assuming that a simplified material model is automatically sufficient.

Feature size is another key issue in LPBF 316L lattices. Puttonen et al. showed that fine TPMS lattice features can locally affect microstructure, surface condition, entrapped powder, and corrosion susceptibility in 316L lattices [30]. This type of finding is relevant beyond corrosion: thin lattice walls and struts are more sensitive to roughness, local overmelting, lack-of-fusion defects, and dimensional deviations. Therefore, when 316L is used in lattice form, the mechanical performance is controlled by the combination of alloy response, LPBF manufacturing quality, and structural topology.

2.3 Density, Porosity, Surface Quality, and Defect Measurement

Density and porosity measurement are central to LPBF quality assessment. Spierings et al. compared density measurement techniques for additively manufactured metallic parts and showed that different methods may not always give identical results because they capture different aspects of the material and defect structure [72]. For lattice structures, this issue is even more complex because there is a distinction between designed porosity and unintended manufacturing porosity. The designed voids define the lattice architecture, while unintended pores inside walls or struts represent defects.

In dense 316L specimens, porosity is often analyzed as a percentage of the total volume. In lattice structures, the local meaning of a defect can be more severe. A pore that is small relative to the whole specimen may be large relative to a thin wall, strut, or node. This explains why LPBF lattice structures often require a stronger connection between manufacturing quality and mechanical interpretation than dense coupons [3,23,30,37,56]. Moreover, roughness and attached powder particles increase the effective surface irregularity of the structure, influencing both load transfer and local stress concentration.

Surface quality and dimensional accuracy are also important because the mechanical response of a lattice is controlled by its real load-bearing geometry. Roughness, local overmelting, lack-of-fusion defects, and powder adhesion can change the effective wall thickness, local curvature, and stress concentration of thin features [3,17,23,30,37,56]. Therefore, defect measurement in lattice structures should not be treated only as a material-density problem. It should also be connected to the as-built geometry, surface condition, and local structural scale of the lattice.

2.4 Mechanical Behavior of Additively Manufactured Lattice Structures

The mechanical behavior of lattice structures is governed by relative density, topology, unit-cell size, material behavior, local defects, and boundary conditions [1–6,20,21,37,42,73–77]. Compared with dense solids, lattice structures usually show lower effective modulus and strength because part of the volume is intentionally occupied by pores. However, their specific properties and energy absorption performance can be advantageous when mass reduction and controlled deformation are required [1,3,6].

Early studies on SLM lattice structures demonstrated the potential of additive manufacturing for producing periodic cellular architectures. Yan et al. evaluated cellular lattice structures manufactured using selective laser melting and showed that manufacturability, geometric accuracy, and mechanical behavior are closely related [73]. Gümrük and Mines investigated 316L stainless steel micro-lattice structures under compression and showed that strut overlap near nodes affects stiffness and strength predictions [74]. Smith et al. developed finite element models for compressive response of SLM lattice structures and compared beam and continuum modelling approaches [75]. These studies remain important because they show that the mechanical response of a lattice cannot

be predicted only from simple unit-cell geometry; manufacturing deviations and modeling assumptions must be included.

Lattice deformation under compression often includes an initial elastic region, followed by plastic collapse or buckling, and then densification [1,3,6,59]. The shape of the stress-strain or force-displacement curve depends on whether the topology is stretching-dominated, bending-dominated, or shell-based. Stretching-dominated structures can provide higher stiffness and strength but may show a sharper collapse after the peak load. Bending-dominated structures often show lower stiffness but may produce a longer plateau region, which is useful for energy absorption. These general categories are helpful, but real LPBF lattices may deviate from ideal behavior because of roughness, dimensional errors, local porosity, and imperfect boundary contact.

Functionally graded lattices have received attention because spatial variation of density, wall thickness, strut diameter, or unit-cell size can control deformation sequence and stress transfer. Choy et al. studied functionally graded lattice structures manufactured by SLM and showed that grading can modify compressive behavior compared with uniform lattices [76]. Yang et al. also demonstrated that continuous graded Gyroid structures can show different compression responses depending on gradient direction and morphology [13]. However, grading is not automatically beneficial. If local relative density becomes too low, manufacturing imperfections may become more influential and collapse may localize in weaker regions [13–16,38,76].

Energy absorption is a key motivation for lattice design. Maskery et al. studied double gyroid lattices and showed that geometry and failure mode strongly influence energy absorption under compression [77]. Zhang et al. reported high energy absorption potential for metallic TPMS sheet structures under compressive loading [22]. Bieler and Weinberg further highlighted the importance of comparing lattice structures in terms of energy absorption under static compression [60]. These studies indicate that the best lattice for energy absorption is not necessarily the stiffest or strongest structure, but the one that combines stable collapse, delayed densification, sufficient plateau stress, and efficient mass use.

2.5 TPMS Structures: Design, Manufacturability, and Mechanical Response

TPMS structures have attracted strong interest because they combine periodicity, smooth continuous surfaces, high interconnectivity, and controllable geometrical parameters [7,22,37,47–50,77–79]. Unlike conventional strut-based lattices, sheet-based TPMS structures are formed by thickening mathematically defined surfaces. This eliminates sharp node-like junctions and can reduce local stress concentration. In addition, the connected pore network makes TPMS structures useful for applications involving fluid flow, heat transfer, and biomedical integration [7,22,49,78,79].

Feng et al. reviewed TPMS porous structures from design, manufacturing, and application perspectives and emphasized that TPMS geometries can be controlled through implicit functions, unit-cell size, wall thickness, level-set parameters, and grading [7]. Zhang et al.

studied metallic TPMS sheet structures fabricated by SLM and showed that Primitive, Diamond, and Gyroid architectures have different stiffness, plateau stress, collapse mechanisms, and energy absorption behavior [22]. Qiu et al. compared several TPMS structures using experiments and finite element simulations and demonstrated that topology and relative density strongly affect energy absorption and stress distribution [37]. These works show that TPMS structures should not be treated as one uniform category; individual topology matters.

The Gyroid is one of the most widely studied TPMS architectures. Abueidda et al. investigated polymeric Gyroid structures experimentally and numerically and showed that Gyroid topology can provide competitive mechanical behavior compared with other TPMS structures [47]. Ma et al. studied 316L gyroid scaffolds produced by SLM and reported that volume fraction influences elastic modulus, yield stress, and transport properties [49]. Fu et al. demonstrated that micro-LPBF can improve lightweighting potential for SS316L TPMS shell lattices by enabling smaller feature sizes [50]. Li et al. analyzed SLM-printed Gyroid structures under dynamic compression and used numerical simulations to interpret deformation and energy absorption mechanisms [53].

In biomedical contexts, TPMS architectures have been studied because they can combine permeability, surface area, and mechanical compatibility. Melchels et al. showed that mathematically defined scaffold architectures can be manufactured with controlled pore geometry and tailored mechanical behavior [79]. Bobbert et al. designed additively manufactured metallic porous biomaterials based on minimal surfaces and showed that TPMS-based porous metals can combine bone-mimicking topology, mechanical response, fatigue resistance, and mass transport properties [78].

Split-P is less widely represented in the literature than Gyroid, Diamond, and Primitive structures. Rezapourian et al. studied selective laser melted Ti6Al4V Split-P TPMS lattices for bone tissue engineering and showed that Split-P can be considered a relevant surface-based porous architecture with controllable mechanical and biological potential [55]. Its limited presence in the literature is one reason why direct comparison with Gyroid and stochastic Voronoi lattices is useful. In the present thesis, Split-P is not treated as a general TPMS example but as a specific architecture whose response must be compared experimentally and numerically under the same material and manufacturing framework.

2.6 Stochastic Voronoi and Bioinspired Porous Architectures

Stochastic Voronoi lattices represent a different design logic from periodic TPMS structures. Instead of being generated from smooth periodic surfaces, Voronoi architectures are based on irregular cellular partitions. This makes them attractive when the goal is to imitate natural porous systems, such as trabecular bone, or when non-periodic architecture is desired [43–45,80,81].

Fantini et al. proposed a method to design biomimetic scaffolds for bone tissue engineering based on Voronoi lattices, showing that Voronoi diagrams can be used to control

pore size, porosity, and anatomical adaptation [80]. Zadpoor emphasized that scaffold geometry, including pore architecture, curvature, interconnectivity, and mechanical compatibility, plays a central role in bone tissue regeneration [81]. More recent studies have applied stochastic lattice-based porous designs to implant applications, stress transfer, and functionally graded biomedical structures [43,45]. Deng et al. investigated stochastic lattice-based porous implant design for improving stress transfer in unicompartmental knee arthroplasty [43]. Cheloni et al. compared body-centered cubic, Gyroid, Diamond, and Voronoi functionally graded biomedical lattice structures, showing that failure mode and mechanical behavior depend strongly on architecture [45].

The broader literature on additively manufactured porous metallic biomaterials also confirms that pore architecture and manufacturing route must be considered together. Campoli et al. showed that open-cell metallic biomaterials manufactured by AM can be mechanically tailored through their cellular architecture [82]. Hazlehurst et al. evaluated laser-melted square-pore CoCrMo cellular structures for orthopedic applications and showed that stiffness can be adjusted through the designed porous geometry [83]. Zadpoor later reviewed additively manufactured porous metallic biomaterials and emphasized the combined role of topology, processability, mechanical compatibility, and biological function [84]. These studies support the use of porous architecture as an engineering design variable rather than only a method of reducing mass.

Voronoi structures can offer design flexibility because cell size, randomness, and local density can be modified. However, this irregularity can also create complex local load paths and less predictable deformation compared with periodic lattices [44,45,80]. Colamartino et al. investigated compressive properties of three-dimensional Voronoi reticula and showed that the response of Voronoi networks is strongly influenced by the irregular cellular arrangement [44]. This makes Voronoi lattices interesting for comparison with TPMS structures: they may be more biomimetic, but their mechanical behavior can be more difficult to generalize.

The literature therefore suggests that stochastic Voronoi architectures should not be judged only by visual similarity to trabecular bone. Their mechanical performance must be assessed through actual testing and, when possible, numerical analysis. For the present thesis, the stochastic Voronoi specimen acts as a contrast to Gyroid and Split-P because it represents a non-periodic cellular architecture fabricated under the same material and process route. This comparison allows architecture to be discussed as a real design variable rather than as a purely visual category.

2.7 Uniform and Graded Lattice Design

Uniform lattice structures are useful for studying the intrinsic behavior of a topology because their relative density, unit-cell size, wall thickness, or strut diameter remain approximately constant. Graded lattices introduce spatial variation into one or more of these

parameters, allowing the designer to tune local stiffness, collapse sequence, permeability, or energy absorption [13–16,38,76].

Surface-based TPMS structures are especially suitable for grading because wall thickness, level-set value, amplitude, or unit-cell size can be varied continuously. Maskery et al. studied surface-based lattice structures with volume fraction and cell-type grading and showed that grading can be implemented numerically and experimentally to modify mechanical response [15]. Zhou et al. compared sheet- and network-based graded lattices manufactured by SLM and showed that design strategy and geometry family influence the final mechanical performance [16]. Ma et al. developed graded-amplitude Gyroid structures and demonstrated that amplitude variation changes deformation behavior, energy absorption, and anisotropy [38].

The effect of grading is not always straightforward. A graded structure may improve energy absorption by promoting progressive collapse, but it can also concentrate deformation if weak regions are too thin or poorly manufactured [13,38,76]. Moreover, grading increases the importance of manufacturing fidelity because local geometric deviations may change the intended density profile. For this reason, graded lattices should be interpreted through the combined effects of design, process quality, and mechanical testing rather than by nominal CAD parameters alone [3,37,56].

Although the full experimental program includes several relative-volume classes, the 79% group provides the controlled comparison level used for XCT analysis and Abaqus validation. The graded-lattice literature remains relevant because it shows how spatial material distribution affects mechanical response. Even when the overall relative volume is controlled, different topologies distribute material differently. Therefore, comparing Gyroid, Split-P, and stochastic Voronoi lattices within the 79% group provides insight into topology and spatial material arrangement without mixing too many additional design variables.

2.8 Digital Design and nTop-Based Lattice Modeling

The design of lattice structures for additive manufacturing requires tools that can control complex internal geometries with sufficient accuracy and flexibility. Conventional CAD software is effective for many solid components, but it can become inefficient when dealing with highly complex lattice architectures, especially when the geometry contains thousands of repeated cells, smooth TPMS surfaces, stochastic cellular regions, or spatially varying thickness. For this reason, implicit modeling and lattice-design platforms have become increasingly important in Design for Additive Manufacturing (DfAM) [3,7,37].

In lattice design, the final mechanical response is not defined only by the selected material. It is also controlled by topology, cell mapping strategy, unit-cell size, wall or strut thickness, relative volume, and spatial material distribution. These parameters determine how material is distributed inside the specimen and how loads are transferred during compression. Even when two specimens have similar relative volume, their stiffness, collapse behavior,

and energy absorption may differ because their internal load paths are different [1–7,37,47,48].

nTop is widely used for lattice and implicit-geometry design because it allows complex structures to be generated through field-driven and parameter-controlled workflows [57]. In this type of modeling environment, the designer can define the design volume, apply a lattice architecture, control cell size and orientation, adjust wall or strut thickness, and export the final geometry for additive manufacturing. This approach is particularly useful for TPMS-based structures because their geometry can be represented through continuous implicit surfaces rather than manually constructed solid features [7,37].

For surface-based TPMS structures such as Gyroid and Split-P, digital design enables the control of wall thickness, cell mapping, level-set parameters, and relative volume [7,37,47,48,55]. For stochastic Voronoi lattices, the design process is instead related to seed-point distribution, cell generation, and strut or wall definition [43–45]. These two design approaches are different, but both allow the creation of controlled porous architectures suitable for LPBF fabrication and mechanical testing.

From a DfAM perspective, lattice design must also consider manufacturability. Thin walls, narrow struts, overhanging surfaces, enclosed regions, and small internal channels may influence printability, powder removal, surface roughness, and dimensional accuracy [3,7,12,17,37]. Therefore, the digital design of lattice specimens should not be separated from the manufacturing process. The intended geometry, LPBF process limitations, post-processing method, and testing requirements must be considered together.

In the present thesis, nTop-based design is used to generate Gyroid, Split-P, and stochastic Voronoi compression specimens with controlled relative-volume classes. This design stage provides the geometrical basis for the following experimental and numerical work. The full set of designed specimens is fabricated by LPBF and tested under quasi-static compression, while the 79% relative-volume group is further investigated using XCT and Abaqus simulation. Therefore, the design workflow is directly connected to the interpretation of manufacturing quality, compressive behavior, and experimental–numerical validation.

2.9 XCT-Based Evaluation and As-Built Geometry in Lattice Studies

The difference between designed and as-built geometry is one of the main challenges in LPBF lattice research. Nominal CAD or STL files assume ideal surfaces, exact wall thickness, and perfect connectivity. Real LPBF components may contain rough surfaces, adhered powder, dimensional deviations, internal pores, and local defects [3,17,30,37,56]. These deviations can alter stiffness, collapse initiation, maximum force, and energy absorption. Therefore, as-built inspection is not only a quality-control step but also a necessary part of mechanical interpretation.

X-ray computed tomography has become one of the most important tools for inspecting additively manufactured lattices because it allows non-destructive three-dimensional evaluation of internal and external geometry [41,56,85,86]. Du Plessis et al. reviewed

microcomputed tomography applications in additive manufacturing and highlighted its usefulness for defect detection, porosity analysis, dimensional verification, and quality control [85]. Thompson et al. reviewed the use of XCT for additive manufacturing and emphasized its role in volumetric dimensional measurement and inspection of internal features [86]. For TPMS and Voronoi structures, XCT is particularly valuable because many critical features are internal and cannot be accessed by simple optical inspection.

XCT has also been used directly in lattice studies to connect as-built geometry with mechanical response. Lei et al. used micro-CT-based finite element analysis to evaluate SLM-fabricated multi-layer lattice structures and showed that real geometry can improve the interpretation of mechanical performance [56]. Qiu et al. discussed different meshing strategies for TPMS structures and highlighted the role of voxel and solid models when wall thickness or relative density increases [37]. Rios et al. showed that geometry details such as strut-joint rounding and multi-cell representation can significantly influence the agreement between simulation and experiment in 316L lattices [54].

XCT-based modelling can improve realism, but it also increases workflow complexity. The image must be reconstructed, segmented, cleaned, converted into a surface or voxel model, meshed, and then simulated. Each step may introduce uncertainty. For this reason, idealized STL-based models remain common when the objective is to compare topologies under controlled assumptions. In such cases, XCT is still useful because it helps explain why experimental results may deviate from numerical predictions [37,54,56,85,86]. This approach is consistent with the present thesis, where XCT is used for the 79% relative-volume group to evaluate as-built quality and to support interpretation of the experimental–numerical comparison. The remaining specimens are interpreted mainly through their compression response.

2.10 Finite Element Modelling of Lattice Compression

Finite element modelling is widely used to study lattice structures because experiments alone cannot fully reveal internal stress distribution, plastic strain localization, contact development, or collapse mechanisms [37,51,54,56,61,75]. FE simulations can also be used to compare topologies under the same boundary conditions and material assumptions. However, the predictive value of a simulation depends strongly on the accuracy of geometry, mesh, material model, boundary conditions, contact assumptions, and damage representation.

Mesh convergence is particularly important for TPMS and stochastic lattice specimens because local curvature, wall thickness, and contact regions can make the predicted reaction force sensitive to element size. For this reason, the numerical workflow of the present thesis includes a mesh convergence study before selecting the final mesh used for validation.

Different modelling strategies have been used for lattices. Beam models are computationally efficient for strut-based structures but may not accurately capture local node geometry, strut overlap, or curved surfaces [74,75]. Shell elements can be suitable for thin-walled TPMS structures, while solid or voxel elements may be required for thicker walls or

complex geometries [37,61]. Smith et al. compared continuum and beam approaches for SLM lattice compression and showed that modelling choice affects predicted stiffness and collapse [75]. Qiu et al. compared shell, solid, and voxel strategies for TPMS structures and found that appropriate element selection depends on relative density and wall thickness [37].

Material modelling is another major issue. Simplified isotropic elastic-plastic models are often used to reduce computational cost, especially for full-specimen simulations. However, LPBF 316L may show anisotropic plasticity, strain hardening, and fracture behavior that depend on build orientation and stress state [33,39,54]. Damage and fracture models can improve local failure prediction, but they require additional calibration data. Therefore, a simplified model may reproduce the general force-displacement trend while failing to capture local cracking, sudden stress drops, or anisotropic collapse.

Boundary conditions and contact can also affect numerical results. In compression tests, friction between plates and specimen may restrict lateral deformation, modify collapse sequence, and change reaction force [37,54,61]. Single-cell models may be useful for efficient property estimation but may not reproduce the boundary and size effects present in full specimens. Rios et al. emphasized that multi-cell configurations and geometry details can be necessary to match experimental curves in 316L lattice simulations [54]. Therefore, finite element models should be treated as tools for interpretation and comparison, not as automatically reliable representations of the real printed structure.

2.11 Synthesis of the State of the Art and Positioning of the Present Work

The reviewed literature shows that LPBF enables the fabrication of complex metallic lattices, but the final mechanical behavior depends on the interaction between process parameters, material response, topology, defects, surface condition, and as-built geometry [3,11,12,17,23,24,30,37,62–67]. Stainless steel 316L is a suitable material for this type of study because it is processable by LPBF and can sustain plastic deformation, but its LPBF microstructure and defect sensitivity require careful interpretation [17–19,33,39,68–71].

The literature on lattice compression confirms that relative density alone is not enough to predict performance. Topology, unit-cell type, wall thickness, strut geometry, grading strategy, and manufacturing quality strongly influence stiffness, strength, plateau behavior, collapse mode, and energy absorption [1–6,20–22,37,42,73–77]. TPMS structures provide smooth periodic surface-based architectures with good potential for mechanical and multifunctional applications [7,22,37,47–50,77–79]. Stochastic Voronoi structures provide a contrasting irregular and biomimetic design approach, but their local stress paths and collapse behavior can be more complex [43–45,80,81]. More broadly, the literature on additively manufactured porous metallic biomaterials confirms that porous architecture, mechanical compatibility, and manufacturability should be evaluated together [82–84].

The literature also shows that XCT and finite element modelling are complementary. XCT provides non-destructive access to internal geometry and defects, while FEM provides insight into stress distribution and deformation mechanisms [37,41,54,56,61,85,86]. However,

numerical models must be validated against experiments because idealized geometries and simplified material laws cannot fully reproduce LPBF defects, surface roughness, anisotropy, or local damage [37,39,54,56,61].

Within this context, the present thesis is positioned as a controlled design–manufacturing–testing–simulation study of LPBF-fabricated 316L lattice structures. Gyroid, Split-P, and stochastic Voronoi specimens are designed in nTop, manufactured using LPBF, separated by WEDM, and experimentally tested under compression. The 79% relative-volume group is further analyzed using XCT and Abaqus simulation to connect internal quality, topology, compressive response, and numerical predictability.

Chapter 3

Materials and Methods

3.1 Specimen Design Plan and Sample Matrix

The experimental and numerical work of this thesis was based on a set of compression specimens designed to compare different lattice architectures under the same material system and manufacturing route. The specimen set included Gyroid, Split-P, and stochastic Voronoi lattice structures, together with one fully dense bulk geometry used as a numerical reference. The lattice specimens were designed with different relative-volume classes in order to evaluate the influence of architecture, material distribution, and relative volume on compressive response.

All compression specimens were designed with the same external dimensions of 30 × 15 × 15 mm^3. The central 20 mm of the specimen height was assigned to the lattice region, while the top and bottom parts were kept as solid end caps with a thickness of 5 mm each. These solid end regions were introduced to improve load transfer during compression and to reduce the direct interaction between the platen surfaces and the porous lattice region. Therefore, the lattice core was located in the central gauge region, while the solid end caps acted as loading interfaces during compression testing.

The specimen set was organized into three relative-volume classes, identified as A, B, and C. Class A specimens had a nominal relative volume of approximately 79%, Class B specimens had a nominal relative volume of approximately 72%, and Class C specimens had a nominal relative volume of approximately 75%. The relative volume was calculated with

respect to the fully dense bulk reference geometry. The bulk geometry had the same external dimensions as the lattice specimens and a volume of 6750 mm³, corresponding to 100% relative volume.

For the Gyroid and Split-P architectures, two cell-mapping strategies were considered: cubic cell mapping and cylindrical cell mapping. The cubic cell map was used to arrange the unit cells in a regular Cartesian distribution inside the lattice region. The cylindrical cell map was used to introduce a different spatial arrangement of the same lattice topology, allowing the influence of cell mapping on the mechanical response to be evaluated. The stochastic Voronoi specimens were designed as irregular cellular networks and were included to provide a non-periodic architecture for comparison with the surface-based Gyroid and Split-P structures.

The detailed design procedure used to generate these geometries in nTop is described in Section 3.2, while the present section defines the specimen set and the role of each geometry in the experimental and numerical program. The final specimen matrix is reported in Table 1. The lattice specimens were fabricated from stainless steel 316L by Laser Powder Bed Fusion and were used for quasi-static compression testing. A selected common relative-volume group was also used for XCT characterization and Abaqus-based numerical validation. The bulk geometry was included only as a numerical dense reference and was not part of the experimental compression-testing program.

Table 1. Compression Specimen Design Matrix.

ID	Lattice type	Architecture / cell map	Thickness / offset range [mm]	Solid volume [mm³]	Relative volume [%]	Compression	XCT	FEM simulation
GY-CYL-A	Gyroid	Cylindrical cell map	1.5–3	5322	79	✓	✓	✓
GY-CYL-B	Gyroid	Cylindrical cell map	1.5–2	4867	72	✓	—	—
GY-CU-A	Gyroid	Cubic cell map	2–3.5	5320	79	✓	✓	✓
GY-CU-B	Gyroid	Cubic cell map	1.8–2.5	4860	72	✓	—	—
SP-CYL-A	Split-P	Cylindrical cell map	0–1	5324	79	✓	✓	✓
SP-CYL-C	Split-P	Cylindrical cell map	0–0.5	5052	75	✓	—	—
SP-CU-A	Split-P	Cubic cell map	0–1.3	5317	79	✓	✓	✓
SP-CU-C	Split-P	Cubic cell map	0–0.7	5040	75	✓	—	—
ST-A	Stochastic Voronoi	Stochastic cellular network	2.5–4	5320	79	✓	✓	✓
ST-B	Stochastic Voronoi	Stochastic cellular network	2–3	4872	72	✓	—	—
ST-C	Stochastic Voronoi	Stochastic cellular network	2.5–3.5	5052	75	✓	—	—
Bulk	Fully dense reference	No lattice structure	—	6750	100	—	—	✓

This matrix was defined to allow two levels of comparison. First, the full lattice set was used to compare the general compression behavior of different architectures and relative-

volume classes. Second, the common relative-volume group was used for a more controlled comparison between topology, internal quality, and numerical response. In this way, the experimental and numerical program was structured to separate the broader effect of relative volume from the more specific effect of lattice architecture.

3.2 nTop-Based Design of Lattice Specimens

The lattice specimens were designed using nTop 5.33.3. The design work focused on generating controlled Gyroid, Split-P, and stochastic Voronoi architectures inside the central gauge region of the compression specimens. Since the general specimen dimensions and the complete sample matrix were already defined in Section 3.1, this section describes the actual digital design procedure used to generate the lattice geometries.

The design process started by defining the compression-specimen envelope and separating the model into two main regions: the central lattice gauge section and the two solid end blocks. The lattice architecture was assigned only to the gauge section, while the upper and lower end blocks were kept fully solid to provide stable contact surfaces during compression. Rounded transition regions were introduced between the lattice core and the solid ends. This step was important because a sharp transition between a porous region and a fully dense region could create local stress concentration and could also make the model less suitable for both manufacturing and simulation.

Three lattice architectures were generated: Gyroid, Split-P, and stochastic Voronoi. For the Gyroid and Split-P specimens, the design was based on the definition of a unit cell followed by the application of a cell map. The unit cell defined the local geometry of the lattice, while the cell map controlled how the unit cells were distributed inside the gauge volume. Therefore, the final lattice geometry was not controlled only by the topology itself, but also by the mapping strategy used to fill the specimen volume.

For the Gyroid and Split-P compression specimens, two cell-mapping strategies were used: cubic and cylindrical. In the cubic cell map, the unit cells were repeated in a regular Cartesian arrangement with dimensions of $7.5 \times 7.5 \times 7.5$ mm³. In the cylindrical cell map, the lattice was generated using a cylindrical distribution defined by a radius of 7.5 mm, a height of 7.5 mm, and 8 angular divisions. This made it possible to design the same topology with two different spatial arrangements, allowing the effect of cell mapping to be considered together with the effect of lattice type. In Figure 20 nTop-based design workflow of the compression specimens could be observed.

The stochastic Voronoi specimens were generated using a different workflow. First, seed points were distributed inside the gauge volume. Based on these seed points, a Voronoi diagram was created, producing an irregular cellular network. After the cellular network was generated, a strut thickness was assigned to convert the Voronoi skeleton into a solid lattice structure. A Trim operation was then applied in nTop to remove the parts of the Voronoi cells that extended outside the intended gauge region. In this way, the final stochastic lattice was kept inside the same external specimen boundary used for the Gyroid and Split-P designs.

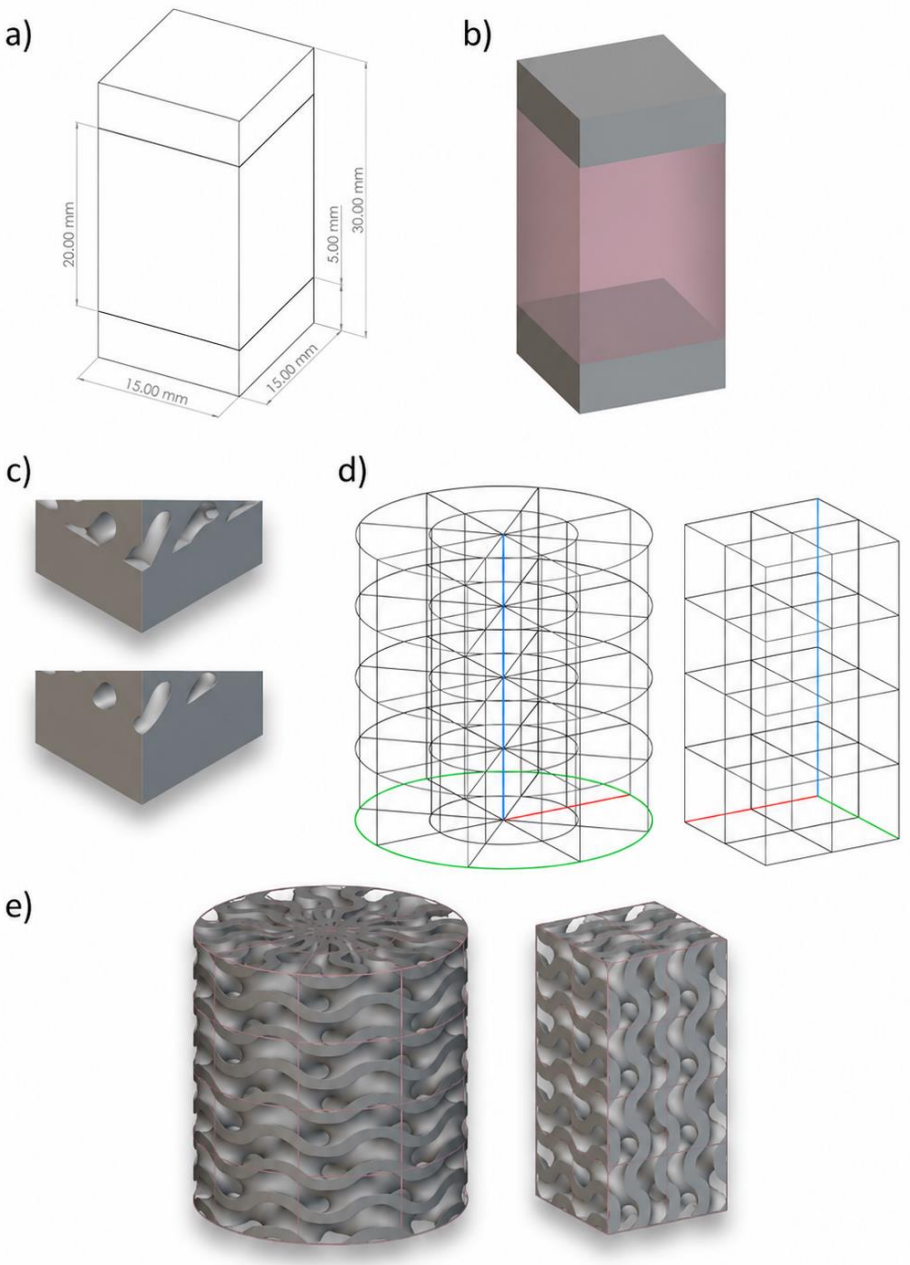

Figure 20. nTop-based Design Workflow of the Compression Specimens: (a) specimen dimensions, (b) separation of solid (grey) and lattice regions (red), (c) transition detail between solid ends and lattice core, (d) and (e) cylindrical and cubic cell-mapping strategies and those representatives.

The wall or strut thickness was controlled through a scalar field along the gauge section. For the graded designs, the minimum thickness was located at the middle of the gauge region, while the thickness increased gradually toward the solid end blocks. This created a smooth thickness variation along the loading direction. The thickness field was therefore used to

control the spatial distribution of material inside the specimen, while avoiding sudden changes between the central lattice region and the end sections.

Two different thickness-control methods were used depending on the lattice type. For the Split-P specimens, the Offset method was used. In this method, the surface thickness was controlled by applying an offset distance from the mid-surface of the TPMS geometry. For the Gyroid and stochastic Voronoi specimens, the Exact Thickness method was used. This method allowed the target wall or strut thickness to be defined directly, with the software adjusting the geometry to match the required thickness more closely. The choice of method was made according to the way each lattice type was generated and controlled inside nTop.

After the topology, cell map, and thickness method were defined, the minimum and maximum thickness or offset values were adjusted to obtain the required solid volume for each specimen. This step was necessary because the comparison between specimens had to be based on controlled relative-volume classes rather than only on visual similarity between geometries. The final thickness or offset ranges, solid volumes, and relative-volume values were those reported in Table 1.

The bulk reference geometry was prepared using the same external dimensions as the lattice specimens, but without applying any lattice structure to the gauge region. It was therefore kept as a fully dense geometry and used as the 100% relative-volume reference for the design matrix.

At the end, the final models were exported as STL files. These STL files were then used for the LPBF manufacturing stage and for the preparation of the finite element models. In this way, the nTop design workflow provided the starting point for both the experimental and numerical parts of the thesis. In Figure 21 the designed samples using nTop software is shown.

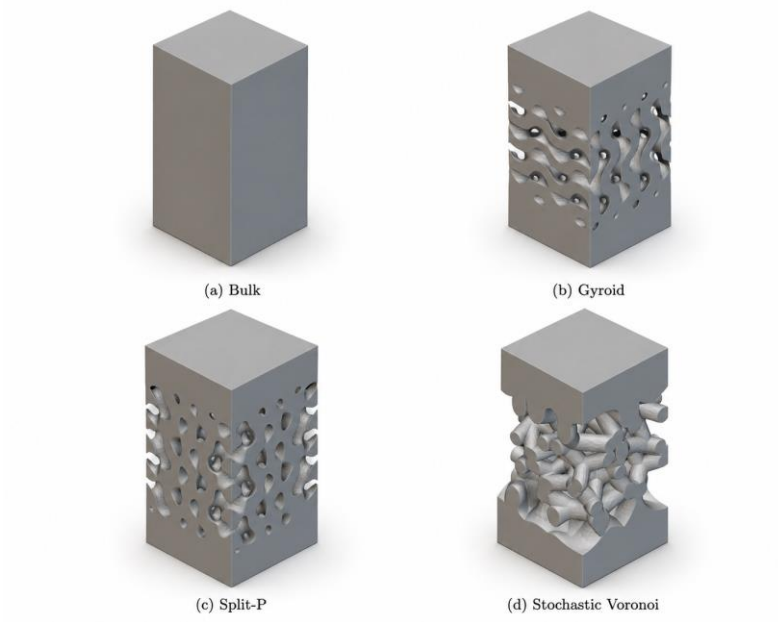

Figure 21. Representative nTop-designed Compression Specimens used in this Study: (a) Bulk, (b) Gyroid, (c) Split-P, and (d) Stochastic Voronoi.

3.3 Stainless Steel 316L Material System

Stainless steel 316L was used as the feedstock material for the fabrication of the lattice specimens. This alloy was selected because of its widespread use in laser powder bed fusion, good corrosion resistance, ductile mechanical response, and suitability for load-bearing lattice structures. In the present work, the material was used in powder form for LPBF fabrication and as the reference material system for the numerical simulations.

The feedstock consisted of LPBF-grade stainless steel 316L powder with a nominal particle size range of 15–45 μm. The powder morphology was examined by scanning electron microscopy (SEM), as shown in Figure 22. The particles were mainly spherical, which is desirable for powder-bed processing because it supports powder spreading and packing during layer deposition. Some slightly irregular particles and satellite particles were also observed. This morphology is commonly found in metal powders used for LPBF and can influence flowability, powder-bed uniformity, and the final surface condition of the printed parts.

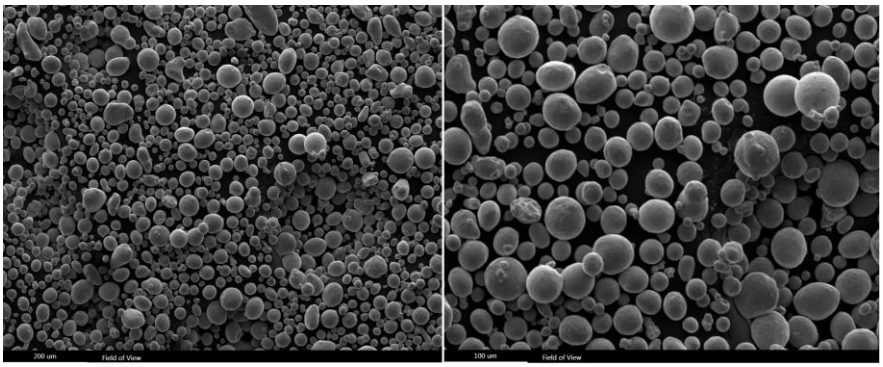

Figure 22. SEM Image of the Stainless Steel 316L Powder Feedstock used for LPBF Fabrication.

The chemical composition of the powder was evaluated by energy-dispersive X-ray spectroscopy (EDS). The EDS analysis was performed at 20 kV and 250× magnification. The measured composition is reported in Table 2. The detected elements confirm the main alloying system of stainless steel 316L, with iron as the balance element and chromium, nickel, molybdenum, and manganese as the principal alloying elements.

Table 2. EDS Chemical Composition of the Stainless Steel 316L Powder.

Element	Mo	Cr	Mn	Fe	Ni
Weight [%]	1.51	17.79	1.12	65.36	14.22
Atomic [%]	0.88	19.10	1.14	65.35	13.53

For the finite element simulations, the mechanical behavior of the printed stainless steel 316L was represented using an elastic–plastic material model. The elastic properties adopted in the numerical model are listed in Table 3. The density and elastic modulus were introduced in Abaqus using the consistent unit system adopted for the simulations (mm).

Table 3. Elastic Material Properties of Printed Stainless Steel 316L used in the FEM Model.

Property	Value
Elastic modulus	143 GPa
Elastic modulus in Abaqus unit system	143000 MPa
Poisson's ratio	0.30
Density	7.98 g/cm^3
Density in Abaqus unit system	7.98×10^{-9} tonne/mm^3

The plastic behavior was defined by a tabulated true stress–plastic strain relationship. This approach allows the nonlinear hardening behavior of the printed material to be included in the compression simulations without assuming a purely elastic or perfectly plastic response. The plastic data used in the model are reported in Table 4. The plastic strain values are shown in percentage form for readability and were converted into dimensionless values when introduced into Abaqus.

Only the elastic and plastic properties required for the numerical compression analysis were introduced in the material model. Fracture-related parameters were not included because the main objective of the simulation was to reproduce the global elastic–plastic response, force–displacement behavior, and deformation trend of the printed lattice specimens. Under compressive loading, these lattice structures are mainly governed by plastic deformation, local bending or buckling, internal contact, and progressive densification. In addition, a reliable fracture model would require separate calibration of damage parameters, which was outside the scope of the present work. This simplification also reduced computational cost and avoided unnecessary numerical instability in the simulation of complex lattice geometries.

Table 4. True Plastic Stress–Plastic Strain Data used for Printed Stainless Steel 316L.

True plastic stress [MPa]	True plastic strain [%]
453	0
476	0.487
489	0.800
504	1.310
522	2.230
538	3.130
578	5.790
625	9.190
681	13.600
781	23.040
802	25.000
855	30.000
908	35.000
961	40.000

3.4 LPBF Manufacturing Procedure

The designed specimens were fabricated by Laser Powder Bed Fusion using a TruPrint 1000 system, which could be found in Figure 23. The manufacturing stage was carried out using stainless steel 316L powder, as described in Section 3.3. The same external specimen geometry and build configuration were used for all lattice designs in order to keep the manufacturing conditions consistent across the different architectures.

Figure 23. TruPrint 1000 [87].

The specimens were arranged on the build platform and fabricated in the vertical direction, with the 30 mm specimen height aligned with the build direction. In this configuration, the solid lower end cap was positioned at the base of the specimen, while the lattice region was built between the lower and upper solid end sections. This orientation was selected to maintain a consistent layer-wise build direction for all samples and to allow comparison between different lattice topologies under the same manufacturing condition.

During the LPBF process, successive powder layers with a thickness of 30 µm were spread over the build platform using a recoating blade. The build chamber was operated under an argon protective atmosphere in order to limit oxidation during laser melting. Each layer was processed using a contour scan followed by a stripe-wise hatch scan of the internal region. A stripe scan strategy with a 67° rotation angle between successive layers was used to reduce directional thermal accumulation and to promote a more balanced distribution of heat during the build. In Figure 24 the printing process and the printed specimens on the build platform are shown.

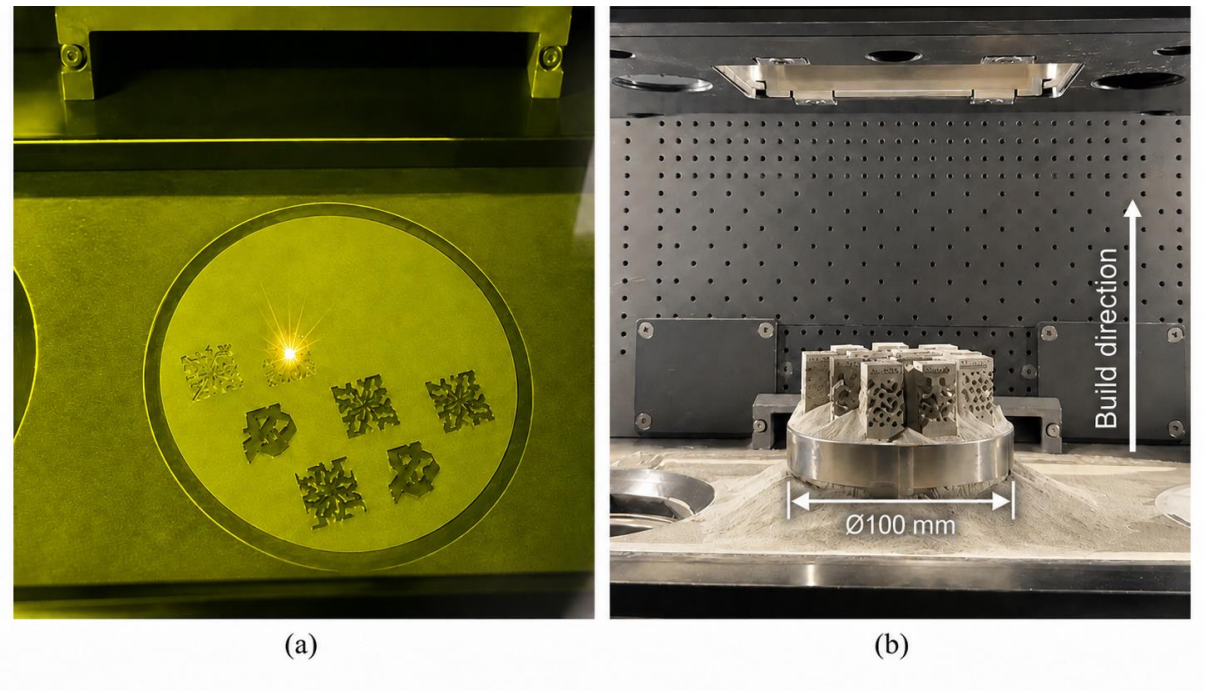

Figure 24. LPBF Fabrication Process: (a) Laser Melting During Printing and (b) As-built Lattice Specimens on the Build Platform.

The main LPBF process parameters used in this work are summarized in Table 5. The laser power was set to 200 W, the scan speed to 1000 mm/s, the hatch spacing to 0.10 mm, and the layer thickness to 0.03 mm. Based on these values, the line energy and volumetric energy density were calculated as 0.20 J/mm and 66.7 J/mm³, respectively.

Table 5. LPBF Process Parameters used for Manufacturing the Stainless Steel 316L Specimens.

Parameter	Value
LPBF system	TruPrint 1000
Material	Stainless steel 316L
Protective atmosphere	Argon
Shielding gas speed	1.5 m/s
Layer thickness	30 µm
Laser beam diameter	80 µm
Laser power	200 W
Scan speed	1000 mm/s
Hatch spacing	0.10 mm
Hatch pattern	Stripe scan strategy
Layer rotation angle	67°
Stripe width	6 mm
Stripe overlap	0.10 mm
Line energy	0.20 J/mm
Volumetric energy density	66.7 J/mm³

The volumetric energy density and line energy were calculated using Equations (2) and (3):

$$\mathrm{VED} = \frac{P}{v \cdot h \cdot t} \tag{2}$$

$$\mathrm{E_{Line}} = \frac{P}{v} \tag{3}$$

Where *VED* is the volumetric energy density ($\frac{J}{mm^3}$), P is the laser power ($\frac{J}{S}$), v is the scan speed ($\frac{mm}{s}$), h is the hatch spacing (mm), and t is the layer thickness (mm), and E_{Line} is the line energy ($\frac{J}{mm}$).

These values were used as compact indicators of the energy input applied during manufacturing. However, they were considered only as engineering indicators, since the final quality of LPBF parts also depends on other factors such as scan strategy, powder spreading, local heat accumulation, melt-pool stability, and lattice geometry.

A photograph of the printed build platform is presented in Figure 25. This figure shows the as-built arrangement of the stainless steel 316L specimens before complete separation and further characterization. It is remarkable to say, the printing process for all the 12 specimens has repeated 2 times to make sure that the compression tests will have reliable results.

Figure 25. Printed Build Platform Containing the Stainless Steel 316L Compression Specimens Fabricated by LPBF.

3.5 Specimen Removal from the Build Platform by WEDM

After completion of the LPBF process, the printed specimens remained attached to the circular build platform. Before XCT characterization and compression testing, the specimens had to be separated from the platform without damaging the lattice regions. For this purpose, Wire Electrical Discharge Machining (WEDM) was used.

The cutting operation was carried out using a Bomatec BMW 3000 WEDM machine. WEDM was selected because stainless steel 316L is electrically conductive and can therefore be machined by controlled electrical discharges. In this process, a continuously fed wire electrode removes material through localized spark erosion, while dielectric fluid cools the cutting zone and flushes away the eroded particles. Since the wire does not apply conventional mechanical cutting forces to the part, WEDM is especially suitable for delicate lattice specimens, where thin walls and internal features could be damaged by sawing, milling, or manual separation.

During specimen removal, the build platform was fixed on the WEDM machine and the cutting path was positioned close to the interface between the specimens and the platform. The cut was performed through the solid base region, away from the central lattice gauge section. This approach allowed the samples to be detached while preserving the lattice architecture and avoiding direct mechanical loading of the porous region. The main WEDM parameters used for the removal process are summarized in Table 6.

Table 6. WEDM Parameters Used for Specimen Removal.

Parameter	Value
WEDM machine	Bomatec BMW 3000
Cutting method	Wire electrical discharge machining
Workpiece material	LPBF stainless steel 316L
Current	2 A
V-F wire-feed setting	30
Dielectric medium	Deionized water-based dielectric fluid
Cutting region	Solid base/end-cap region

During cutting, a small safety distance from the build platform was maintained by the wire to prevent undesired arcing and protect the reusable platform. After separation, the specimens were prepared for XCT characterization and quasi-static compression testing. This separation process is shown in Figure 26.

Figure 26. Separation of LPBF-fabricated Stainless Steel 316L Lattice Specimens from the Build Platform Using WEDM.

Figure 27 shows the stainless steel 316L specimens after separation from the build platform. The different lattice architectures remained visually intact after WEDM removal, confirming that the cutting operation did not directly damage the central lattice regions.

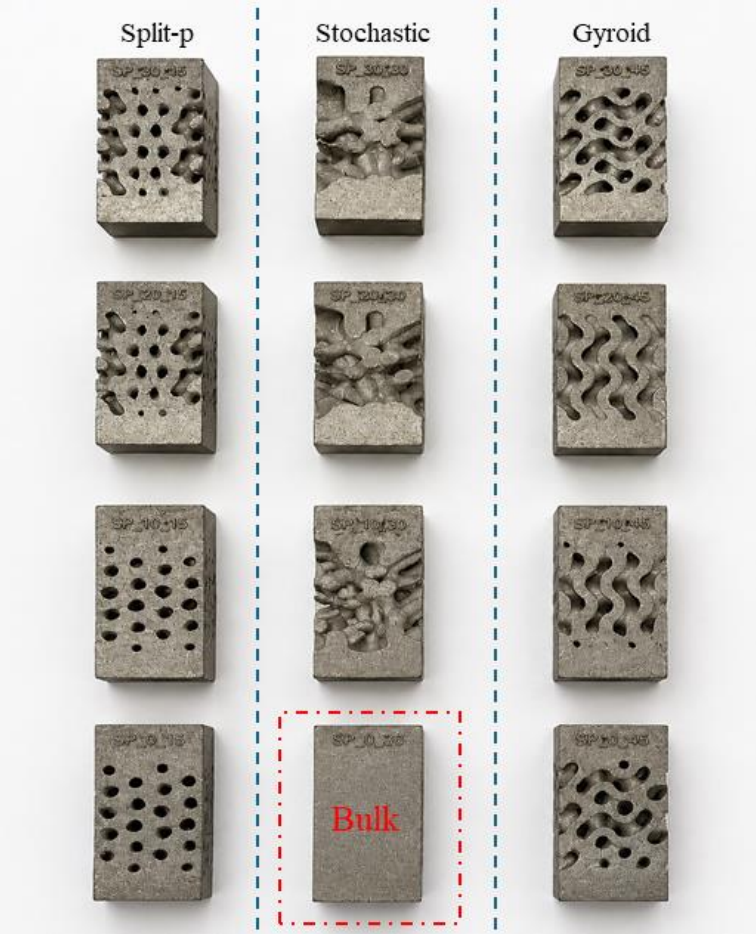

Figure 27. LPBF-fabricated Stainless Steel 316L Specimens after WEDM Separation from the Build Platform.

3.6 X-ray Computed Tomography Characterization

XCT was used as a non-destructive method to inspect the selected stainless steel 316L lattice specimens after LPBF fabrication and WEDM separation. The analysis was performed on the common 79% relative-volume group, including GY-CYL-A, GY-CU-A, SP-CYL-A, SP-CU-A, and ST-A. This selection allowed the different lattice architectures to be compared under the same nominal relative-volume condition.

The scans were carried out using a Phoenix v|tome|x S XCT system in cone-beam mode. During scanning, each specimen was rotated through 360°, while radiographic projections were collected using a DXR-250 RT flat-panel detector. The main acquisition settings included an X-ray voltage of 180 kV, a current of 60 µA, a 0.5 mm copper filter, an exposure time of 333.107 ms per projection, and a focal spot size of 10.8 µm. The focal spot size was considered as a resolution-related scan parameter and was not treated as the direct measurement precision of the XCT analysis.

The reconstructed XCT volumes were processed using Dragonfly 2024.1 software. Two analysis workflows were carried out. First, the reconstructed as-built geometry was registered

with the original STL model to perform a nominal/actual comparison and visualize local geometrical deviations through color maps. The deviation scale used for this comparison was ±0.08 mm. Second, porosity and inclusion analysis was performed to detect internal defects and classify pores according to their size, position, and distribution. In this workflow, only features above the software-defined threshold of 90 voxels were considered. In Figure 28 both the machine and the software are shown.

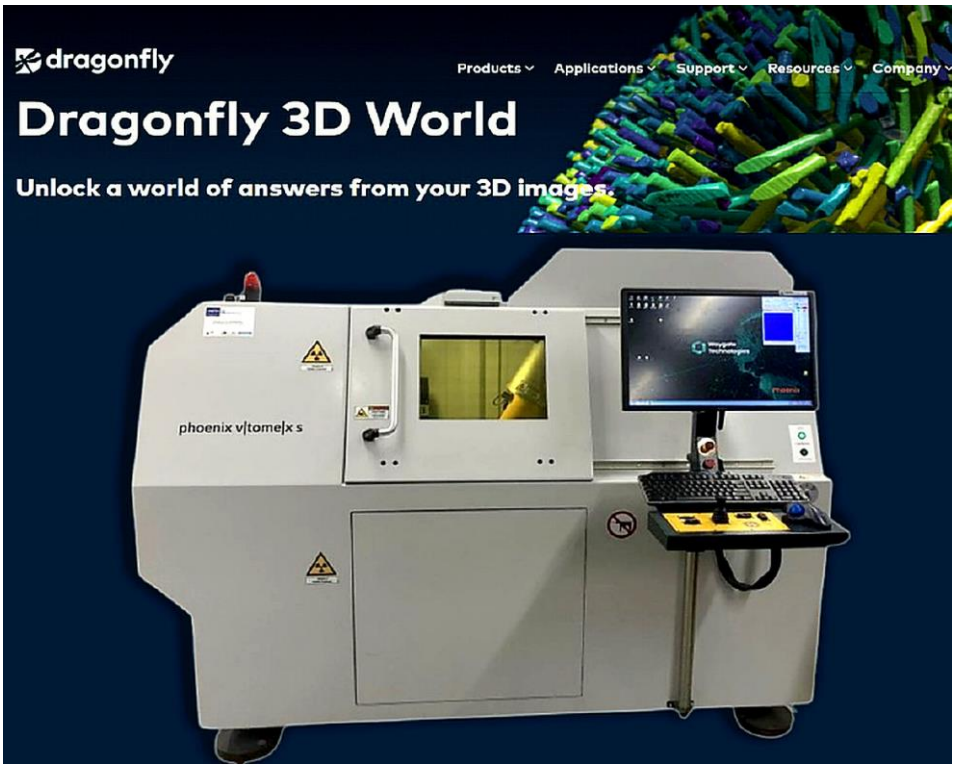

Figure 28. The Dragonfly Software Used to Analyze the XCT Data and the Phoenix v\|tome\|x S XCT System Used to Acquire the Data [88].

3.7 Quasi-Static Compression Testing

Quasi-static compression tests were carried out to evaluate the mechanical response of the LPBF-fabricated stainless steel 316L lattice specimens. The tests were performed using an Easydur 3Mz universal testing machine as shown in Figure 29, following the general procedure for compression testing of porous and cellular metallic materials according to ISO 13314. The aim of this stage was to obtain the force–displacement response of each lattice architecture and to derive the corresponding engineering stress–strain curves for comparison between the different designs.

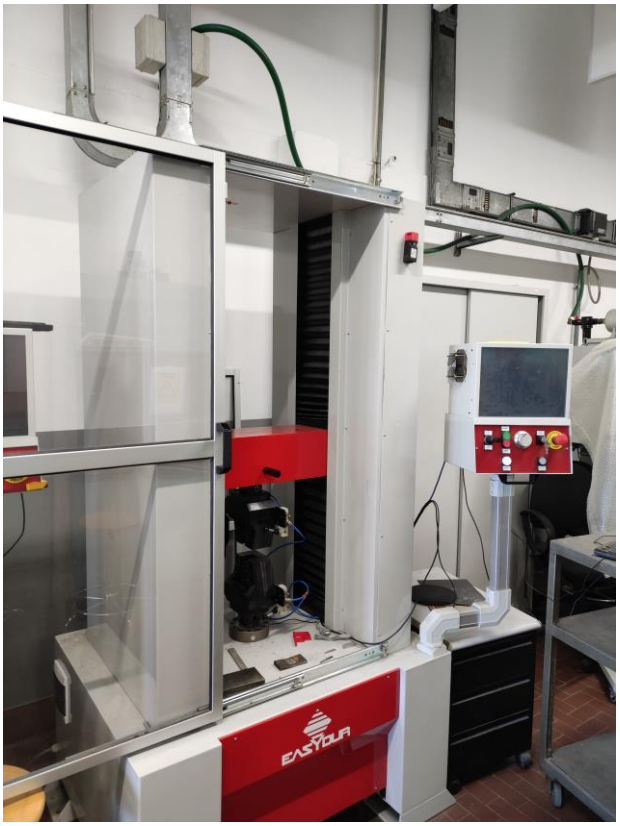

Figure 29. Easydur 3Mz Universal Testing Machine.

The compression tests were performed on all lattice specimens, while the fully dense bulk specimen was not included in the experimental compression test due to the load-capacity limitation of the testing system. The bulk geometry was therefore considered only in the numerical part of the thesis as a fully dense reference model.

Each specimen was positioned between two flat compression platens and loaded along its vertical direction. Therefore, the loading direction was parallel to the 30 mm specimen height and to the build direction. A thin film of lubricating grease was applied to the contact surfaces between the specimen and the compression platens to reduce friction, and promote a more uniform load distribution during compression. Before the main loading stage, a preload of 1000 N was applied to ensure proper contact between the specimen and the platens and to reduce the effect of initial seating or misalignment.

The compression test was conducted under displacement control at a crosshead speed of 1 mm/min up to almost 7.5 mm which was quite the threshold regarding the capacity of machine for imposing compressive force (100KN). During testing, the applied force and crosshead displacement were continuously recorded by the testing system and we did the test for 2 complete sets of lattices, to make sure that the results are reliable enough. The main testing parameters are summarized in Table 7.

Table 7. Parameters Used for Quasi-Static Compression Testing.

Parameter	Value / description
Testing method	Quasi-static uniaxial compression
Testing machine	Easydur 3Mz universal testing machine
Reference standard	ISO 13314
Tested samples	Lattice specimens only
Bulk specimen	Not experimentally tested
Loading direction	Vertical, along specimen height
Control mode	Displacement control
Crosshead speed	1 mm/min
Preload	1000 N
Maximum displacement	7.5 mm
Lubrication	Thin film of lubricating grease at platen–specimen contact surfaces
Initial cross-sectional area	15 × 15 mm^2
Initial height for strain calculation	30 mm

The engineering compressive stress was calculated by dividing the measured force by the initial projected cross-sectional area of the specimen, equal to 225 mm^2. The engineering compressive strain was calculated by dividing the crosshead displacement by the initial specimen height of 30 mm. This approach provided engineering stress–strain curves suitable for comparing the global compressive response of the different lattice architectures.

From the force–displacement and engineering stress–strain curves, the main mechanical indicators were extracted, including the initial effective stiffness, compressive strength, plateau-like response, and absorbed energy. The absorbed energy was calculated from the area under the force–displacement curve over the selected deformation range. These parameters were later used to compare the performance of the Gyroid, Split-P, and stochastic Voronoi specimens.

The compression testing procedure was repeated as part of the experimental campaign in order to assess the repeatability of the measured response.

Representative photographs of the compression tests are shown in Figure 30 for the three lattice architectures investigated in this work. The images illustrate the positioning of the specimens between the upper and lower compression platens and confirm that the load was applied along the vertical specimen direction.

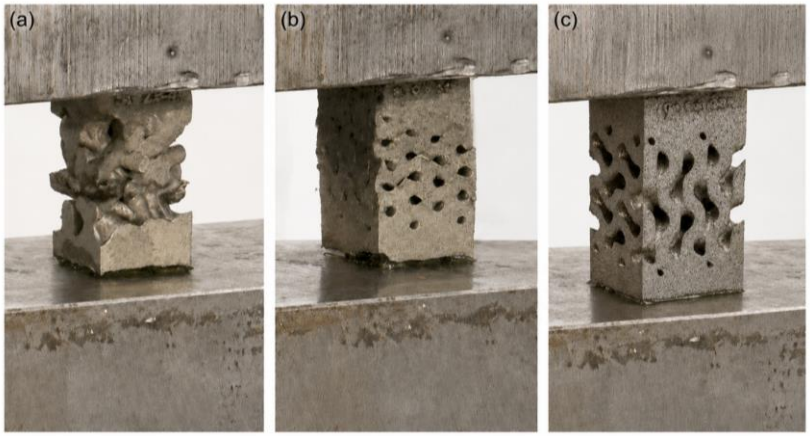

Figure 30. Representative Quasi-Static Compression Tests of the LPBF-Fabricated Stainless Steel 316L Lattice specimens: (a) Stochastic Voronoi, (b) Split-P, and (c) Gyroid Lattice Architecture.

3.8 Finite Element Simulation

Finite element simulations were carried out to reproduce the compression response of the selected stainless steel 316L lattice specimens and to support the comparison between experimental and numerical results. The numerical analysis was performed for the common 79% relative-volume lattice group and for the fully dense bulk reference geometry. Abaqus 2023 was used for the simulation stage, while nTop 5.33.3 was used for preparing the finite element volume meshes of the lattice specimens.

The meshing stage was performed in nTop because of the complex internal surfaces and fine geometrical details of the lattice architectures. Direct meshing of such geometries in Abaqus can be difficult due to the curved TPMS surfaces, internal channels, small local features, and gradual wall-thickness variations. Therefore, the designed lattice models were first converted into finite element volume meshes in nTop and then exported as Abaqus input files for the numerical simulation.

Quadratic tetrahedral elements were selected instead of linear tetrahedral elements because the lattice specimens contained highly curved surfaces and complex internal geometries. Linear tetrahedral elements represent element edges with straight lines and are therefore less suitable for accurately capturing curved lattice walls unless a very fine mesh is used. In contrast, quadratic tetrahedral elements include mid-side nodes, allowing the element edges and faces to follow curved geometries more accurately. This was particularly important for the TPMS and stochastic Voronoi lattices, where the mechanical response is strongly affected by local curvature, wall thickness variation, and bending-dominated deformation. Therefore, the use of quadratic elements improved the geometrical representation of the lattice surfaces and reduced the risk of artificial stiffness caused by an overly simplified linear discretization.

After importing the mesh into Abaqus, the original C3D10 element type was changed to C3D10M. The C3D10M element is the modified version of the 10-node quadratic tetrahedral

element and is more suitable for nonlinear explicit simulations involving large deformation and contact. This choice was important because the compression of lattice structures involves progressive collapse, interaction between the specimen and the compression plates, and possible contact between different regions of the lattice during deformation. Compared with the standard C3D10 formulation, the modified C3D10M element provides more robust numerical behavior for contact-dominated explicit simulations and reduces the risk of numerical difficulties during large deformation.

A mesh convergence study was performed before selecting the final mesh parameters. The objective was to obtain a mesh fine enough to represent the curved lattice walls and local deformation zones, while avoiding excessive computational cost. The final mesh parameters were therefore selected as an optimum compromise between numerical accuracy and computational efficiency. The suitability of the mesh was evaluated mainly based on the stability of the global force–displacement response, since the main objective of the simulation was to compare the global compression behavior rather than to predict local fracture initiation. The final nTop mesh settings used for the lattice specimens are summarized in Table 8.

Table 8. The Final nTop Mesh Settings.

Parameter / value	Purpose
Mesh type: FE volume mesh	Generation of simulation-ready volume elements
Unit system: mm	Consistent geometry scale for Abaqus import
Tolerance: 0.25 mm	Controls the allowed deviation during surface remeshing
Minimum feature size: 0.30 mm	Preserves small lattice openings and local wall features
Sharpen iterations: 2	Improves preservation of relevant edges and transitions
Surface edge length: 0.75 mm	Controls the characteristic size of surface triangles
Surface element shape: Triangle	Defines the surface discretization before volume meshing
Span angle: 10°	Improves discretization of curved TPMS and Voronoi regions
Growth rate: 1.15	Controls smooth transition between small and large surface elements
Feature angle: 40°	Helps preserve important geometrical transitions
Minimum edge length: 0.15 mm	Allows local refinement near small openings and curved details
Volume edge length: 1.0 mm	Controls the characteristic size of the internal volume mesh
Volume growth rate: 1.15	Reduces abrupt element-size transitions inside the volume mesh
Geometric order: Quadratic	Enables the use of second-order tetrahedral elements

The mesh parameters were selected to capture the main geometrical features of the lattice structures while maintaining a reasonable computational cost. The surface edge length, span angle, and minimum edge length controlled the quality of the surface representation, especially in curved regions. The minimum feature size was used to avoid the loss of relevant

small openings and local wall features. The growth rate controlled the transition between refined and coarser regions, reducing sudden mesh-size changes. Finally, the quadratic geometric order improved the representation of curved lattice surfaces, while the modified C3D10M formulation provided better robustness for the explicit contact analysis of the deforming lattice specimens.

The finite element simulations were performed using the Abaqus/Explicit solver. This solver was selected because the compression of lattice structures involves large deformation, complex contact between lattice walls and compression plates, and possible self-contact during collapse. These conditions can create severe convergence difficulties in an implicit standard analysis. Therefore, the dynamic explicit procedure was used as a robust numerical approach for simulating the full compression process.

The compression setup was modeled using two rigid plates and one deformable specimen. The lower compression plate was modeled as a discrete rigid plane with dimensions of 20 × 20 mm² and a linear mesh size of 2 mm. This plate was fully fixed using an encastre boundary condition. The upper compression plate had the same dimensions and rigid-body definition, but a vertical displacement of −18 mm was imposed in the z-direction. The displacement was applied using a tabular amplitude, defined as 0 at time 0 and 1 at the final simulation time of 0.018. In this way, the prescribed displacement increased progressively during the analysis.

The selection of 18 mm for the displacement and 0.018 s for the time period of the solver, will result the compression speed set to almost 1 meter per second. The selection of 18 mm was for the reason that it is 60 % percent of our specimen's height which is appropriate for determining the elastic, plateau, and the densification regions, but as we have limitation with the compression machine, the results till 7.5 mm are considered, which is still completely appropriate to determine the elastic and plateau region and the mechanical behavior of our lattices which are our aim of this study.

The explicit analysis time was set to 0.018. This time period was used as a numerical time suitable for the explicit simulation and was not treated as the real experimental loading time. To verify that the simulation remained close to quasi-static conditions, the kinetic energy was monitored during the analysis and compared with the internal energy. In the performed simulations, the kinetic energy remained almost below 5% of the internal energy, confirming that inertial effects were limited and that the numerical response could be considered acceptable for quasi-static comparison.

General contact was defined in the Abaqus Interaction module. The normal contact behavior was modeled using hard contact, while the tangential behavior was defined using a penalty friction formulation with a friction coefficient of 0.3. This contact definition was used to describe the interaction between the specimen and the compression plates, as well as the contact that could occur between different regions of the deforming lattice during compression.

The stainless steel 316L material model defined in Section 3.3 was assigned to the lattice and bulk specimens. The compression plates were modeled as rigid bodies because their deformation was negligible compared with that of the lattice specimens. The simulations were performed using a consistent N–mm–MPa unit system. The main finite element simulation settings are summarized in Table 9.

Table 9. The Main Finite Element Simulation Settings.

Parameter	Value / description
Simulation software	Abaqus 2023
Solver	Dynamic Explicit
Meshing software	nTop 5.33.3
Imported mesh format	Abaqus input file (.inp)
Lattice mesh element type	C3D10M modified quadratic tetrahedral element
Plate type	Discrete rigid planes
Plate mesh type	Linear mesh
Plate dimensions	20 × 20 mm²
Plate mesh size	2 mm
Lower plate boundary condition	Encastre
Upper plate boundary condition	Vertical displacement of −18 mm
Analysis time period	0.018
Amplitude definition	Tabular amplitude: 0 at time 0, 1 at time 0.018
Contact formulation	General contact
Normal behavior	Hard contact
Tangential behavior	Penalty friction formulation
Friction coefficient	0.3
Simulated specimens	79% relative-volume lattice specimens and bulk reference

After completion of the simulations, the reaction force and displacement data were extracted from the compression setup to obtain numerical force–displacement curves. These curves were then converted into engineering stress–strain curves using the same reference area and height used for the experimental compression data. The initial cross-sectional area was taken as 15 × 15 mm², while the initial height was taken as 30 mm. This allowed a direct comparison between the experimental and numerical responses of the lattice specimens.

In Figure 31, the meshed lattice specimen in nTop software and also the assembly of it in Abaqus software is shown.

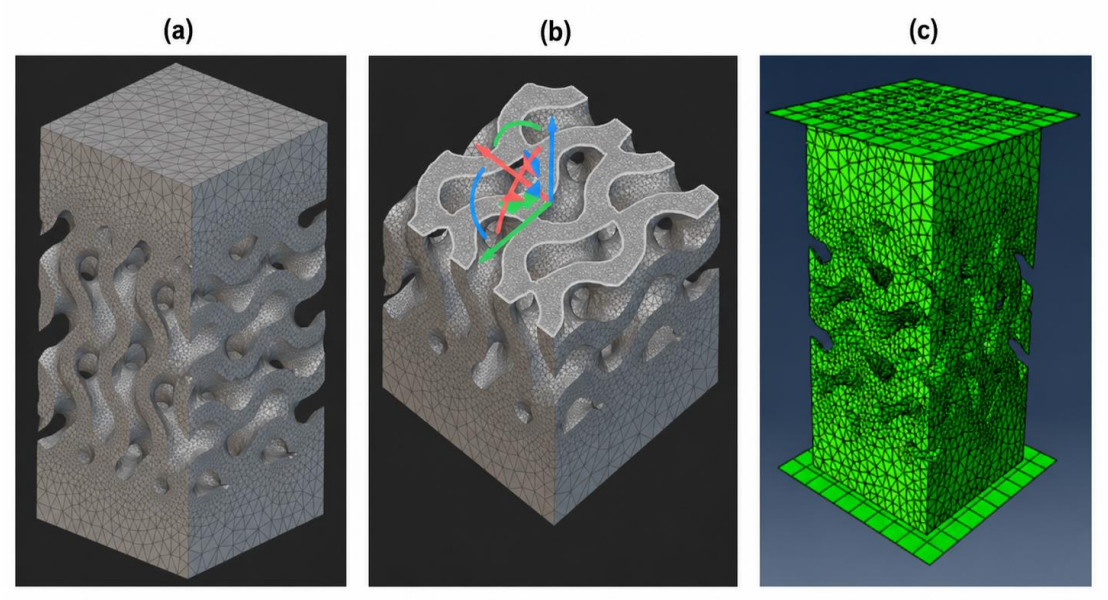

Figure 31. Finite Element Preparation Workflow: (a) Complete nTop-generated Lattice Volume Mesh, (b) Cross-Sectional View of the nTop Mesh Showing the Internal Lattice Discretization, and (c) Abaqus Assembly of the Meshed Specimen Between Rigid Compression Plates.

Chapter 4

Results and Discussion

4.1 Overview of the Results

This chapter presents and discusses the experimental and numerical results obtained from the compression testing, energy absorption analysis, XCT-based characterization, and Abaqus simulations of the lattice samples. The main purpose of this chapter is not only to report the mechanical values, but also to understand how the different geometries respond under compression and how their performance is influenced by relative volume, topology, and manufacturing quality.

The results are first organized based on the experimental compression tests performed on the eleven lattice samples. For each design, two repeated tests were carried out, and the average values were used as the main basis for comparison. The evaluated mechanical properties include the elastic modulus, ultimate compressive strength (UCS), absorbed energy up to the UCS point, and absorbed energy up to a strain of 0.20. These parameters were selected because they describe both the initial load-bearing capacity of the structures and their ability to continue absorbing energy after the first major collapse event.

The discussion then compares the behavior of the different topology families, including Gyroid, Split-P, and stochastic structures. Particular attention is given to the influence of the cubic and cylindrical configurations, since this geometrical difference produced clear changes in stiffness, strength, and absorbed energy. After the experimental comparison, the XCT and as-built geometry results are used to support the interpretation of the mechanical response,

especially for the 79% relative-volume samples. These data help to explain the role of manufacturing deviations, surface irregularities, and internal porosity in the final behavior of the printed structures.

Finally, the Abaqus simulation results are compared with the experimental averages for the 79% relative-volume samples. This comparison is used to evaluate the accuracy of the numerical models and to identify the possible reasons for differences between simulation and experiment. In this way, the chapter connects the experimental observations, the as-built quality of the samples, and the numerical predictions into a single interpretation of the mechanical performance of the investigated lattice structures.

4.2 Experimental Compression Results

The compression results were first collected and organized for all eleven lattice samples in order to compare their mechanical response in a consistent way. For each design, two compression tests were carried out under the same testing condition. The values obtained from the two repetitions were reported separately, and then the average value was calculated. In the following sections, the average values are used as the main reference for comparison, since they provide a more reliable representation of the behavior of each geometry than a single test result. Table 10 summarizes the elastic modulus and UCS values obtained from the compression tests.

Table 10. Elastic Modulus (E) and UCS Values Obtained from the Compression Tests.

Sample	Rel. volume	E_1 (GPa)	E_2 (GPa)	E avg. (GPa)	UCS_1 (MPa)	UCS_2 (MPa)	UCS avg. (MPa)
GY-CU-A	79%	6.16	5.86	**6.01**	210.84	211.56	**211.20**
GY-CU-B	72%	4.60	5.04	**4.82**	152.96	145.88	**149.42**
GY-CYL-A	79%	6.56	6.08	**6.32**	237.00	235.88	**236.44**
GY-CYL-B	72%	5.58	5.00	**5.29**	185.74	190.60	**188.17**
SP-CU-A	79%	6.48	5.83	**6.16**	195.29	192.60	**193.94**
SP-CU-C	75%	5.29	5.81	**5.55**	178.32	176.88	**177.60**
SP-CYL-A	79%	6.38	6.53	**6.46**	221.14	212.49	**216.81**
SP-CYL-C	75%	5.50	6.04	**5.77**	181.10	197.23	**189.16**
ST-A	79%	5.78	4.90	**5.34**	157.21	154.97	**156.09**
ST-B	72%	4.19	3.81	**4.00**	102.31	88.31	**95.31**
ST-C	75%	5.37	5.06	**5.21**	134.92	127.35	**131.13**

A clear difference can be observed between the tested geometries. The highest average elastic modulus was measured for the SP-CYL-A sample, with a value of 6.46 GPa, showing that this configuration had the stiffest initial response. On the other hand, the highest average UCS was obtained for the GY-CYL-A sample, reaching 236.44 MPa. This means that the

stiffest sample was not necessarily the one with the highest compressive strength. This point is important because the elastic stiffness mainly describes the early response of the structure, while the UCS is more related to the load-bearing limit before the main collapse stage.

The weakest response was observed for the ST-B sample. This structure showed the lowest average elastic modulus, 4.00 GPa, and the lowest average UCS, 95.31 MPa. Compared with the TPMS-based samples, the stochastic structure showed a less efficient mechanical response, especially at the lower relative volume of 72%. This behavior suggests that the irregularity of the stochastic architecture may lead to less uniform load transfer and earlier local collapse. In Figure 32 and Figure 33 these comparisons are visually presented.

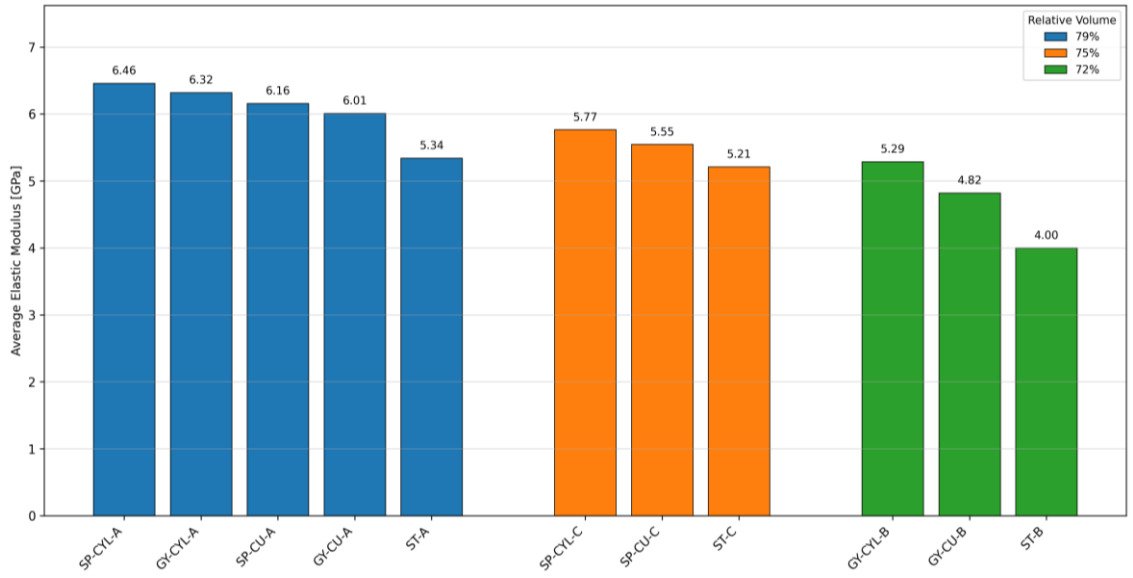

Figure 32. Average Elastic Modulus.

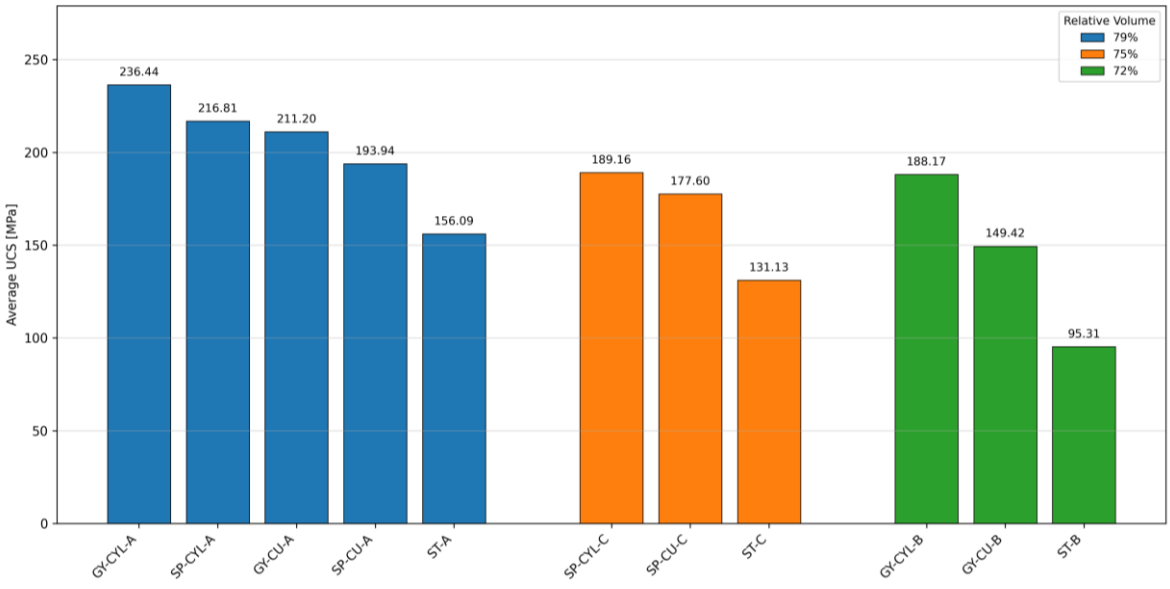

Figure 33. Average UCS.

In general, the samples with higher relative volume showed better mechanical properties. However, the results also show that relative volume alone cannot fully explain the compression behavior. For example, samples with the same relative volume of 79% did not show the same stiffness, UCS, or energy absorption. Therefore, the topology and geometrical configuration must also be considered when interpreting the results.

The absorbed energy was calculated from the area under the force–displacement curve and then divided by each sample volume. Therefore, the results are reported as absorbed energy density in MJ/m³. Two values were considered for each test: absorbed energy up to the UCS point and absorbed energy up to a strain of 0.20. The first value represents the amount of energy absorbed before reaching the main compressive strength limit. The second value gives a broader view of the energy absorption capacity during further deformation, including the post-UCS collapse and densification stages. Table 11 summarizes the energy absorption of samples.

Table 11. Energy Absorption of Samples.

Sample	EA_1 at UCS (MJ/m³)	EA_2 at UCS (MJ/m³)	EA avg. at UCS (MJ/m³)	EA_1 at 0.20 strain (MJ/m³)	EA_2 at 0.20 strain (MJ/m³)	EA avg. at 0.20 strain (MJ/m³)
GY-CU-A	6.30	7.43	**6.87**	32.42	33.16	**32.79**
GY-CU-B	5.17	3.95	**4.56**	19.17	19.66	**19.41**
GY-CYL-A	9.18	8.33	**8.75**	42.82	43.39	**43.11**
GY-CYL-B	6.18	7.30	**6.74**	29.40	29.81	**29.60**
SP-CU-A	4.58	5.17	**4.88**	34.87	34.11	**34.49**
SP-CU-C	4.77	4.38	**4.57**	27.71	28.16	**27.94**
SP-CYL-A	6.54	5.10	**5.82**	38.20	38.30	**38.25**
SP-CYL-C	4.49	5.26	**4.88**	27.68	28.52	**28.10**
ST-A	2.46	2.61	**2.54**	29.78	29.48	**29.63**
ST-B	1.82	1.50	**1.66**	14.87	15.77	**15.32**
ST-C	2.01	1.79	**1.90**	20.51	18.88	**19.70**

As reported in Table 11, the GY-CYL-A sample showed the highest energy absorption performance. Its average absorbed energy at UCS was 8.75 MJ/m³, and its average absorbed energy at 0.20 strain reached 43.11 MJ/m³. This confirms that GY-CYL-A was not only the strongest sample in terms of UCS, but also the most effective structure for absorbing energy over the selected strain range.

The SP-CYL-A sample also showed a high energy absorption capacity, with an average value of 38.25 MJ/m³ at 0.20 strain. Although this value is lower than that of GY-CYL-A, it is still one of the highest results among the tested samples. This shows that the Split-P cylindrical configuration was mechanically efficient, particularly in stiffness, but the Gyroid cylindrical configuration provided a better combination of strength and energy absorption. These comparisons between the energy absorption of the samples are visually presented in Figure 34.

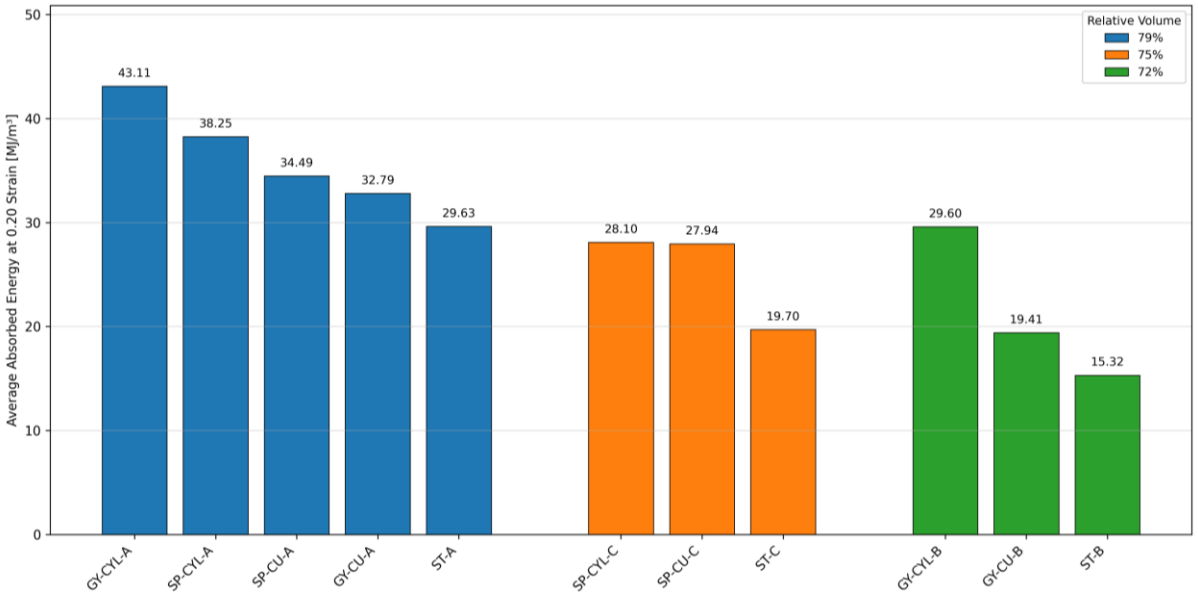

Figure 34. Average Absorbed Energy at 0.20 Strain.

A comparison between cubic and cylindrical configurations shows that the cylindrical samples generally performed better. This trend is particularly clear for the Gyroid structures, where GY-CYL-A had higher stiffness, UCS, and absorbed energy than GY-CU-A. The same tendency was also observed for the Split-P samples, although the difference was slightly less pronounced. This indicates that the cylindrical configuration improved the load transfer and helped the structure maintain better mechanical performance during compression.

Overall, the experimental results show that the mechanical behavior of the lattice structures depends on the combined effect of relative volume, topology, and geometrical configuration. Higher relative volume generally improved the response, but the best performance was achieved when the topology and geometry also provided stable load transfer. Based on the average values, GY-CYL-A can be identified as the best-performing sample in terms of UCS and absorbed energy, while SP-CYL-A showed the highest elastic modulus. These average values are used in the next sections for the detailed comparison of topology, geometry, XCT-based quality, and Abaqus validation.

4.3 Effect of Topology and Geometrical Configuration

The nominal geometries and design workflow of the investigated samples were already presented in Chapter 3. Therefore, the present section focuses on the experimental compression response of each topology family and compares the effect of geometrical configuration and relative volume on the measured mechanical behavior. The comparison is mainly based on the average values of elastic modulus, UCS, and absorbed energy reported in Tables 10 and 11, together with the compression curves shown in Figures 35–39.

Although relative volume has a clear influence on the mechanical response, the results show that it is not the only controlling factor. Samples with the same relative volume did not always show the same stiffness, UCS, or energy absorption capacity. This indicates that topology and external configuration also affected the load-transfer mechanism, collapse behavior, and post-UCS response of the structures.

4.3.1 Gyroid samples

The Gyroid group included four samples: GY-CU-A, GY-CU-B, GY-CYL-A, and GY-CYL-B.

Among the Gyroid samples, GY-CYL-A showed the best overall mechanical response. This sample had an average elastic modulus of 6.32 GPa and the highest UCS among all tested samples, equal to 236.44 MPa. It also showed the highest absorbed energy at 0.20 strain, with an average value of 43.11 MJ/m³. The stress level of GY-CYL-A remained relatively high after the first peak, which helped the sample absorb a larger amount of energy during further compression.

The comparison between GY-CU-A and GY-CYL-A is especially important because both samples had the same relative volume of 79%. However, GY-CYL-A performed better in all main mechanical indicators. The average UCS increased from 211.20 MPa for GY-CU-A to 236.44 MPa for GY-CYL-A, while the absorbed energy at 0.20 strain increased from 32.79 MJ/m³ to 43.11 MJ/m³. This suggests that the cylindrical configuration improved the mechanical efficiency of the Gyroid topology, especially in terms of strength and energy absorption.

A similar trend was observed at the lower relative volume. GY-CYL-B showed higher stiffness, UCS, and absorbed energy than GY-CU-B. The average UCS increased from 149.42 MPa in GY-CU-B to 188.17 MPa in GY-CYL-B, and the absorbed energy at 0.20 strain increased from 19.41 MJ/m³ to 29.60 MJ/m³. Therefore, the cylindrical configuration improved the Gyroid response not only at 79% relative volume, but also at 72%.

Overall, the Gyroid samples showed a stable and efficient compression behavior. The cylindrical Gyroid samples were clearly stronger than the cubic ones, indicating that this configuration provided a more effective load-transfer path under compression. All these comparisons are shown visually in Figure 35 and Figure 36.

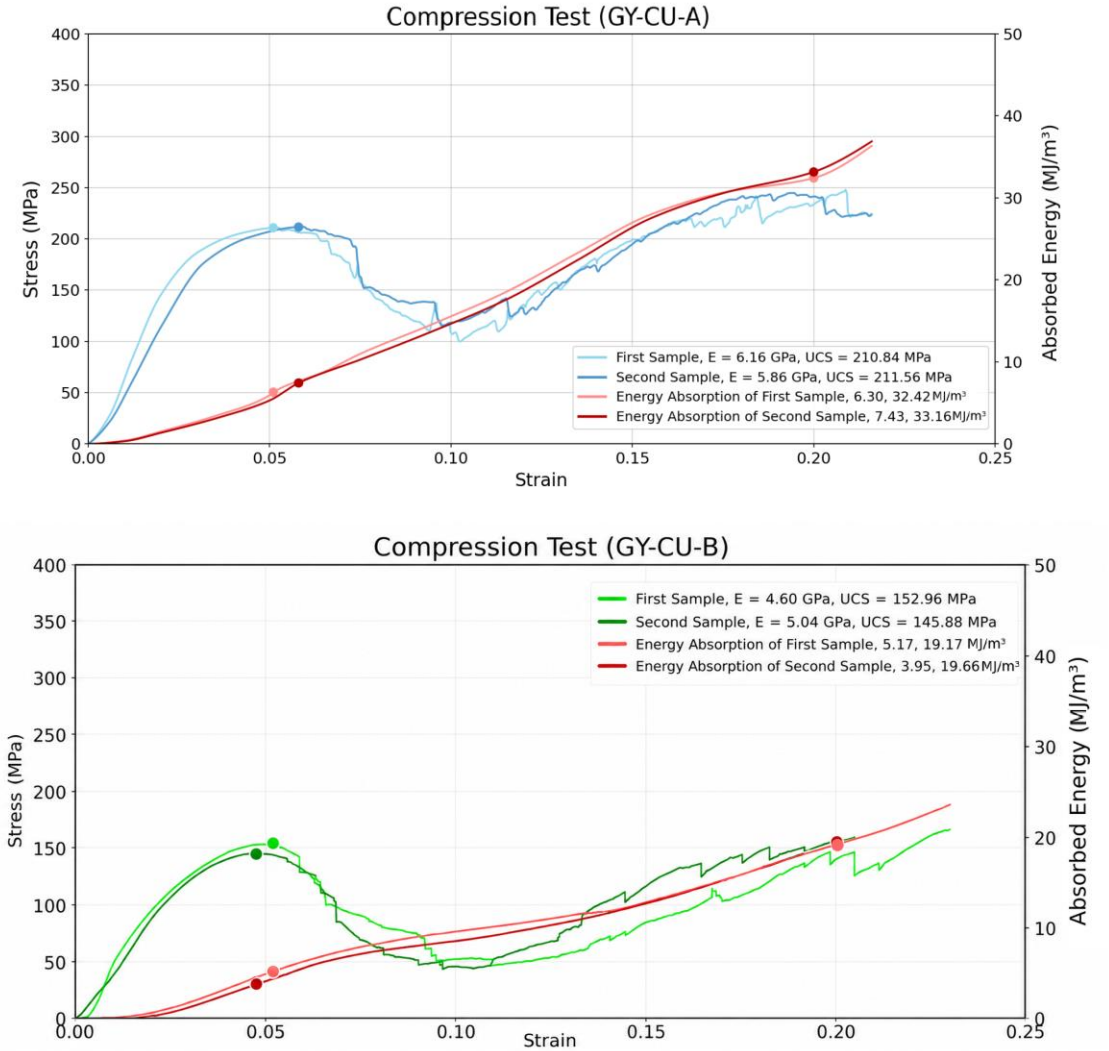

Figure 35. Experimental Compression Response and Absorbed Energy Evolution of the Cubic Gyroid Samples: GY-CU-A and GY-CU-B.

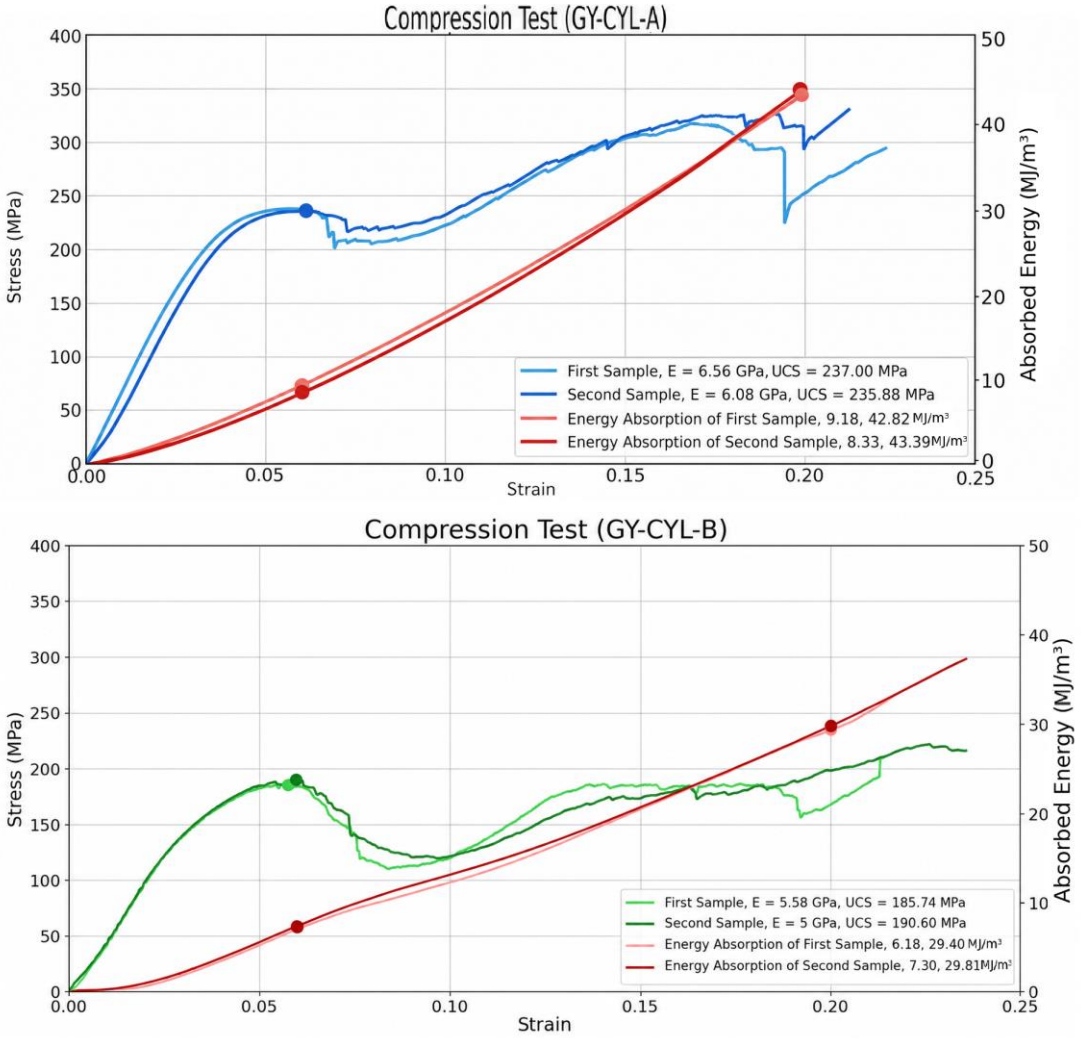

Figure 36. Experimental Compression Response and Absorbed Energy Evolution of the Cylindrical Gyroid Samples: GY-CYL-A and GY-CYL-B.

4.3.2 Split-P samples

The Split-P group included SP-CU-A, SP-CU-C, SP-CYL-A, and SP-CYL-C.

Among all tested samples, SP-CYL-A showed the highest average elastic modulus, equal to 6.46 GPa. This indicates that the cylindrical Split-P configuration had the stiffest initial response under compression. Its average UCS was also high, equal to 216.81 MPa, and its absorbed energy at 0.20 strain reached 38.25 MJ/m³.

When SP-CU-A and SP-CYL-A are compared, both samples have the same relative volume of 79%. However, SP-CYL-A showed better performance. The average elastic modulus increased from 6.16 GPa for SP-CU-A to 6.46 GPa for SP-CYL-A, and the UCS increased from 193.94 MPa to 216.81 MPa. The absorbed energy at 0.20 strain also increased from 34.49 MJ/m³ to 38.25 MJ/m³. This confirms that the cylindrical configuration improved the Split-P structure as well, although the improvement was slightly less pronounced than in the Gyroid group.

For the 75% relative-volume Split-P samples, SP-CYL-C also showed higher stiffness and UCS than SP-CU-C. The average elastic modulus increased from 5.55 GPa to 5.77 GPa, and the UCS increased from 177.60 MPa to 189.16 MPa. However, the absorbed energy values at 0.20 strain were very close, with 27.94 MJ/m³ for SP-CU-C and 28.10 MJ/m³ for SP-CYL-C. This shows that, at this relative volume, the cylindrical configuration mainly improved stiffness and UCS, while the improvement in energy absorption was limited.

In general, the Split-P samples showed strong stiffness performance. SP-CYL-A was the stiffest sample in the entire experimental set. However, when strength and energy absorption are considered together, GY-CYL-A still showed the best overall performance. This indicates that Split-P may be more suitable when stiffness is the main design requirement, while the cylindrical Gyroid configuration is more effective when both UCS and energy absorption are important. All these comparisons are shown visually in Figure 37 and Figure 38.

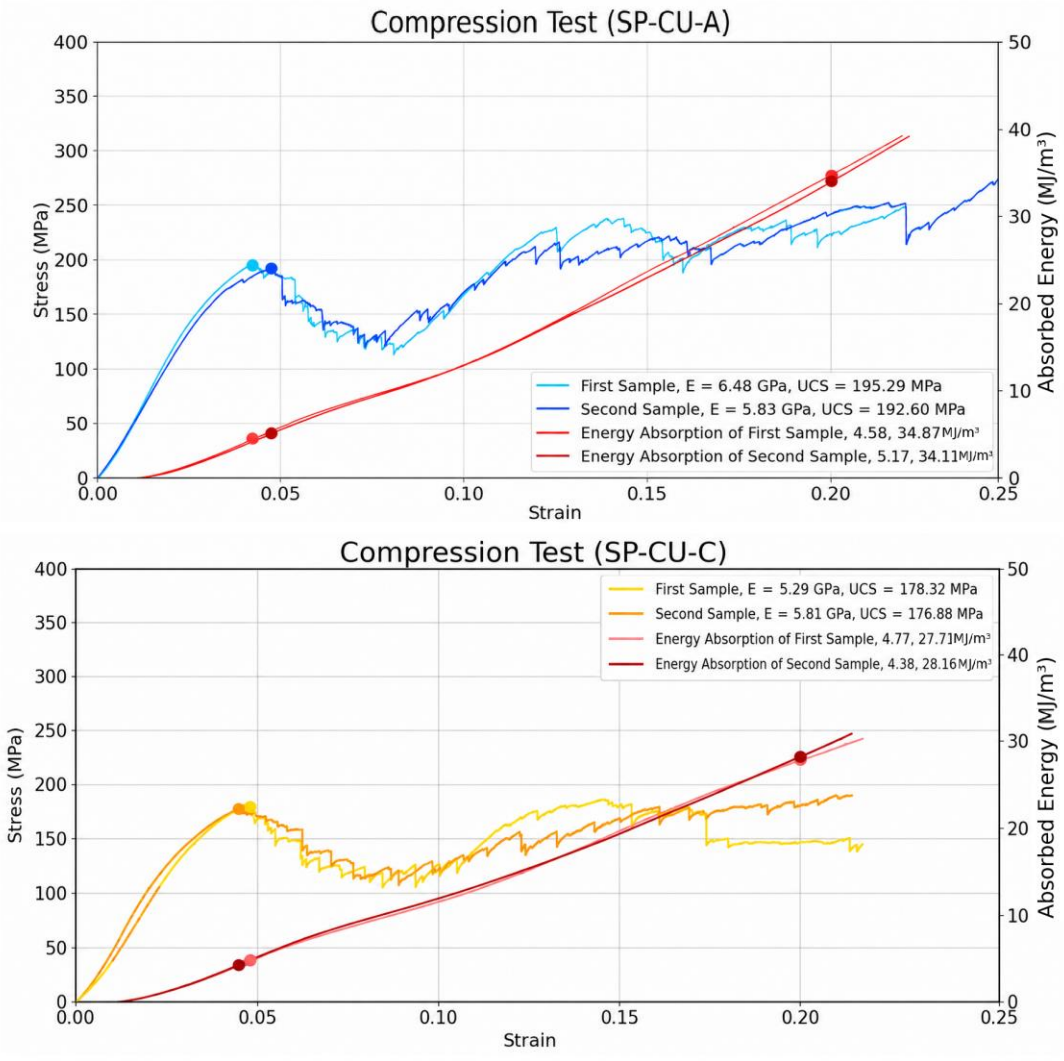

Figure 37. Experimental Compression Response and Absorbed Energy Evolution of the Cubic Split-P Samples: SP-CU-A and SP-CU-C.

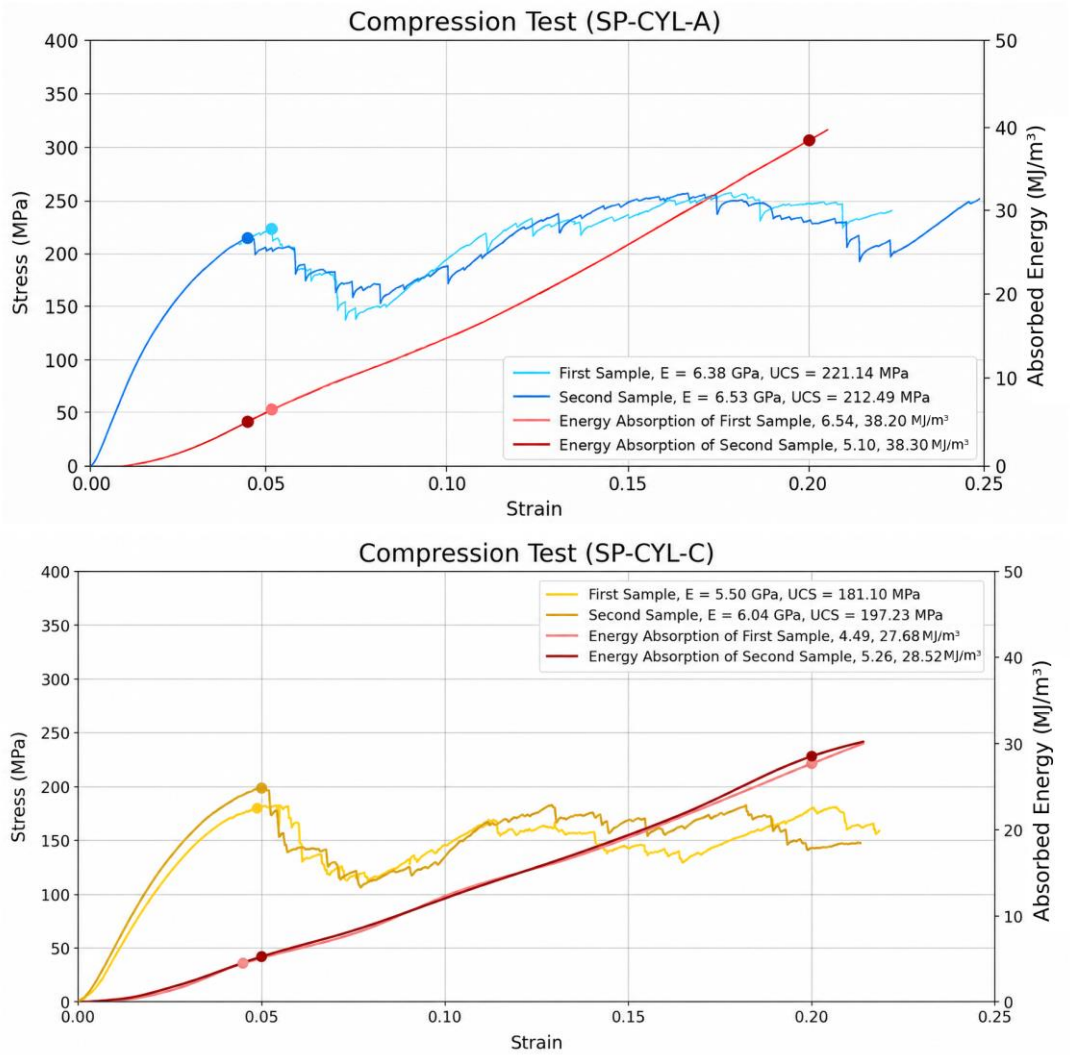

Figure 38. Experimental Compression Response and Absorbed Energy Evolution of the Cylindrical Split-P Samples: SP-CYL-A and SP-CYL-C.

4.3.3 Stochastic samples

The stochastic group included ST-A, ST-B, and ST-C. Compared with the Gyroid and Split-P samples, the stochastic structures generally showed lower mechanical performance.

ST-A, with 79% relative volume, showed the best response within the stochastic group. It had an average elastic modulus of 5.34 GPa, an average UCS of 156.09 MPa, and an absorbed energy of 29.63 MJ/m³ at 0.20 strain. However, even with the highest relative volume in the stochastic group, its UCS remained lower than most of the TPMS-based samples.

The weakest response was observed for ST-B. This sample had the lowest average elastic modulus, equal to 4.00 GPa, and the lowest UCS, equal to 95.31 MPa. It also had the lowest absorbed energy at 0.20 strain, with an average value of 15.32 MJ/m³. The compression

curves show that ST-B had a much lower stress level compared with the other samples, confirming its weaker load-bearing capacity.

ST-C showed intermediate behavior between ST-A and ST-B. Its average elastic modulus was 5.21 GPa, and its average UCS was 131.13 MPa. The absorbed energy at 0.20 strain was 19.70 MJ/m³. Although ST-C performed better than ST-B, it was still weaker than the Gyroid and Split-P samples with comparable relative volumes.

The lower performance of the stochastic structures may be related to their less regular internal architecture. Unlike the TPMS-based samples, which have continuous and periodic geometries, the stochastic structures can create less uniform load-transfer paths. This may lead to local stress concentration and earlier collapse in some regions of the structure. As a result, the global compression response becomes less stable and less efficient. All these comparisons are shown visually in Figure 39.

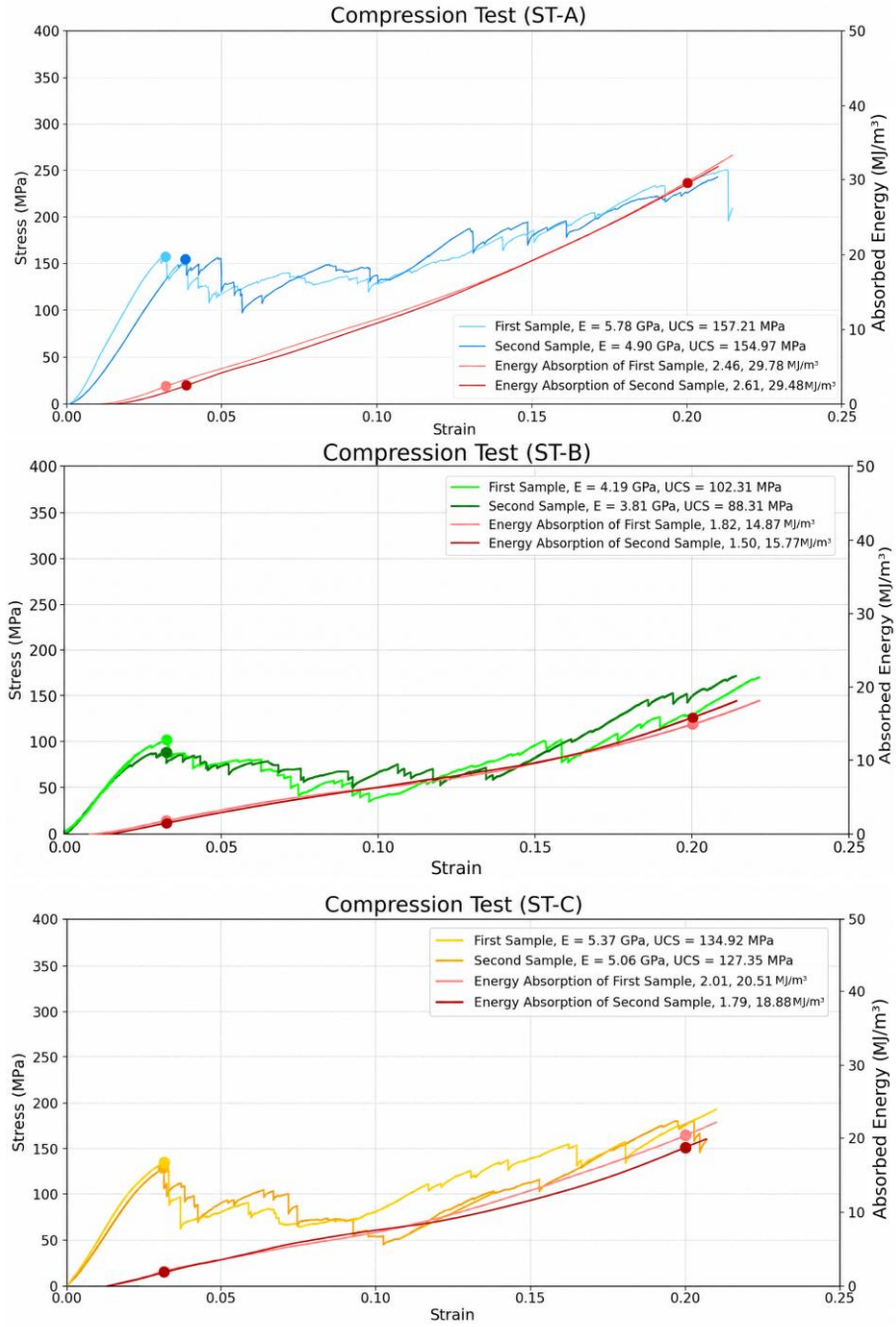

Figure 39. Experimental Compression Response and Absorbed Energy Evolution of the Stochastic Samples: ST-A, ST-B, and ST-C.

4.3.4 Overall comparison

The comparison between the three topology families shows that the Gyroid and Split-P structures generally performed better than the stochastic structures under compression. Among all samples, GY-CYL-A showed the highest UCS and the highest absorbed energy at 0.20 strain, while SP-CYL-A showed the highest elastic modulus. Therefore, the best-performing geometry depends on the target property. If the design priority is stiffness, SP-CYL-A is the most effective sample. If the priority is strength and energy absorption, GY-CYL-A provides the best overall response.

The results also confirm the positive effect of the cylindrical configuration. In both the Gyroid and Split-P families, the cylindrical samples generally showed higher stiffness, UCS, and absorbed energy than the corresponding cubic samples. This improvement was especially clear in the Gyroid group, where the cylindrical samples showed much higher UCS and absorbed energy than the cubic samples at the same relative volume.

Overall, the compression behavior of the lattice structures was controlled by the combined effect of relative volume, topology, and geometrical configuration. Higher relative volume generally improved the mechanical response, but the best results were obtained when the topology and sample configuration also allowed stable and efficient load transfer during compression.

4.4 XCT-Based Geometrical Deviation and Porosity Analysis

X-ray computed tomography was used to evaluate the as-built quality of the selected 79% relative-volume specimens: GY-CU-A, GY-CYL-A, SP-CU-A, SP-CYL-A, and ST-A. The aim was to check how closely the printed parts followed the nominal STL models and whether internal defects could help explain the mechanical behavior observed during compression. The analysis is presented in two parts: first the nominal/actual geometrical deviation, and then the internal porosity and inclusion analysis.

The nominal/actual comparison was used to compare the reconstructed XCT geometry with the original design. In the cumulative absolute deviation graphs, the horizontal axis represents the absolute deviation from the nominal geometry, while the vertical axis shows the percentage of analyzed surface accumulated up to that deviation value. A steeper curve would indicate that a larger portion of the surface is close to the nominal model. The signed deviation distribution graphs show how the surface deviations are distributed between negative and positive values. In practical terms, negative and positive deviations indicate surfaces located on opposite sides of the nominal geometry, which can be associated with local undersizing, oversizing, surface roughness, or material build-up. The ±0.08 mm range shown in the reports should be treated as the visualization range of the software output, not as a direct mean deviation value.

For the Gyroid samples, the cumulative graphs show that the deviation was concentrated at very small values only, meaning that the as-built surfaces had not noticeable local differences from the nominal STL model. The signed deviation distributions are broad, showing that both inward and outward deviations were present. This behavior is expected for LPBF lattice structures, especially around curved surfaces and internal channels and also in the location which the lattice is separated from its platform. In the deviation maps, the main differences are visible around the curved Gyroid walls and near the transition between the lattice core and the solid end caps. However, both GY-CU-A and GY-CYL-A preserved their general designed architecture. The outcomes of analyses are presented in Figure 40 and 41.

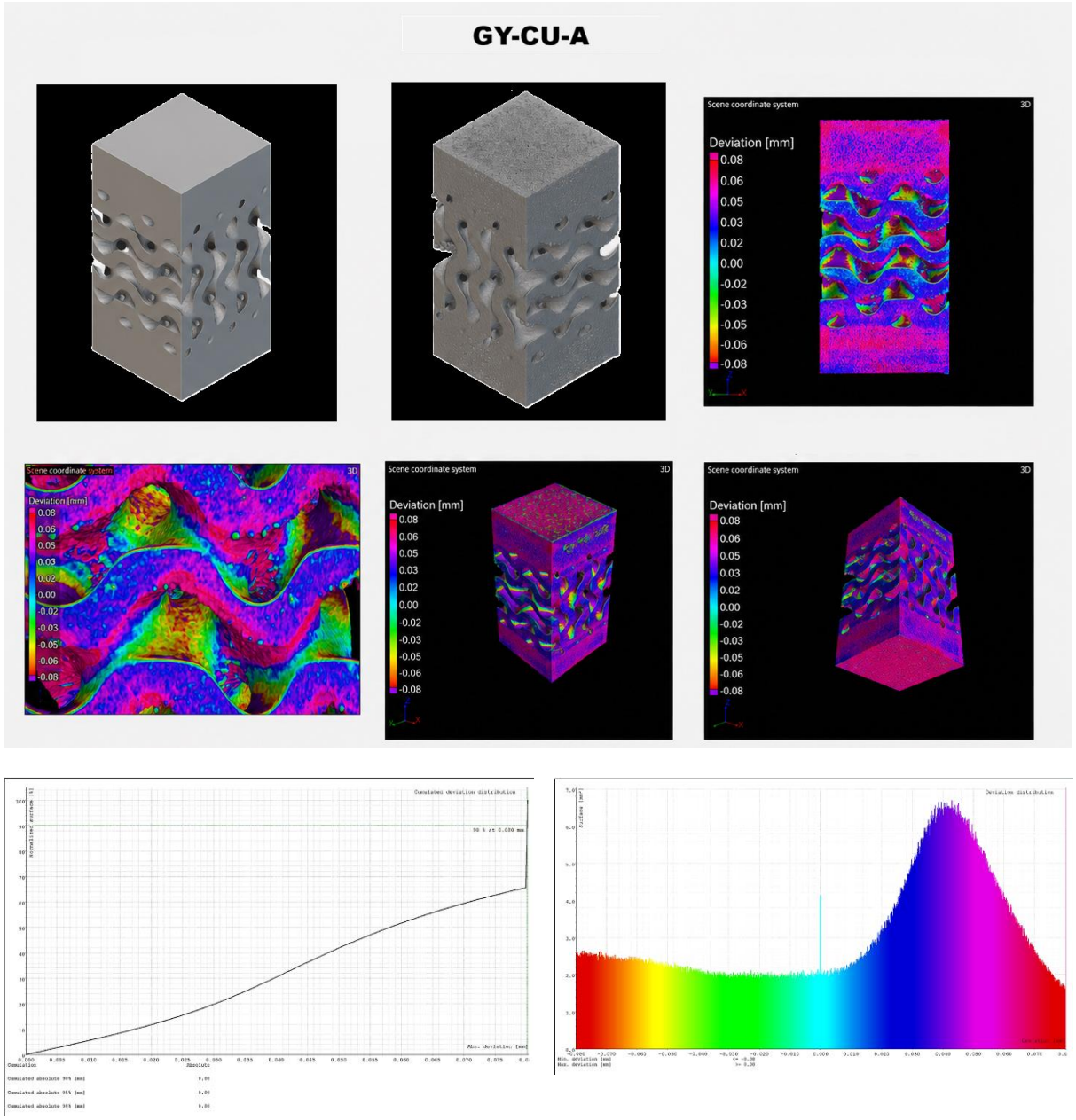

Figure 40. Nominal/Actual Deviation Analysis of GY-CU-A.

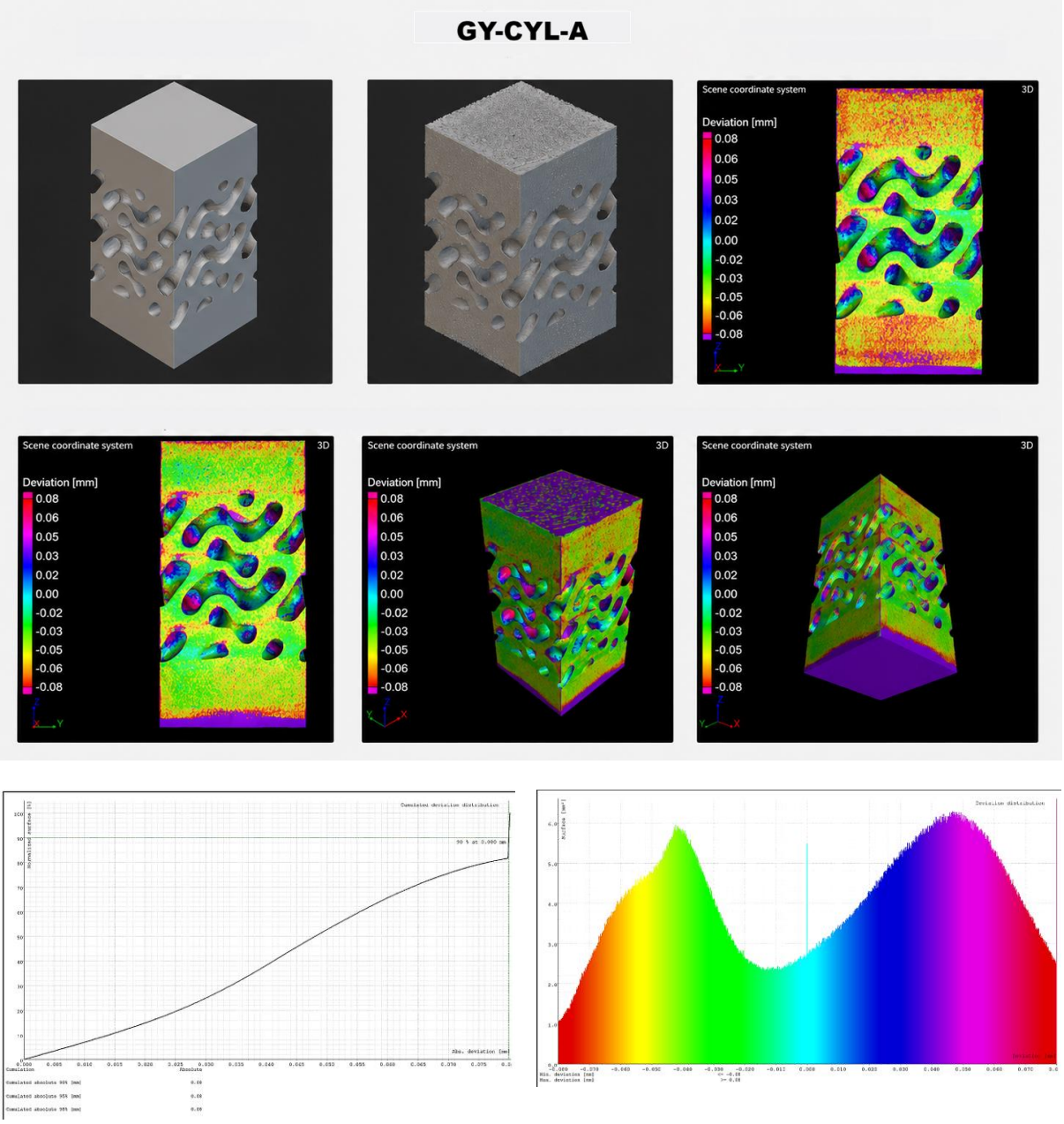

Figure 41. Nominal/Actual Deviation Analysis of GY-CYL-A.

In Figure 42, scanned top surface of GY-CU-A is presented, which shows perfectly an example of local deviation between designed and built sample.

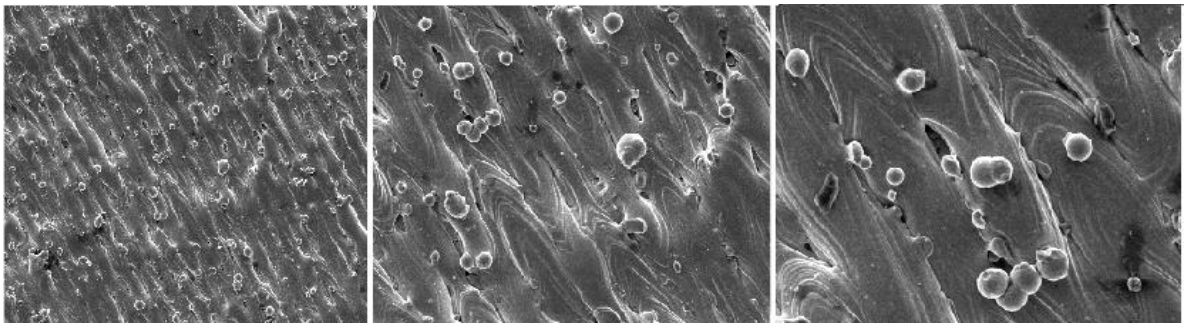

Figure 42. Scanned Top Surface of GY-CU-A.

For the Split-P samples, the cumulative deviation curves again confirm that the printed surfaces were not identical to the nominal geometry. The signed deviation distributions show two main deviation regions, meaning that both excess material and local material deficiency were present on the analyzed surfaces. This is visible in the deviation maps in Figure 43 and 44, where the colored regions are mainly located around the lattice openings and the solid-lattice transition zones. SP-CYL-A still preserved its cylindrical Split-P geometry clearly, which is consistent with its high elastic modulus measured during compression.

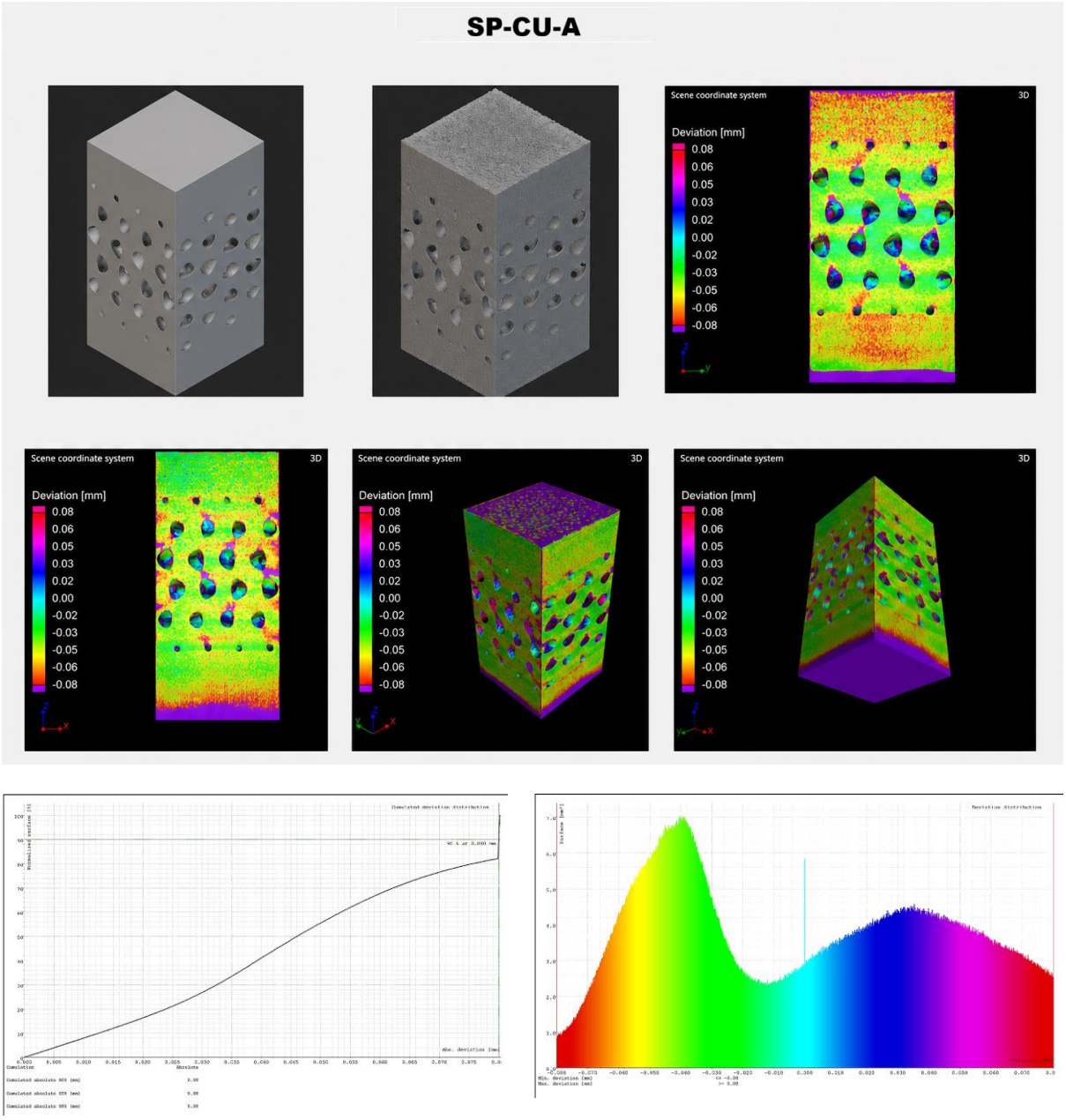

Figure 43. Nominal/Actual Deviation Analysis of SP-CU-A.

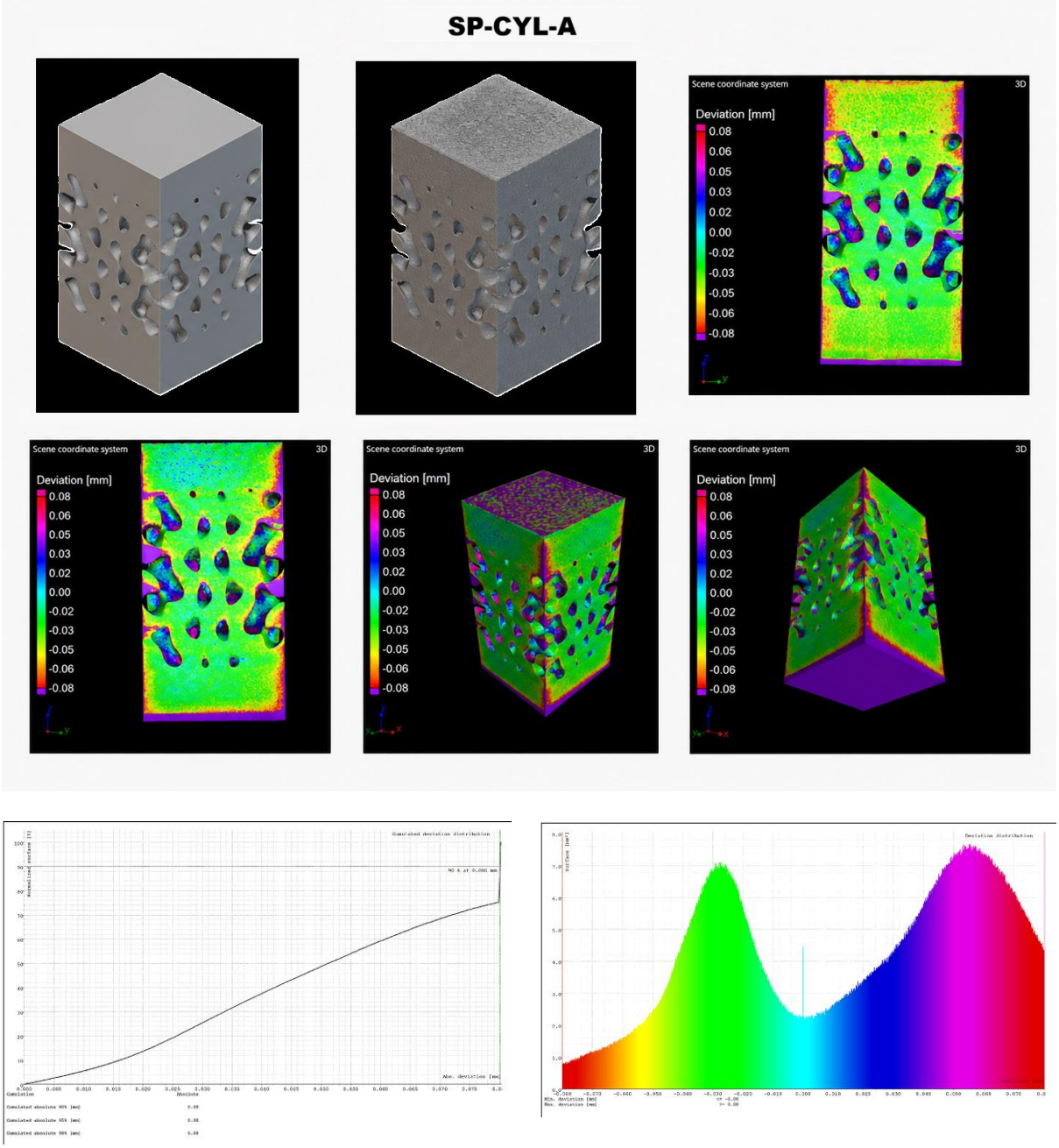

Figure 44. Nominal/Actual Deviation Analysis of SP-CYL-A.

The stochastic sample showed a different deviation behavior. Its signed deviation distribution is less balanced and more irregular compared with the TPMS-based samples, as shown in Figure 45. This reflects the non-periodic nature of the stochastic architecture, where the local wall orientations and internal connections are less uniform. The deviation maps show localized differences around irregular internal connections and near the solid end regions. This irregular as-built geometry may have contributed to the lower UCS and absorbed energy of ST-A compared with the Gyroid and Split-P samples.

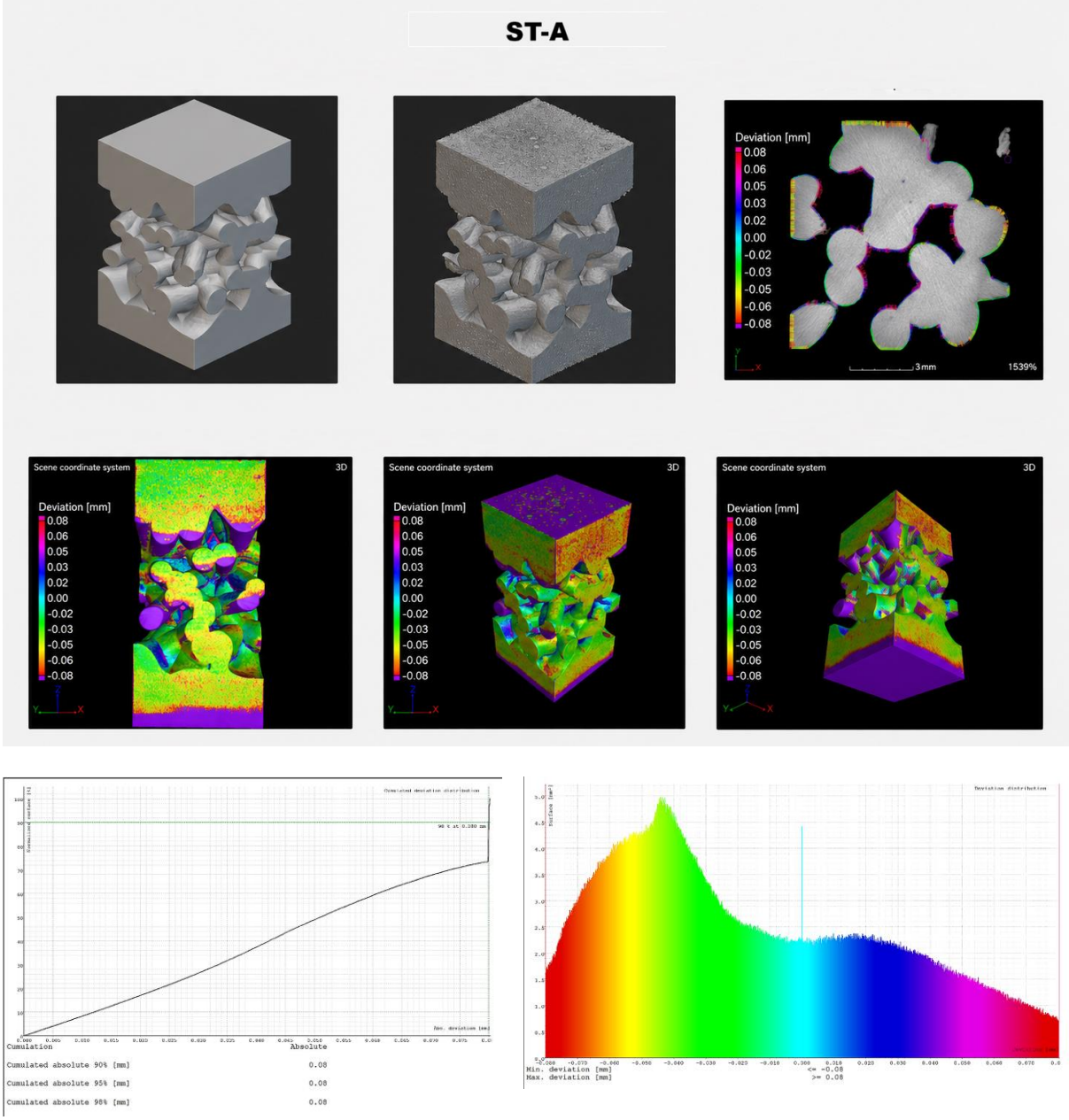

Figure 45. Nominal/Actual Deviation Analysis of ST-A.

Overall, the deviation results show that all selected samples were successfully manufactured with their intended global architecture, but local differences from the nominal STL model were present in every case. These deviations were mainly located around internal openings, curved walls, external surfaces, separation place from the platform, and solid-lattice transition regions. This is important for the later numerical comparison, because ideal Abaqus models cannot fully represent the real surface roughness, powder adhesion, and local as-built deviations observed by XCT.

The second part of the XCT analysis focused on internal porosity and inclusions. Here, only unintended defects inside the solid material volume were considered. The designed lattice openings were not counted as defects. The main quantitative results are summarized in Table 12.

Table 12. XCT-based Internal Defect Summary Extracted from Dragonfly Porosity Reports.

Sample	Material volume [mm³]	Defect volume [mm³]	Defect volume ratio [%]	Defect surface [mm²]
GY-CU-A	5128.44	0.39	0.01	24.90
GY-CYL-A	5173.23	0.31	0.01	17.61
SP-CU-A	5125.00	0.14	0.01	7.90
SP-CYL-A	5299.94	0.92	0.02	41.56
ST-A	4989.76	1.00	0.02	54.43

In Table 12, material volume refers to the solid volume analyzed in Dragonfly. Defect volume is the total volume of the detected internal defects, while defect volume ratio expresses this value relative to the material volume. Defect surface gives additional information about the morphology and distribution of the defects: for example, a larger defect surface can indicate a more distributed or more irregular defect population, even when the total defect volume is still low.

The porosity figures include three types of information. The defect diameter distribution graph shows the equivalent diameter of the detected defects. The diameter–sphericity graph shows the shape tendency of the defects, values closer to 1 represent more spherical pores, while lower values indicate more irregular or elongated defects. The merged porosity views show where the detected defects are located inside the sample and whether they are scattered or concentrated in specific regions.

For the Gyroid samples, the defect volume was low in both cases. GY-CU-A showed a defect volume of 0.39 mm³, while GY-CYL-A showed a slightly lower value of 0.31 mm³. The diameter distribution graphs indicate that the detected defects were mostly small and isolated, with only a few larger features. The diameter–sphericity plots show that many defects were not perfectly spherical, which is typical for LPBF defects and small segmented inclusions. The merged porosity views confirm that the defects were scattered within the material volume rather than forming one large continuous defective region. Therefore, the stronger mechanical response of GY-CYL-A should be mainly linked to its cylindrical Gyroid load path, not only to its slightly lower defect volume. These analyses came in Figure 46 and Figure 47.

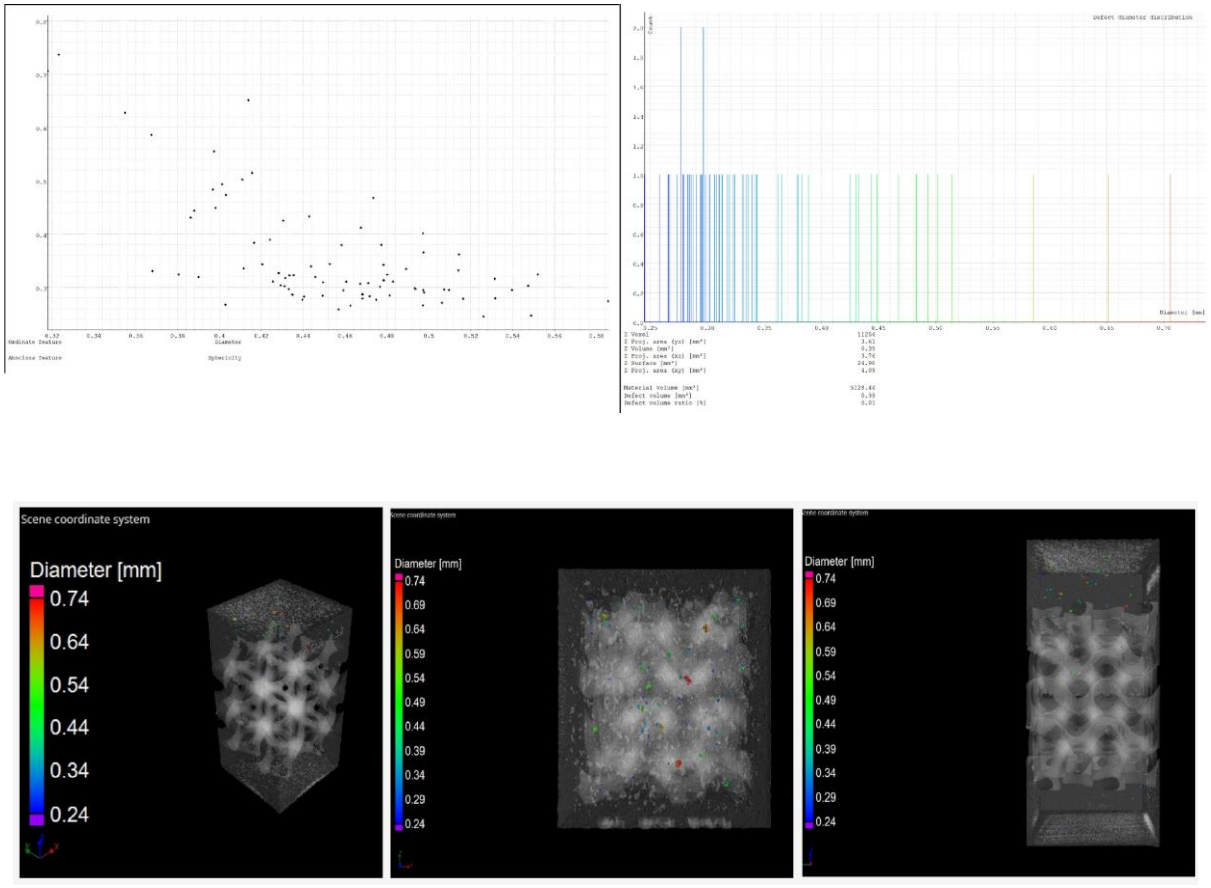

Figure 46. XCT Porosity Analysis of GY-CU-A.

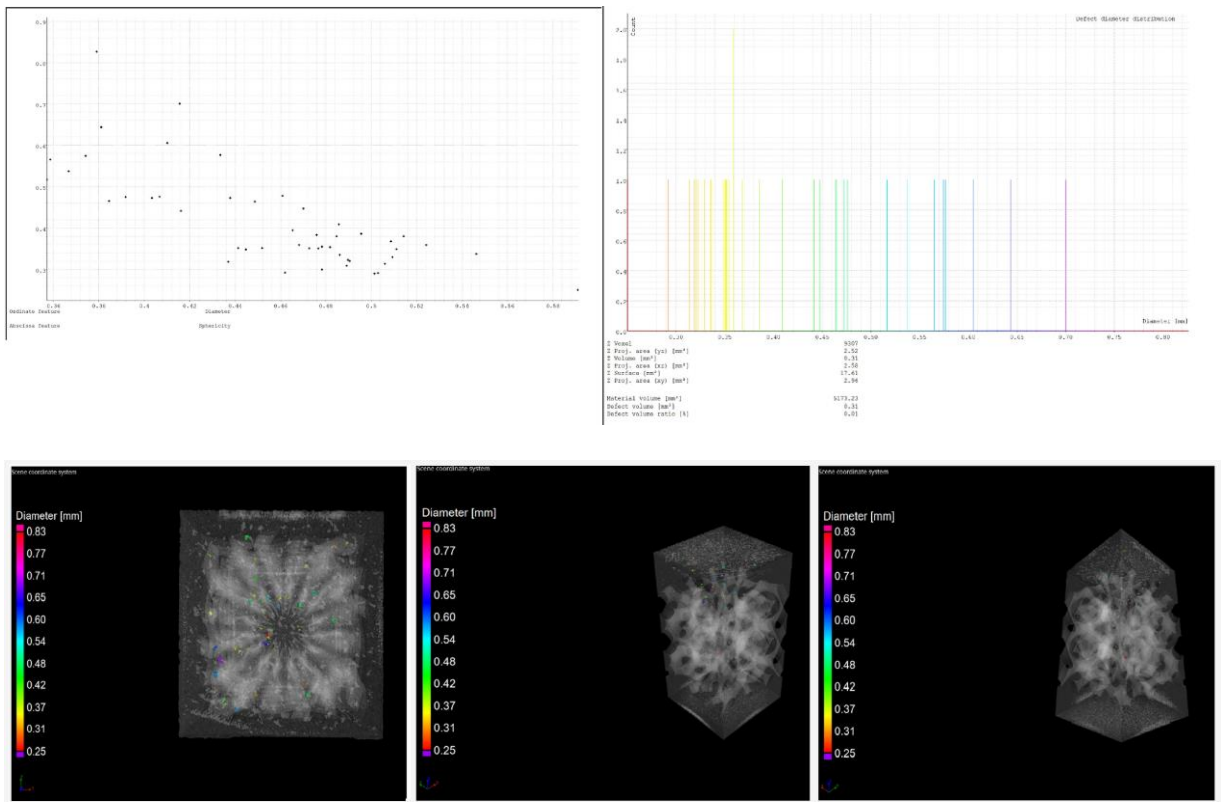

Figure 47. XCT Porosity Analysis of GY-CYL-A.

For the Split-P samples, SP-CU-A had the lowest defect volume and defect surface among all inspected specimens, with 0.14 mm³ and 7.90 mm², respectively. Its defect diameter distribution is limited, showing fewer detected defects compared with the other samples. SP-CYL-A, on the other hand, had a higher defect volume of 0.92 mm³ and a larger defect surface of 41.56 mm². Its porosity graphs show a more distributed defect population. However, SP-CYL-A still showed higher stiffness during compression. This confirms that the mechanical response was not controlled only by internal porosity; the cylindrical Split-P configuration provided a more effective load-bearing path in the initial compression stage. These analyses came in Figure 48 and Figure 49.

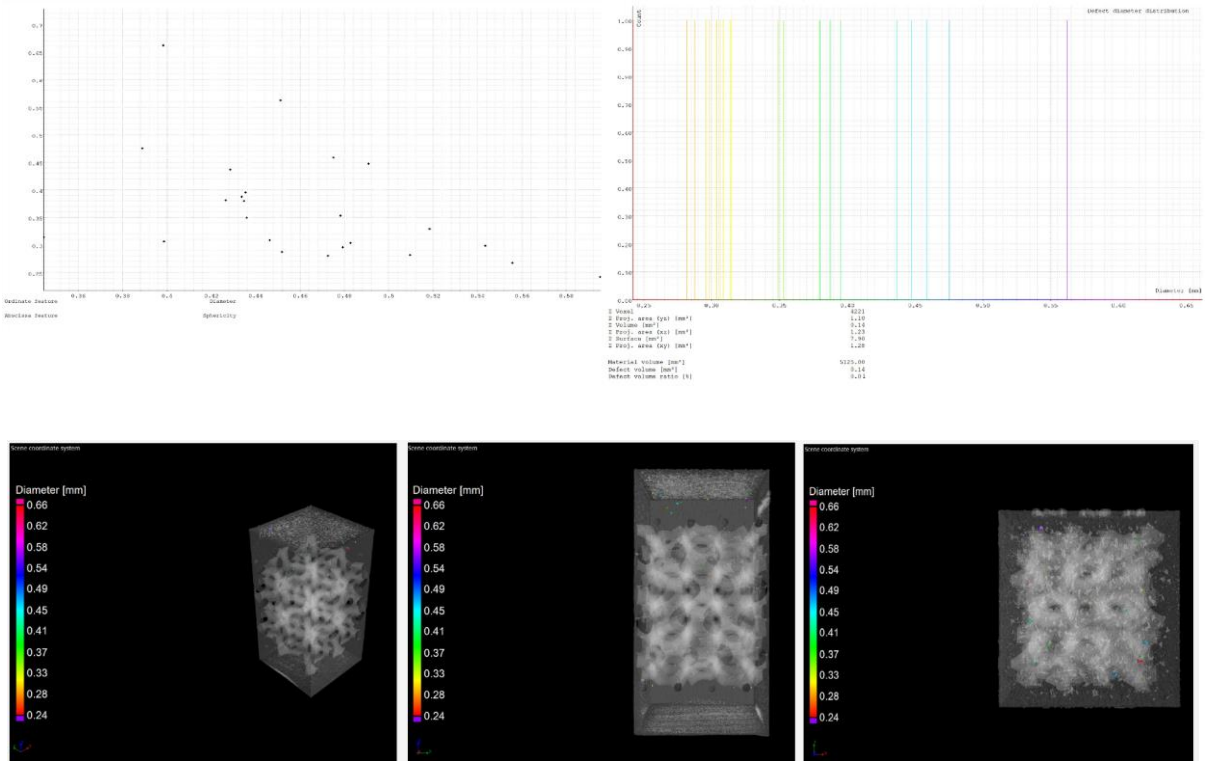

Figure 48. XCT Porosity Analysis of SP-CU-A.

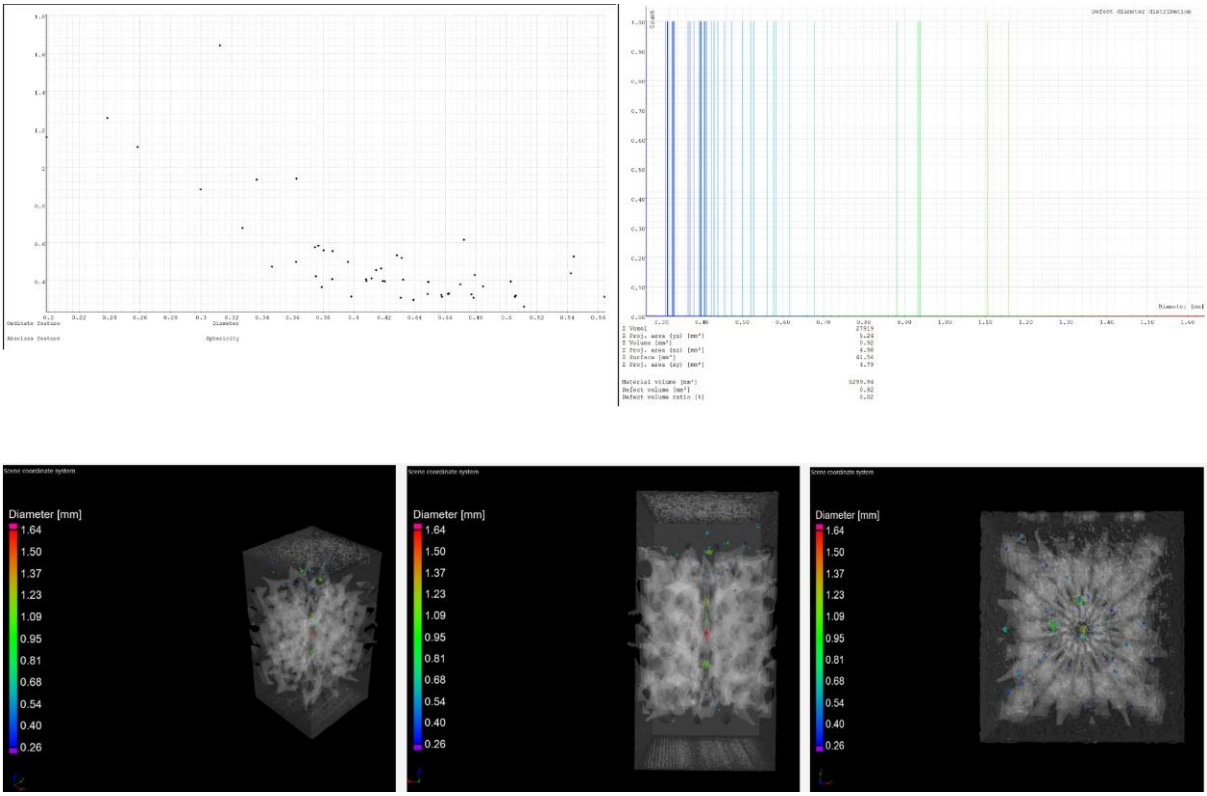

Figure 49. XCT Porosity Analysis of SP-CYL-A.

ST-A showed the highest defect volume and defect surface, equal to 1.00 mm^3 and 54.43 mm^2. Its defect diameter distribution is wider than the other samples and includes more scattered detected features. The diameter–sphericity plot also suggests that many defects were irregular rather than highly spherical. The merged porosity views show that these defects were distributed through the structure. However, the defect volume ratio was still only 0.02%, so the weaker mechanical performance of ST-A should not be explained by porosity alone. A more reasonable interpretation is that the stochastic architecture created less uniform load transfer, while its higher defect content and irregular deviation pattern further promoted local collapse. These analyses came in Figure 50.

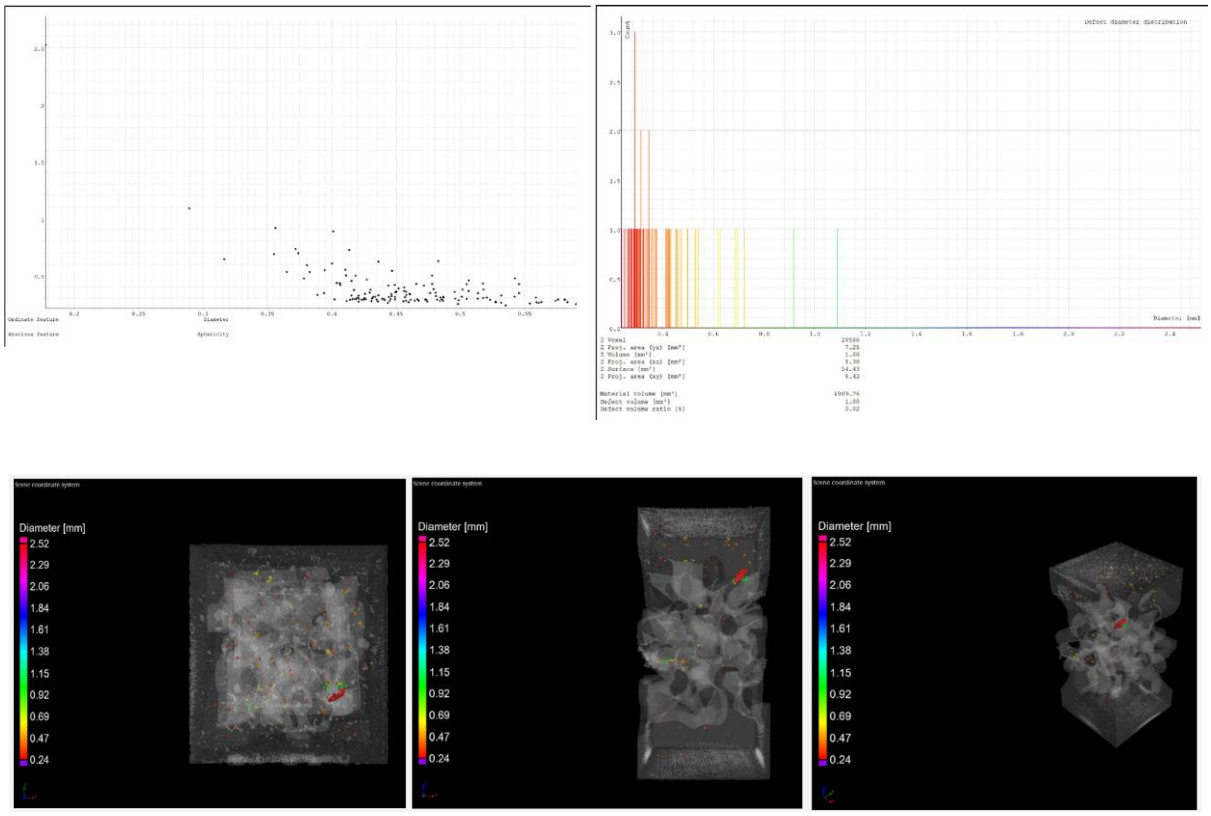

Figure 50. XCT Porosity Analysis of ST-A.

In summary, the XCT results show that all samples had low internal defect ratios, indicating acceptable LPBF material quality. The main differences in compression behavior were therefore governed more by topology and cell mapping than by porosity alone. GY-CYL-A and SP-CYL-A performed well because their cylindrical configurations created more effective load-transfer paths. In contrast, ST-A was affected by a combination of irregular geometry, less uniform stress distribution, higher defect volume, and a more irregular deviation pattern. These XCT observations also explain why some differences should be expected between the experimental results and ideal numerical simulations.

4.5 Abaqus Simulation Results and Experimental Validation

This section presents the Abaqus simulation results for the fully dense bulk reference and for the 79% relative-volume lattice specimens. The purpose of the numerical analysis is to support the experimental compression results by identifying the stress localization zones, reproducing the global stress-strain response, and evaluating how accurately the finite element models can predict the elastic modulus, ultimate compressive strength, and absorbed energy of the printed structures.

As described in the methodology chapter, the numerical models were developed in Abaqus/Explicit using the same reference area and height used for the experimental stress-strain conversion. The comparison is therefore based on engineering stress, engineering

strain, and absorbed energy calculated in a consistent way for the experimental and numerical results. The selected lattice group includes GY-CU-A, GY-CYL-A, SP-CU-A, SP-CYL-A, and ST-A. These samples allow a direct comparison between Gyroid, Split-P, and stochastic architectures at the same relative-volume level.

The stress contour plots were interpreted together with the final compressed specimens and the stress-strain curves. In this way, the numerical results were not treated only as curve-fitting outputs. They were used to understand where the main deformation developed, why some samples carried higher loads, and why the numerical predictions were slightly different from the experimental measurements.

4.5.1 Bulk reference sample

Before discussing the lattice specimens, the fully dense bulk reference was considered as a baseline. The bulk sample does not collapse through internal lattice walls or pores. Instead, it deforms as a continuous solid body. For this reason, the von Mises stress field is smoother than in the lattice samples, and the highest stress zone appears mainly in the central region of the specimen, where the barreling deformation is more evident during compression.

The bulk compression response gives a useful reference for understanding the effect of introducing lattice architecture. The bulk specimen reached a yield stress of approximately 506 MPa, and the absorbed energy up to the selected yield point was 21.7 MJ/m³. Although the bulk sample has a much higher stress level than the lattice structures, the lattices are more relevant for controlled progressive collapse and energy absorption at reduced material volume. Therefore, the bulk result is used here as a mechanical reference, while the numerical-experimental validation is focused on the lattice samples. In Figure 51 the Abaqus simulation and stress-strain curve of our bulk sample are presented.

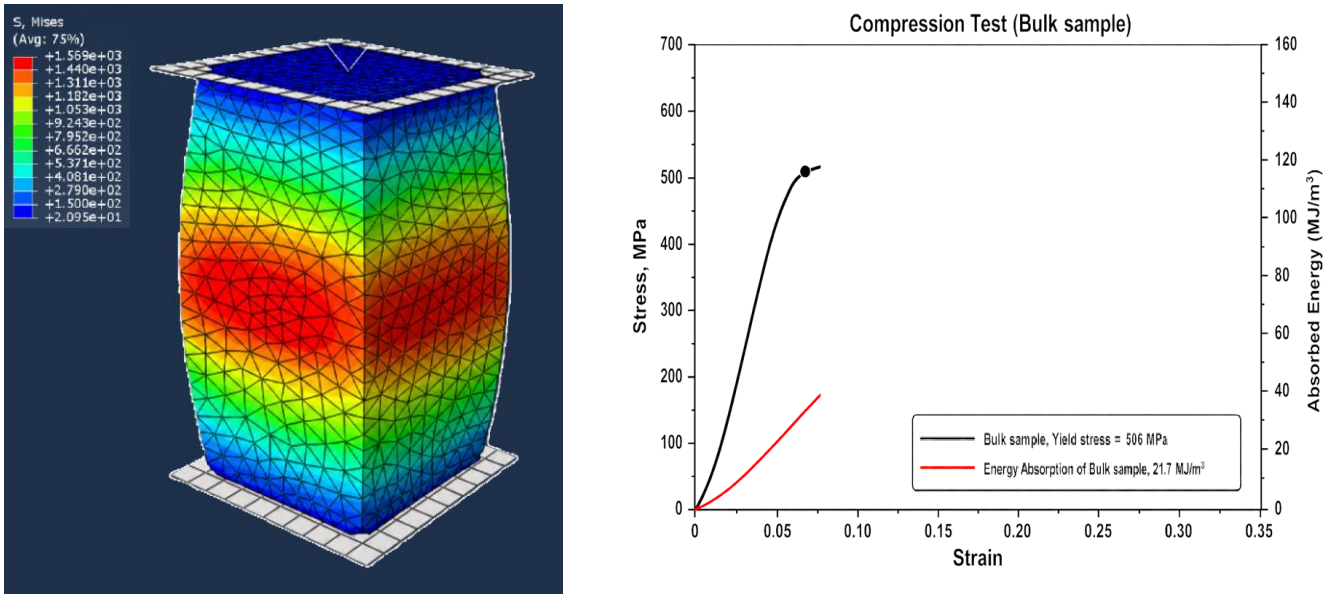

Figure 51. Abaqus Simulation and Stress-Strain Curve of Bulk Sample.

4.5.2 Quantitative comparison between Abaqus and experimental results

For each lattice specimen, the two experimental repetitions were averaged and compared with the corresponding Abaqus prediction. The main comparison parameters are the elastic modulus, UCS, and absorbed energy at 0.20 strain. The absorbed energy at 0.20 strain was selected because it represents the ability of the structure to continue absorbing energy after the first major collapse event, and it is therefore more representative for energy-absorbing lattice behavior than the first peak alone. This comparison is shown in Table 13.

Table 13. Experimental Average Values and Abaqus Simulation results for the 79% Relative Volume Lattice Specimens, (E: Elastic Modulus, UCS: Ultimate Compression Stress, EA: Energy Absorbed).

Sample	Exp. E (GPa)	Abaqus E (GPa)	Exp. UCS (MPa)	Abaqus UCS (MPa)	Exp. EA at 0.20 strain (MJ/m³)	Abaqus EA at 0.20 strain (MJ/m³)
GY-CU-A	6.01	6.04	211.20	223.95	32.79	34.31
GY-CYL-A	6.32	6.90	236.44	254.68	43.11	49.14
SP-CU-A	6.16	6.72	193.94	215.50	34.49	36.60
SP-CYL-A	6.46	7.27	216.81	234.00	38.25	40.35
ST-A	5.34	5.15	156.09	168.89	29.63	30.32

The signed percentage error was calculated according to Equation 4:

$$\text{Error (\%)} = [(\text{Abaqus value} - \text{experimental average value}) / \text{experimental average value}] \times 100 \quad (4)$$

A positive value means that the Abaqus model overestimated the experimental result, while a negative value means that the numerical result was lower than the experimental average. The calculated errors are shown in Table 14.

Table 14. Signed Percentage Error Between Abaqus Simulation and Experimental Average Values.

Sample	E signed error (%)	UCS signed error (%)	EA0.20 signed error (%)
GY-CU-A	+0.50	+6.04	+4.64
GY-CYL-A	+9.18	+7.71	+13.99
SP-CU-A	+9.09	+11.11	+6.12
SP-CYL-A	+12.54	+7.86	+5.49
ST-A	-3.56	+8.20	+2.33
Average absolute error	6.97	8.18	6.51

The average absolute errors are approximately 7.00% for elastic modulus, 8.18% for UCS, and 6.51% for absorbed energy at 0.20 strain. These values show that the numerical models reproduced the global compression behavior with acceptable accuracy. The strongest difference appears in cases where the real printed structure experienced earlier local collapse or stronger post-yield fluctuations than the ideal model. This is expected because the Abaqus models were based on the designed geometry and did not explicitly include every as-built defect, local wall-thickness deviation, surface roughness, powder adhesion, micro-crack initiation, or fracture event.

The comparison also shows that Abaqus generally overestimated UCS and absorbed energy. This trend is reasonable for ideal-geometry lattice models. In the real printed samples, the load paths are affected by LPBF-induced surface irregularities, local geometrical deviations observed in the XCT analysis, and small internal defects. These features can reduce the effective load-bearing area and trigger local deformation earlier than in the ideal numerical model. Moreover, the material model used in the simulations reproduced plastic deformation but did not explicitly remove elements after local fracture. Therefore, the simulated curves remain smoother and can maintain higher stress levels after the first collapse region forms.

4.5.3 Gyroid cubic sample: GY-CU-A

The GY-CU-A sample showed the closest agreement in elastic modulus among all lattice specimens. The experimental average elastic modulus was 6.01 GPa, while Abaqus predicted

6.04 GPa. This very small difference indicates that the initial stiffness of the cubic Gyroid architecture was captured effectively by the model. The UCS was moderately overestimated, with 223.95 MPa predicted numerically compared with 211.20 MPa experimentally. The absorbed energy at 0.20 strain was also slightly higher in the simulation, with 34.31 MJ/m³ compared with the experimental average of 32.79 MJ/m³.

As shown in Figure 52, the stress contour of GY-CU-A shows that the main stress concentration developed around the central region of the lattice, especially along the curved Gyroid walls involved in the collapse band. This is consistent with the final compressed specimen, where the strongest deformation was visible around the middle of the sample. The top and bottom regions remained comparatively more stable because they acted mainly as load-transfer zones near the compression plates. Figure 53 shows the experimental and Abaqus simulation responses of the compression test.

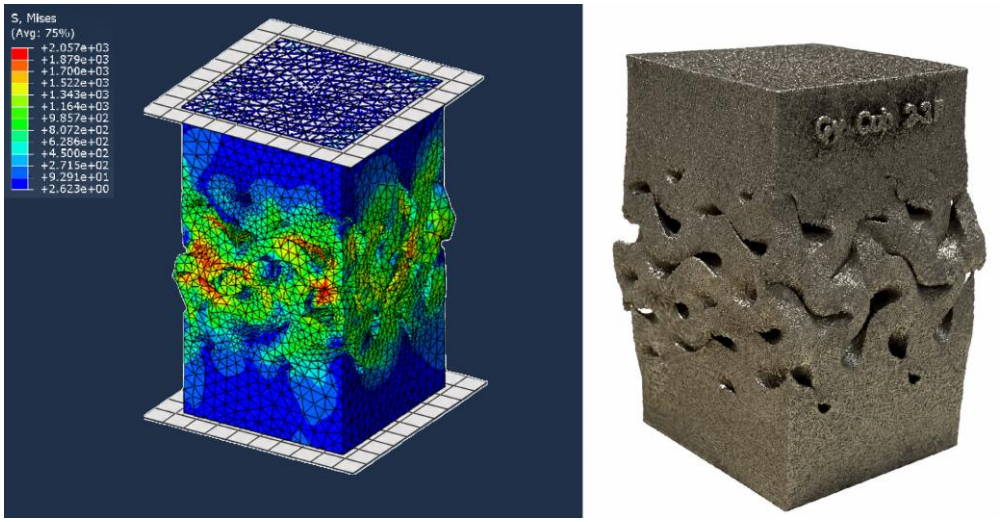

Figure 52. GY-CU-A Deformation Comparison: Abaqus Stress Distribution and Experimental Compressed Specimen.

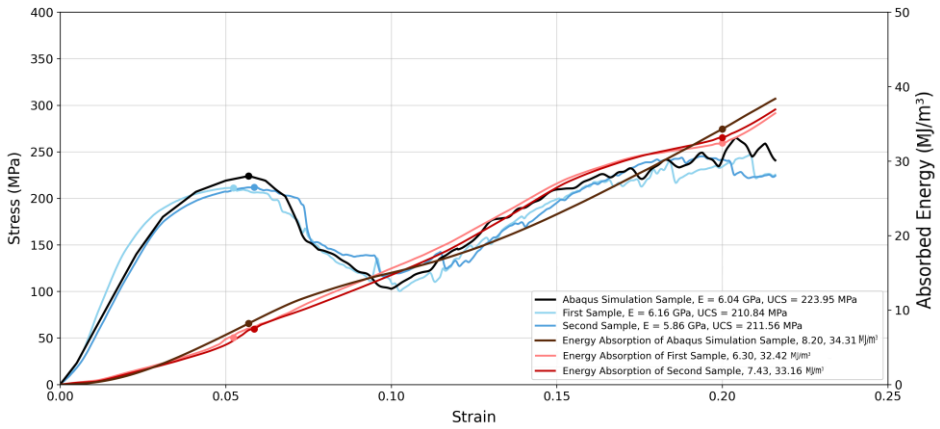

Figure 53. Experimental and Abaqus Compression Response Comparison for GY-CU-A.

4.5.4 Gyroid cylindrical sample: GY-CYL-A

The GY-CYL-A sample showed the highest overall mechanical performance among the studied lattice structures. Experimentally, it reached the highest UCS, equal to 236.44 MPa, and the highest absorbed energy at 0.20 strain, equal to 43.11 MJ/m³. Abaqus predicted the same performance ranking, with a UCS of 254.68 MPa and an absorbed energy of 49.14 MJ/m³. Although these values are higher than the experimental averages, the model correctly identified the cylindrical Gyroid design as the most efficient structure in terms of strength and energy absorption.

The stress distribution of GY-CYL-A is broader and more continuous than that of GY-CU-A. The high-stress region extends through a large part of the central lattice zone, which suggests a more effective load transfer during compression. The final compressed specimen also confirms this behavior, since the cylindrical Gyroid sample maintained a relatively stable deformation pattern and continued carrying load after the initial stress drop. The main reason for the larger numerical error in absorbed energy is that the ideal model preserved a higher post-yield stress level than the real printed specimen, where local imperfections and collapse events reduced the energy absorption capacity. In Figure 54 and 55 the stress distribution and compression responses in experimental and Abaqus simulation are shown.

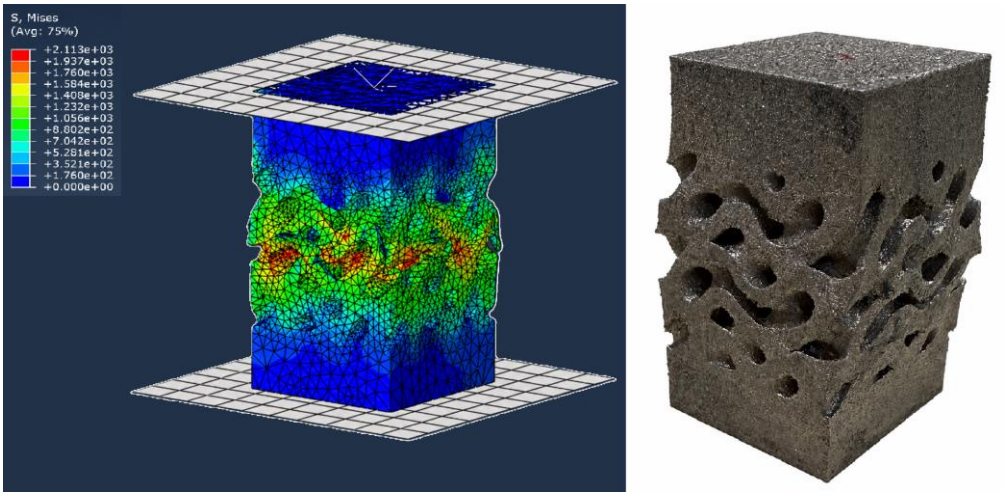

Figure 54. GY-CYL-A Deformation Comparison: Abaqus Stress Distribution and Experimental Compressed Specimen.

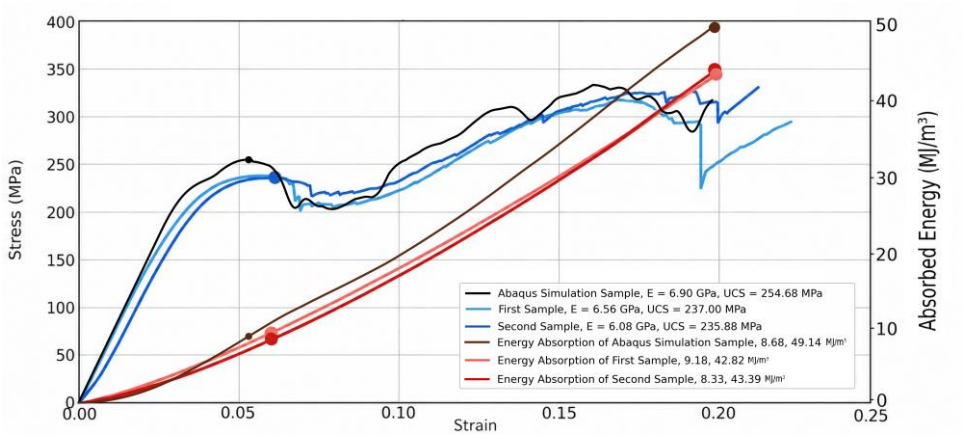

Figure 55. Experimental and Abaqus Compression Response Comparison for GY-CYL-A.

4.5.5 Split-P cubic sample: SP-CU-A

The experimental average elastic modulus was 6.16 GPa, while Abaqus predicted 6.72 GPa. The experimental UCS was 193.94 MPa, compared with 215.50 MPa in the simulation. The absorbed energy at 0.20 strain was 34.49 MJ/m³ experimentally and 36.60 MJ/m³ numerically. Therefore, the simulation captured the global energy absorption reasonably well, while the UCS was the most overestimated parameter for this sample.

The stress distribution of SP-CU-A shows localized high-stress regions around the internal Split-P walls and openings, as it is visible in Figure 56. Compared with the Gyroid architecture, the stress field appears less continuous and more concentrated in selected curved regions. This explains why the real sample can start local collapse earlier than the ideal model. Even if the XCT analysis showed a relatively good internal quality for this sample, the real as-built geometry still contains surface roughness, local wall-thickness deviations, and small irregularities that affect the collapse initiation. These effects are not fully represented in the ideal Abaqus model. In Figure 57 experimental and Abaqus compression response comparison for SP-CU-A is shown.

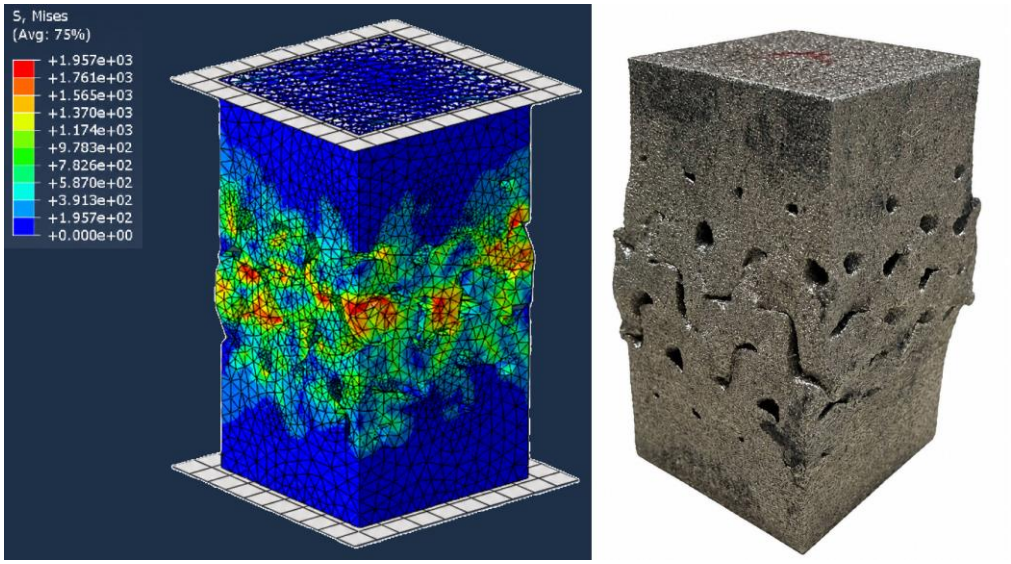

Figure 56. SP-CU-A Deformation Comparison: Abaqus Stress Distribution and Experimental Compressed Specimen.

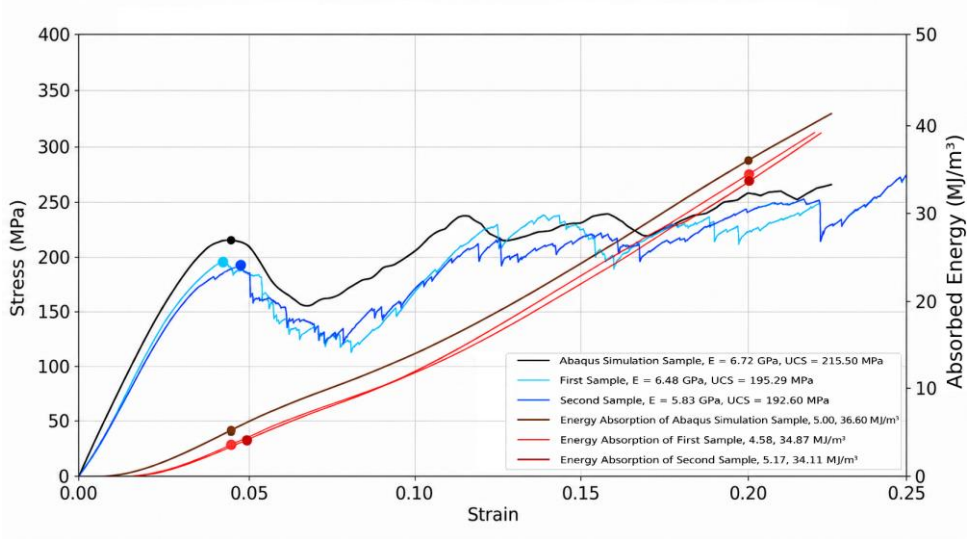

Figure 57. Experimental and Abaqus Compression Response Comparison for SP-CU-A.

4.5.6 Split-P cylindrical sample: SP-CYL-A

The SP-CYL-A sample presented the highest experimental elastic modulus among the lattice specimens, with an average value of 6.46 GPa. This indicates that the cylindrical Split-P configuration provided the stiffest initial response. Abaqus predicted an elastic modulus of 7.27 GPa, which corresponds to the largest stiffness overestimation among the samples. The UCS was also overestimated, with 234.00 MPa predicted numerically compared with 216.81 MPa experimentally. However, the absorbed energy at 0.20 strain was predicted with good accuracy: 40.35 MJ/m³ numerically compared with 38.25 MJ/m³ experimentally.

The stress contour of SP-CYL-A, which is presented in Figure 58, shows the formation of high-stress zones around the central part of the lattice and around several internal curved walls. The experimental compressed specimen shows a similar central collapse region, while the upper and lower solid zones remain less damaged. The strong stiffness response of this design can be related to its cylindrical configuration and load-transfer continuity. The difference between numerical and experimental stiffness is mainly related to the ideal geometry used in Abaqus, because small deviations in wall thickness, local contact, and alignment can strongly influence the initial slope of a stiff lattice sample. In Figure 59, the results of experimental and numerical simulation compression test are presented.

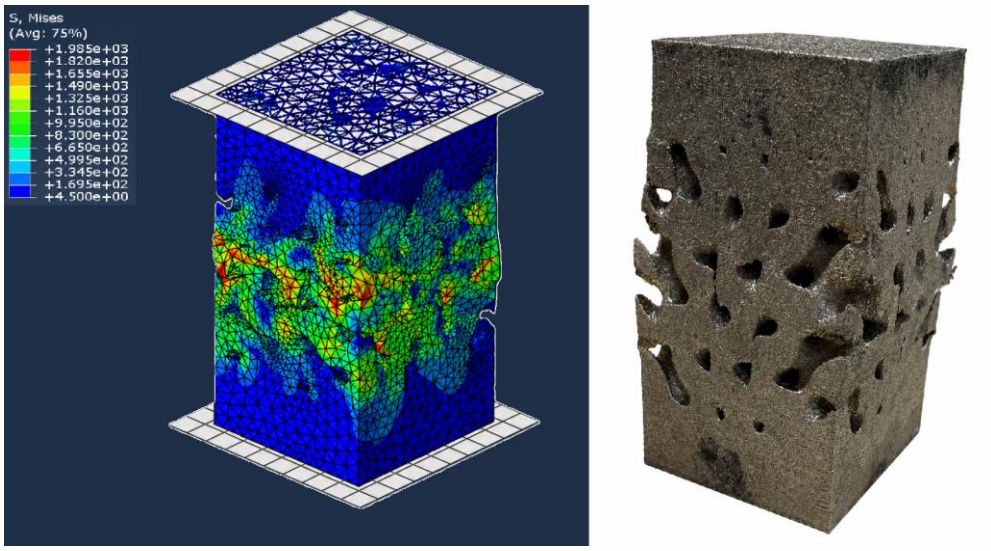

Figure 58. SP-CYL-A Deformation Comparison: Abaqus Stress Distribution and Experimental Compressed Specimen.

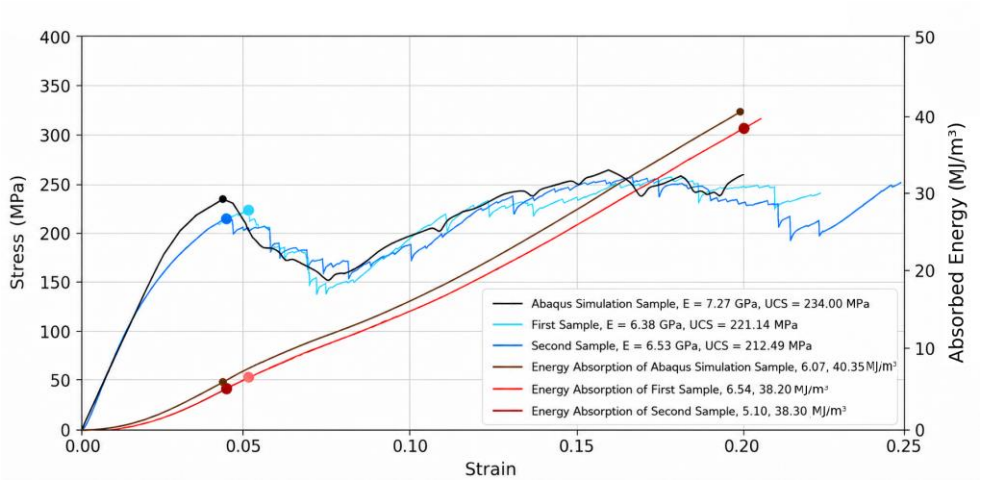

Figure 59. Experimental and Abaqus Compression Response Comparison for SP-CYL-A.

4.5.7 Stochastic sample: ST-A

The ST-A sample showed the weakest experimental mechanical performance among the selected 79% relative-volume samples. The experimental average elastic modulus was 5.34 GPa, and the UCS was 156.09 MPa. Abaqus predicted an elastic modulus of 5.15 GPa and a UCS of 168.89 MPa. This is the only case where the elastic modulus was slightly underestimated by the numerical model, while the UCS and absorbed energy were still overestimated. The absorbed energy at 0.20 strain was predicted closely, with 30.32 MJ/m³ in Abaqus compared with 29.63 MJ/m³ experimentally.

The stress distribution of ST-A in Figure 60 is less uniform than the TPMS samples. High-stress regions appear in scattered locations around irregular connections and local load paths. This behavior is consistent with the final compressed specimen, where the deformation is less symmetric and more localized. The stochastic architecture does not provide the same continuous and periodic load-transfer path as the Gyroid and Split-P structures. Therefore, local stress concentrations and early collapse are more likely. The lower experimental performance of ST-A is also consistent with the XCT observations, where the stochastic sample showed a higher defect content and a more irregular deviation pattern. Responses of the experimental and numerical simulation compression test are presented in Figure 61.

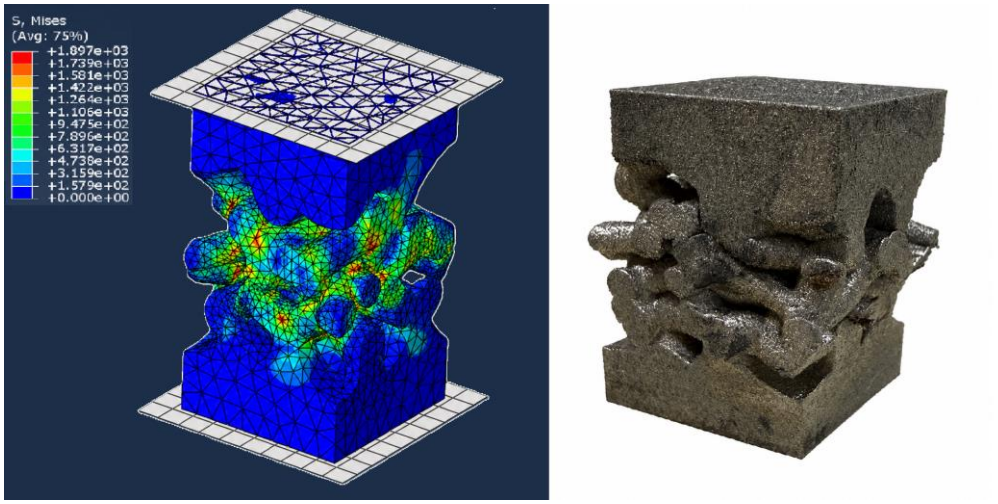

Figure 60. ST-A Deformation Comparison: Abaqus Stress Distribution and Experimental Compressed Specimen.

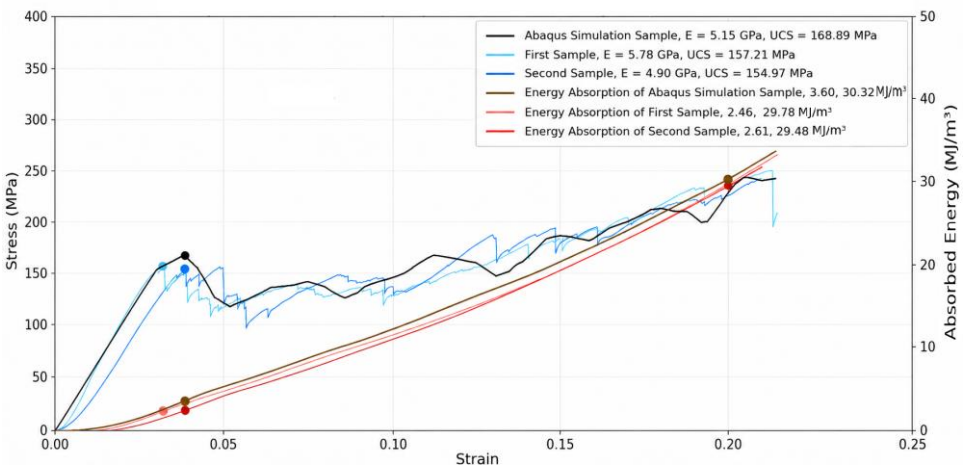

Figure 61. Experimental and Abaqus Compression Response Comparison for ST-A.

4.5.8 Overall Interpretation of the Numerical–Experimental Validation

The Abaqus simulations reproduced the main experimental trends of the 79% relative-volume lattice group and provided a clearer understanding of the deformation behavior of the investigated designs. The model correctly identified GY-CYL-A as the strongest and most energy-absorbing specimen, SP-CYL-A as the stiffest specimen, and ST-A as the weakest specimen. This agreement confirms that the numerical model was able to capture the main influence of topology and external configuration on the global compression response.

The stress maps showed that the highest stress concentration and main deformation occurred in the middle region of the lattice samples. This behavior was consistent with the final experimental compressed specimens, where the central region was the dominant collapse zone, while the top and bottom regions remained less deformed due to their contact with the compression plates. Therefore, the numerical contours were useful not only for comparison with the experimental curves, but also for interpreting the collapse mechanism of each structure.

The differences between the numerical and experimental results were mainly caused by the idealized nature of the Abaqus models. The real LPBF-fabricated samples contained surface roughness, powder adhesion, wall-thickness variations, geometrical deviations, and small internal defects, as observed in the XCT analysis. These imperfections can reduce the effective stiffness and strength and initiate local collapse earlier than in the ideal numerical model. In addition, fracture initiation and damage evolution were not explicitly included in the simulation, which explains why the numerical curves were generally smoother and, in some cases, slightly higher than the experimental curves.

Overall, the combined compression tests, XCT inspection, and Abaqus simulations showed that the Gyroid cylindrical configuration is the most effective design when high compressive strength and energy absorption are required. The Split-P cylindrical configuration is more suitable when high initial stiffness is the main target. In contrast, the

stochastic structure showed lower mechanical efficiency because of its irregular load-transfer paths, scattered stress concentration, and less uniform collapse behavior. Therefore, among the investigated LPBF 316L lattice structures, the TPMS-based cylindrical configurations provided the most reliable and mechanically efficient compression response.

Chapter 5

Conclusion

This thesis investigated the compressive behavior of 316L stainless steel lattice structures manufactured by Laser Powder Bed Fusion. Three different architectures were studied, including Gyroid, Split-P, and stochastic Voronoi structures, with both cubic and cylindrical configurations. The work combined design, LPBF fabrication, WEDM separation, XCT-based quality evaluation, quasi-static compression testing, and Abaqus numerical simulation in order to understand how topology, relative volume, geometrical configuration, and manufacturing quality affect the mechanical performance of the lattice samples.

The experimental results showed that the mechanical response of the samples was controlled not only by the relative volume, but also strongly by the internal architecture and the way the lattice was distributed inside the specimen. Although increasing the relative volume generally improved stiffness, strength, and energy absorption, samples with similar relative volume still behaved differently because of their different load-transfer paths. This confirms that, in lattice structures, the geometry of the architecture is as important as the amount of material used.

Among the tested samples, the Gyroid cylindrical structure with the highest relative volume, GY-CYL-A, showed the best overall performance. It reached the highest ultimate compressive strength, 236.44 MPa, and the highest absorbed energy at 0.20 strain, 43.11 MJ/m^3. This indicates that the continuous and smooth geometry of the Gyroid structure provided an efficient distribution of stress and a stable deformation response under

compression. Therefore, GY-CYL-A can be considered the most effective design among the studied samples when both strength and energy absorption are required.

The Split-P cylindrical sample, SP-CYL-A, showed the highest elastic modulus, 6.46 GPa, and therefore represented the stiffest design in the study. This makes the Split-P cylindrical configuration suitable for applications where resistance to initial elastic deformation is the main requirement. However, its strength and absorbed energy were lower than those of GY-CYL-A, showing that the stiffest structure is not necessarily the best energy absorber. In contrast, the stochastic Voronoi samples showed weaker and less stable compression behavior. The weakest experimental response was observed for ST-B, with an elastic modulus of 4.00 GPa, UCS of 95.31 MPa, and absorbed energy of 15.32 MJ/m³ at 0.20 strain. This lower performance can be related to the less regular internal architecture of the stochastic design, which produced less uniform load transfer and earlier local collapse.

The comparison between cubic and cylindrical configurations also showed that the internal configuration and cell mapping strategy influenced the mechanical behavior. In general, the cylindrical configurations performed better than the cubic ones, especially in the Gyroid group. This means that the design of lattice structures should not be limited only to topology selection; the final geometrical configuration inside the specimen must also be considered carefully.

The XCT analysis confirmed that the printed samples contained real manufacturing imperfections, such as geometrical deviations, local thickness variations, surface irregularities, and small internal defects. However, the mechanical behavior was not controlled by defect volume alone. Some samples with visible deviations still performed well because their topology created more effective load-transfer paths. Therefore, the as-built quality must be interpreted together with the designed architecture, rather than as an isolated factor.

The Abaqus simulations reproduced the main experimental trends with acceptable accuracy. The model correctly identified GY-CYL-A as the strongest and most energy-absorbing sample, SP-CYL-A as the stiffest sample, and ST-A as the weakest sample within the simulated 79% relative-volume group. The average absolute errors were approximately 7.00% for elastic modulus, 8.18% for UCS, and 6.51% for absorbed energy at 0.20 strain. These results show that the numerical model was reliable for predicting the global compression response and comparing the relative performance of the different lattice designs. The remaining differences between experiment and simulation were mainly related to the use of idealized numerical geometries, which did not fully include surface roughness, powder adhesion, local wall-thickness deviations, internal defects, and fracture events.

Overall, this thesis shows that LPBF-fabricated 316L lattice structures can be tailored for different mechanical functions by changing topology and geometrical configuration. The Gyroid cylindrical design was the most promising option for combined strength and energy absorption, while the Split-P cylindrical design was more suitable for high stiffness. The stochastic Voronoi structures were less efficient under the present compression conditions.

Future work should include more repeated tests, XCT-based finite element models, damage and fracture modeling, and fatigue or dynamic compression tests to further evaluate the reliability of these architectures for practical engineering applications.

References

[1] Gibson LJ, Ashby MF. Cellular Solids: Structure and Properties. Cambridge University Press; 1999.

[2] Fleck NA, Deshpande VS, Ashby MF. Micro-Architectured Materials: Past, Present and Future. Proceedings of the Royal Society A 2010;466:2495–516.

[3] Maconachie T, Leary M, Lozanovski B, Zhang X, Qian M, Faruque O, Brandt M. SLM Lattice Structures: Properties, Performance, Applications and Challenges. Materials & Design 2019;183:108137. https://doi.org/10.1016/j.matdes.2019.108137.

[4] Hanks B, Berthel J, Frecker M, Simpson TW. Mechanical Properties of Additively Manufactured Metal Lattice Structures: Data Review and Design Interface. Additive Manufacturing 2020;35:101301.

[5] Wang X, Xu S, Zhou S, Xu W, Leary M, Choong P, Qian M, Brandt M, Xie YM. Topological Design and Additive Manufacturing of Porous Metals for Bone Scaffolds and Orthopaedic Implants: A Review. Biomaterials 2016;83:127–41.

[6] Yin H, Zhang W, Zhu L, Meng F, Liu J, Wen G. Review on Lattice Structures for Energy Absorption Properties. Composite Structures 2023;304:116397. https://doi.org/10.1016/j.compstruct.2022.116397.

[7] Feng J, Fu J, Yao X, He Y. Triply Periodic Minimal Surface (TPMS) Porous Structures: From Multi-Scale Design, Precise Additive Manufacturing to Multidisciplinary Applications. International Journal of Extreme Manufacturing 2022;4:022001. https://doi.org/10.1088/2631-7990/ac5be6.

[8] Gibson I, Rosen DW, Stucker B. Additive Manufacturing Technologies: 3D Printing, Rapid Prototyping, and Direct Digital Manufacturing. Springer; 2015.

[9] Wong KV, Hernandez A. A Review of Additive Manufacturing. International Scholarly Research Notices 2012:208760. https://doi.org/10.5402/2012/208760.

[10] Thompson MK, Moroni G, Vaneker T, Fadel G, Campbell RI, Gibson I, Bernard A, Schulz J, Graf P, Ahuja B, Martina F. Design for Additive Manufacturing: Trends, Opportunities, Considerations, and Constraints. CIRP Annals 2016;65:737–60.

[11] DebRoy T, Wei HL, Zuback JS, Mukherjee T, Elmer JW, Milewski JO, Beese AM, Wilson-Heid A, De A, Zhang W. Additive Manufacturing of Metallic Components – Process, Structure and Properties. Progress in Materials Science 2018;92:112–224. https://doi.org/10.1016/j.pmatsci.2017.10.001.

[12] Ladani L, Sadeghilaridjani M. Review of Powder Bed Fusion Additive Manufacturing for Metals. Metals 2021;11:1391. https://doi.org/10.3390/met11091391.

[13] Yang L, Mertens R, Ferrucci M, Yan C, Shi Y, Yang S. Continuous Graded Gyroid Cellular Structures Fabricated by Selective Laser Melting: Design, Manufacturing and Mechanical Properties. Materials & Design 2019;162:394–404.

[14] Al-Ketan O, Lee D, Rowshan R, Abu Al-Rub RK. Functionally Graded and Multi-Morphology Sheet TPMS Lattices: Design, Manufacturing, and Mechanical Properties. Journal of the Mechanical Behavior of Biomedical Materials 2020;102:103520. https://doi.org/10.1016/j.jmbbm.2019.103520.

[15] Maskery I, Aremu AO, Parry L, Wildman RD, Tuck CJ, Ashcroft IA. Effective Design and Simulation of Surface-Based Lattice Structures Featuring Volume Fraction and Cell Type Grading. Materials & Design 2018;155:220–32. https://doi.org/10.1016/j.matdes.2018.05.058.

[16] Zhou H, Zhao M, Ma Z, Zhang DZ, Fu G. Sheet and Network Based Functionally Graded Lattice Structures Manufactured by Selective Laser Melting: Design, Mechanical

Properties, and Simulation. International Journal of Mechanical Sciences 2020;175:105480. https://doi.org/10.1016/j.ijmecsci.2020.105480.
[17] Yakout M, Elbestawi MA, Veldhuis SC. Density and Mechanical Properties in Selective Laser Melting of Invar 36 and Stainless Steel 316L. Journal of Materials Processing Technology 2019;266:397–420. https://doi.org/10.1016/j.jmatprotec.2018.11.006.
[18] Crisafulli D, Fintová S, Santonocito D, D'Andrea D. Microstructural Characterization and Mechanical Behaviour of Laser Powder Bed Fusion Stainless Steel 316L. Theoretical and Applied Fracture Mechanics 2024;131:104343. https://doi.org/10.1016/j.tafmec.2024.104343.
[19] Ma M, Wang Z, Zeng X. A Comparison on Metallurgical Behaviors of 316L Stainless Steel by Selective Laser Melting and Laser Cladding Deposition. Materials Science and Engineering A 2017;685:265–73. https://doi.org/10.1016/j.msea.2016.12.112.
[20] Zhao J, Liang Z, Sun Z. Compression Behavior of 316L Diamond Lattice Structures Fabricated via Additive Manufacturing with Variable Cell Sizes. Mechanics of Materials 2024;198:105135. https://doi.org/10.1016/j.mechmat.2024.105135.
[21] Alsalla H, Hao L, Smith C. Fracture Toughness and Tensile Strength of 316L Stainless Steel Cellular Lattice Structures Manufactured Using the Selective Laser Melting Technique. Materials Science and Engineering A 2016;669:1–6. https://doi.org/10.1016/j.msea.2016.05.075.
[22] Zhang L, Feih S, Daynes S, Chang S, Wang MY, Wei J, Lu WF. Energy Absorption Characteristics of Metallic Triply Periodic Minimal Surface Sheet Structures under Compressive Loading. Additive Manufacturing 2018;23:505–15. https://doi.org/10.1016/j.addma.2018.08.007.
[23] Pragana JP, Sampaio RFV, Bragança IMF, Silva CMA, Martins PAF. Influence of Processing Parameters on the Density of 316L Stainless Steel Parts Manufactured through Laser Powder Bed Fusion. Proceedings of the Institution of Mechanical Engineers, Part B: Journal of Engineering Manufacture 2020;234:1246–57.
[24] Leicht A, Rashidi M, Klement U, Hryha E. Effect of Process Parameters on the Microstructure, Tensile Strength and Productivity of 316L Parts Produced by Laser Powder Bed Fusion. Materials Characterization 2020;159:110016. https://doi.org/10.1016/j.matchar.2019.110016.
[25] Leicht A, Fischer M, Klement U, Nyborg L, Hryha E. Increasing the Productivity of Laser Powder Bed Fusion for Stainless Steel 316L through Increased Layer Thickness. Journal of Materials Engineering and Performance 2021;30:575–84.
[26] Liu J, Song Y, Chen C, Wang X, Li H, Zhou C, Wang J, Guo K, Sun J. Effect of Scanning Speed on the Microstructure and Mechanical Behavior of 316L Stainless Steel Fabricated by Selective Laser Melting. Materials & Design 2020;186:108355. https://doi.org/10.1016/j.matdes.2019.108355.
[27] Gebhardt A. Layer Manufacturing Processes. Understanding Additive Manufacturing, Carl Hanser Verlag; 2011, p. 31–63.
[28] Amaya-Rivas JL, Perero BS, Helguero CG, Hurel JL, Peralta JM, Flores FA, Alvarado JD. Future trends of additive manufacturing in medical applications: An overview. Heliyon 2024;10:e26641. https://doi.org/10.1016/j.heliyon.2024.e26641.
[29] Minetola P. Additive Manufacturing Systems and Materials (05SQSYP). Politecnico di Torino; 2024. Available at: http://iam.polito.it 2024.
[30] Puttonen T, Chekurov S, Kuva J, Bjorkstrand R, Partanen J, Salmi M. Influence of Feature Size and Shape on Corrosion of 316L Lattice Structures Fabricated by Laser Powder Bed Fusion. Additive Manufacturing 2023;61:103288. https://doi.org/10.1016/j.addma.2022.103288.

[31] Panwisawas C, Tang YT, Reed RC. Metal 3D printing as a disruptive technology for superalloys. Nature Communications 2020;11:2327. https://doi.org/10.1038/s41467-020-16188-7.
[32] Kamath C, El-Dasher B, Gallegos GF, King WE, Sisto A. Density of Additively Manufactured 316L SS Parts Using Laser Powder-Bed Fusion at Powers up to 400 W. International Journal of Advanced Manufacturing Technology 2014;74:65–78.
[33] Suryawanshi J, Prashanth KG, Ramamurty U. Mechanical Behavior of Selective Laser Melted 316L Stainless Steel. Materials Science and Engineering A 2017;696:113–21. https://doi.org/10.1016/j.msea.2017.04.058.
[34] Azarandaz P. A Comparative Multi-Method Study of Uniform and Graded TPMS Lattices Fabricated via Additive Manufacturing. Master Thesis. Politecnico di Torino, 2025.
[35] Li R, Liu J, Shi Y, Wang L, Jiang W. Balling Behavior of Stainless Steel and Nickel Powder during Selective Laser Melting Process. International Journal of Advanced Manufacturing Technology 2012;59:1025–35.
[36] Behjat A, Shamanian M, Taherizadeh A, Lannunziata E, Bagherifard S, Gadalińska E, Saboori A, Iuliano L. Microstructure–Electrochemical Behavior Relationship in Post Processed AISI316L Stainless Steel Parts Fabricated by Laser Powder Bed Fusion. Journal of Materials Research and Technology 2023;23:3294–311. https://doi.org/10.1016/j.jmrt.2023.01.229.
[37] Qiu N, Wan Y, Shen Y, Fang J. Experimental and Numerical Studies on Mechanical Properties of TPMS Structures. International Journal of Mechanical Sciences 2024;261:108657. https://doi.org/10.1016/j.ijmecsci.2023.108657.
[38] Ma X, Guo C, Wang Y, Shen J, Wang X. Design, Fabrication and Mechanical Properties of Multi-Dimensional Graded-Amplitude Gyroid Structures. Thin-Walled Structures 2025;210:113002. https://doi.org/10.1016/j.tws.2025.113002.
[39] Liu J, Li G, Li C, Li C, Fang J. Plasticity and Fracture Properties of Laser Powder Bed Fusion Fabricated 316L Stainless Steel — Experimental and Numerical Investigations. Mechanics of Materials 2026;215:105597. https://doi.org/10.1016/j.mechmat.2026.105597.
[40] Fan H, Yassin A. Fabrication, Characterization, and Compressive Properties of SLM-Fabricated 316L Triply Periodic Minimal Surface Structures. Proceedings of the Institution of Mechanical Engineers, Part C: Journal of Mechanical Engineering Science 2026;240:2387–403. https://doi.org/10.1177/09544062251409486.
[41] Hsieh J. Computed Tomography: Principles, Design, Artifacts, and Recent Advances. SPIE Press; 2009.
[42] Al-Ketan O, Rowshan R, Abu Al-Rub RK. Topology–Mechanical Property Relationship of 3D Printed Strut, Skeletal, and Sheet-Based Periodic Metallic Cellular Materials. Additive Manufacturing 2018;19:167–83. https://doi.org/10.1016/j.addma.2017.12.006.
[43] Deng T, Gong S, Cheng Y, Wang J, Zhang H, Li K, Nie Y, Shen B. Stochastic Lattice-Based Porous Implant Design for Improving the Stress Transfer in Unicompartmental Knee Arthroplasty. Journal of Orthopaedic Surgery and Research 2024;19:499.
[44] Colamartino I, Anghileri M, Boniardi M. Investigation of the Compressive Properties of Three-Dimensional Voronoi Reticula. International Journal of Solids and Structures 2023;284:112501. https://doi.org/10.1016/j.ijsolstr.2023.112501.
[45] Cheloni JPM, Zluhan B, Silveira ME, Fonseca EB, Valim DB, Lopes ESN. Mechanical Behavior and Failure Mode of Body-Centered Cubic, Gyroid, Diamond, and Voronoi Functionally Graded Additively Manufactured Biomedical Lattice Structures.

Journal of the Mechanical Behavior of Biomedical Materials 2025;163:106796. https://doi.org/10.1016/j.jmbbm.2025.106796.
[46] Park K-M, Min K-S, Roh Y-S. Design Optimization of Lattice Structures under Compression: Study of Unit Cell Types and Cell Arrangements. Materials 2021;15:97. https://doi.org/10.3390/ma15010097.
[47] Abueidda DW, Elhebeary M, Shiang C-S, Pang S, Abu Al-Rub RK, Jasiuk IM. Mechanical Properties of 3D Printed Polymeric Gyroid Cellular Structures: Experimental and Finite Element Study. Materials & Design 2019;165:107597. https://doi.org/10.1016/j.matdes.2019.107597.
[48] Maskery I, Sturm L, Aremu AO, Panesar A, Williams CB, Tuck CJ, Wildman RD, Ashcroft IA, Hague RJM. Insights into the Mechanical Properties of Several Triply Periodic Minimal Surface Lattice Structures Made by Polymer Additive Manufacturing. Polymer 2018;152:62–71.
[49] Ma S, Tang Q, Feng Q, Song J, Han X, Guo F. Mechanical Behaviours and Mass Transport Properties of Bone-Mimicking Scaffolds Consisted of Gyroid Structures Manufactured Using Selective Laser Melting. Journal of the Mechanical Behavior of Biomedical Materials 2019;93:158–69. https://doi.org/10.1016/j.jmbbm.2019.01.023.
[50] Fu J, Ding J, Qu S, Zhang L, Wang MY, Fu MW, Song X. Improved Light-Weighting Potential of SS316L Triply Periodic Minimal Surface Shell Lattices by Micro Laser Powder Bed Fusion. Materials & Design 2022;222:111018. https://doi.org/10.1016/j.matdes.2022.111018.
[51] Wang Y, Ren X, Chen Z, Jiang Y, Cao X, Fang S, Zhao T, Li Y, Fang D. Numerical and Experimental Studies on Compressive Behavior of Gyroid Lattice Cylindrical Shells. Materials & Design 2020;186:108340. https://doi.org/10.1016/j.matdes.2019.108340.
[52] Szatkiewicz T, Laskowska D, Bałasz B, Mitura K. The Influence of the Structure Parameters on the Mechanical Properties of Cylindrically Mapped Gyroid TPMS Fabricated by Selective Laser Melting with 316L Stainless Steel Powder. Materials 2022;15:4352. https://doi.org/10.3390/ma15124352.
[53] Li X, Xiao L, Song W. Compressive Behavior of Selective Laser Melting Printed Gyroid Structures under Dynamic Loading. Additive Manufacturing 2021;46:102054. https://doi.org/10.1016/j.addma.2021.102054.
[54] Ríos I, Duchêne L, Habraken AM, Oñate A, Valle R, Mertens A, Garrido C, Pincheira G, Tuninetti V. Compressive Behavior of 316L Stainless Steel Lattice Structures for Additive Manufacturing: Experimental Characterization and Numerical Modeling. Biomimetics 2025;10:680. https://doi.org/10.3390/biomimetics10100680.
[55] Rezapourian M, Jasiuk I, Saarna M, Hussainova I. Selective Laser Melted Ti6Al4V Split-P TPMS Lattices for Bone Tissue Engineering. International Journal of Mechanical Sciences 2023;251:108353. https://doi.org/10.1016/j.ijmecsci.2023.108353.
[56] Lei H, Li C, Meng J, Zhou H, Liu Y, Zhang X, Wang P, Fang D. Evaluation of Compressive Properties of SLM-Fabricated Multi-Layer Lattice Structures by Experimental Test and μ-CT-Based Finite Element Analysis. Materials & Design 2019;169:107685. https://doi.org/10.1016/j.matdes.2019.107685.
[57] nTop. Lattice generation software. nTop 2026. https://www.ntop.com/software/capabilities/lattice-structures/ (accessed June 11, 2026).
[58] Ho KH, Newman ST, Rahimifard S, Allen RD. State of the Art in Wire Electrical Discharge Machining (WEDM). International Journal of Machine Tools and Manufacture 2004;44:1247–59. https://doi.org/10.1016/j.ijmachtools.2004.04.017.
[59] International Organization for Standardization. ISO 13314:2011. Mechanical testing of metals — Ductility testing — Compression test for porous and cellular metals 2011.

[60] Bieler S, Weinberg K. Energy absorption of sustainable lattice structures under static compression. Meccanica 2025;60:2533–47. https://doi.org/10.1007/s11012-025-02003-4.
[61] Jia H, Lei H, Wang P, Meng J, Li C, Zhou H, Zhang X, Fang D. An Experimental and Numerical Investigation of Compressive Response of Designed Schwarz Primitive Triply Periodic Minimal Surface with Non-Uniform Shell Thickness. Extreme Mechanics Letters 2020;37:100671. https://doi.org/10.1016/j.eml.2020.100671.
[62] Kruth JP, Levy G, Klocke F, Childs THC. Binding mechanisms in selective laser sintering and selective laser melting. Rapid Prototyping Journal 2005;11:26–36. https://doi.org/10.1108/13552540510573365.
[63] Khairallah SA, Anderson AT, Rubenchik A, King WE. Laser powder-bed fusion additive manufacturing: Physics of complex melt flow and formation mechanisms of pores, spatter, and denudation zones. Acta Materialia 2016;108:36–45. https://doi.org/10.1016/j.actamat.2016.02.014.
[64] King WE, Barth HD, Castillo VM, Gallegos GF, Gibbs JW, Hahn DE, Kamath C, Rubenchik AM. Observation of keyhole-mode laser melting in laser powder-bed fusion additive manufacturing. Journal of Materials Processing Technology 2014;214:2915–25. https://doi.org/10.1016/j.jmatprotec.2014.06.005.
[65] Matthews MJ, Guss G, Khairallah SA, Rubenchik AM, Depond PJ, King WE. Denudation of metal powder layers in laser powder bed fusion processes. Acta Materialia 2016;114:33–42. https://doi.org/10.1016/j.actamat.2016.05.017.
[66] Cunningham R, Zhao C, Parab N, Kantzos C, Pauza J, Fezzaa K, Sun T, Rollett AD. Keyhole threshold and morphology in laser melting revealed by ultrahigh-speed X-ray imaging. Science 2019;363:849–52. https://doi.org/10.1126/science.aav4687.
[67] Oliveira JP, LaLonde AD, Ma J. Processing parameters in laser powder bed fusion metal additive manufacturing. Materials & Design 2020;193:108762. https://doi.org/10.1016/j.matdes.2020.108762.
[68] Cherry JA, Davies HM, Mehmood S, Lavery NP, Brown SGR, Sienz J. Investigation into the effect of process parameters on microstructural and physical properties of 316L stainless steel parts by selective laser melting. The International Journal of Advanced Manufacturing Technology 2015;76:869–79. https://doi.org/10.1007/s00170-014-6297-2.
[69] Liverani E, Toschi S, Ceschini L, Fortunato A. Effect of selective laser melting (SLM) process parameters on microstructure and mechanical properties of 316L austenitic stainless steel. Journal of Materials Processing Technology 2017;249:255–63. https://doi.org/10.1016/j.jmatprotec.2017.05.042.
[70] Saeidi K, Gao X, Zhong Y, Shen ZJ. Hardened austenite steel with columnar sub-grain structure formed by laser melting. Materials Science and Engineering A 2015;625:221–9. https://doi.org/10.1016/j.msea.2014.12.018.
[71] Riemer A, Leuders S, Thone M, Richard HA, Troster T, Niendorf T. On the fatigue crack growth behavior in 316L stainless steel manufactured by selective laser melting. Engineering Fracture Mechanics 2014;120:15–25. https://doi.org/10.1016/j.engfracmech.2014.03.008.
[72] Spierings AB, Schneider M, Eggenberger R. Comparison of density measurement techniques for additive manufactured metallic parts. Rapid Prototyping Journal 2011;17:380–6. https://doi.org/10.1108/13552541111156504.
[73] Yan C, Hao L, Hussein A, Raymont D. Evaluations of cellular lattice structures manufactured using selective laser melting. International Journal of Machine Tools and Manufacture 2012;62:32–8. https://doi.org/10.1016/j.ijmachtools.2012.06.002.
[74] Gumruk R, Mines RAW. Compressive behaviour of stainless steel micro-lattice structures. International Journal of Mechanical Sciences 2013;68:125–39. https://doi.org/10.1016/j.ijmecsci.2013.01.006.

[75] Smith M, Guan Z, Cantwell WJ. Finite element modelling of the compressive response of lattice structures manufactured using the selective laser melting technique. International Journal of Mechanical Sciences 2013;67:28–41. https://doi.org/10.1016/j.ijmecsci.2012.12.004.
[76] Choy SY, Sun C-N, Leong KF, Wei J. Compressive properties of functionally graded lattice structures manufactured by selective laser melting. Materials & Design 2017;131:112–20. https://doi.org/10.1016/j.matdes.2017.06.006.
[77] Maskery I, Aboulkhair NT, Aremu AO, Tuck CJ, Ashcroft IA. Compressive failure modes and energy absorption in additively manufactured double gyroid lattices. Additive Manufacturing 2017;16:24–9. https://doi.org/10.1016/j.addma.2017.04.003.
[78] Bobbert FSL, Lietaert K, Eftekhari AA, Pouran B, Ahmadi SM, Weinans H, Zadpoor AA. Additively manufactured metallic porous biomaterials based on minimal surfaces: A unique combination of topological, mechanical, and mass transport properties. Acta Biomaterialia 2017;53:572–84. https://doi.org/10.1016/j.actbio.2017.02.024.
[79] Melchels FPW, Bertoldi K, Gabbrielli R, Velders AH, Feijen J, Grijpma DW. Mathematically defined tissue engineering scaffold architectures prepared by stereolithography. Biomaterials 2010;31:6909–16. https://doi.org/10.1016/j.biomaterials.2010.05.068.
[80] Fantini M, Curto M, De Crescenzio F. A method to design biomimetic scaffolds for bone tissue engineering based on Voronoi lattices. Virtual and Physical Prototyping 2016;11:77–90. https://doi.org/10.1080/17452759.2016.1172301.
[81] Zadpoor AA. Bone tissue regeneration: The role of scaffold geometry. Biomaterials Science 2015;3:231–45. https://doi.org/10.1039/C4BM00291A.
[82] Campoli G, Borleffs MS, Amin Yavari S, Wauthle R, Weinans H, Zadpoor AA. Mechanical properties of open-cell metallic biomaterials manufactured using additive manufacturing. Materials & Design 2013;49:957–65. https://doi.org/10.1016/j.matdes.2013.01.071.
[83] Hazlehurst K, Wang CJ, Stanford M. Evaluation of the stiffness characteristics of square pore CoCrMo cellular structures manufactured using laser melting technology for potential orthopaedic applications. Materials & Design 2013;51:949–55. https://doi.org/10.1016/j.matdes.2013.05.009.
[84] Zadpoor AA. Additively manufactured porous metallic biomaterials. Journal of Materials Chemistry B 2019;7:4088–117. https://doi.org/10.1039/C9TB00420C.
[85] du Plessis A, Yadroitsev I, Yadroitsava I, le Roux SG. X-ray microcomputed tomography in additive manufacturing: A review of the current technology and applications. 3D Printing and Additive Manufacturing 2018;5:227–47. https://doi.org/10.1089/3dp.2018.0060.
[86] Thompson A, Maskery I, Leach RK. X-ray computed tomography for additive manufacturing: A review. Measurement Science and Technology 2016;27:072001. https://doi.org/10.1088/0957-0233/27/7/072001.
[87] TRUMPF. TruPrint 1000. https://www.trumpf.com/en_INT/products/machines-systems/additiveproduction-systems/truprint-1000/ (accessed June 13, 2026).
[88] Comet Technologies Canada Inc. Dragonfly 3D World. https://dragonfly.comet.tech/en/products/dragonfly-3d-world (accessed June 14, 2026).